

NBS TECHNICAL NOTE 1142

U.S. DEPARTMENT OF COMMERCE / National Bureau of Standards

NBS Reactor: Summary of Activities July 1979 to June 1980



OC
.00
5753
no. 1142
.981
.2

NATIONAL BUREAU OF STANDARDS

The National Bureau of Standards¹ was established by an act of Congress on March 3, 1901. The Bureau's overall goal is to strengthen and advance the Nation's science and technology and facilitate their effective application for public benefit. To this end, the Bureau conducts research and provides: (1) a basis for the Nation's physical measurement system, (2) scientific and technological services for industry and government, (3) a technical basis for equity in trade, and (4) technical services to promote public safety. The Bureau's technical work is performed by the National Measurement Laboratory, the National Engineering Laboratory, and the Institute for Computer Sciences and Technology.

THE NATIONAL MEASUREMENT LABORATORY provides the national system of physical and chemical and materials measurement; coordinates the system with measurement systems of other nations and furnishes essential services leading to accurate and uniform physical and chemical measurement throughout the Nation's scientific community, industry, and commerce; conducts materials research leading to improved methods of measurement, standards, and data on the properties of materials needed by industry, commerce, educational institutions, and Government; provides advisory and research services to other Government agencies; develops, produces, and distributes Standard Reference Materials; and provides calibration services. The Laboratory consists of the following centers:

Absolute Physical Quantities² — Radiation Research — Thermodynamics and Molecular Science — Analytical Chemistry — Materials Science.

THE NATIONAL ENGINEERING LABORATORY provides technology and technical services to the public and private sectors to address national needs and to solve national problems; conducts research in engineering and applied science in support of these efforts; builds and maintains competence in the necessary disciplines required to carry out this research and technical service; develops engineering data and measurement capabilities; provides engineering measurement traceability services; develops test methods and proposes engineering standards and code changes; develops and proposes new engineering practices; and develops and improves mechanisms to transfer results of its research to the ultimate user. The Laboratory consists of the following centers:

Applied Mathematics — Electronics and Electrical Engineering² — Mechanical Engineering and Process Technology² — Building Technology — Fire Research — Consumer Product Technology — Field Methods.

THE INSTITUTE FOR COMPUTER SCIENCES AND TECHNOLOGY conducts research and provides scientific and technical services to aid Federal agencies in the selection, acquisition, application, and use of computer technology to improve effectiveness and economy in Government operations in accordance with Public Law 89-306 (40 U.S.C. 759), relevant Executive Orders, and other directives; carries out this mission by managing the Federal Information Processing Standards Program, developing Federal ADP standards guidelines, and managing Federal participation in ADP voluntary standardization activities; provides scientific and technological advisory services and assistance to Federal agencies; and provides the technical foundation for computer-related policies of the Federal Government. The Institute consists of the following centers:

Programming Science and Technology — Computer Systems Engineering.

¹Headquarters and Laboratories at Gaithersburg, MD, unless otherwise noted; mailing address Washington, DC 20234.

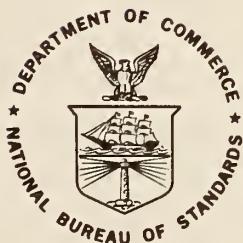
²Some divisions within the center are located at Boulder, CO 80303.

JUN 15 1981

NBS Reactor: Summary of Activities July 1979 to June 1980

Frederick J. Shorten, Editor

Reactor Radiation Division
National Measurement Laboratory
National Bureau of Standards
Washington, DC 20234



U.S. DEPARTMENT OF COMMERCE, Malcolm Baldrige, Secretary
NATIONAL BUREAU OF STANDARDS, Ernest Ambler, Director

Issued May 1981

National Bureau of Standards Technical Note 1142

Nat. Bur. Stand. (U.S.), Tech. Note 1142, 211 pages (May 1981)
CODEN: NBTNAE

U.S. GOVERNMENT PRINTING OFFICE
WASHINGTON: 1981

For sale by the Superintendent of Documents, U.S. Government Printing Office, Washington, D.C. 20402

Price

(Add 25 percent for other than U.S. mailing)

FOREWORD

The National Bureau of Standards Reactor was built not only to serve the needs of the NBS but also those of other government agencies and the greater Washington Scientific Community. The Reactor Radiation Division was established to operate the reactor and to foster its scientific and technological use. Toward this end, the Division has a small nucleus of scientists experienced in the use of reactors for a wide range of scientific and technical problems. In addition to pursuing their own research and developing sophisticated experimental facilities, they actively seek out and encourage collaboration with other scientists engaged in challenging programs whose work can benefit from use of the reactor, but who as yet do not have the reactor experience necessary to take full advantage of the facilities available. The Division also provides irradiation services to a wide variety of users as well as engineering and other technical services.

The reactor operates at 10 MW and is designed to provide more than 25 experimental facilities ranging from intense neutron beams to extensive irradiation facilities, making it one of the most versatile high flux research reactors in the country. Thus it is able to serve a large number of scientists and engineers in a broad range of activities both within and outside the NBS.

This report attempts to summarize all the work done which is dependent on the reactor including a large number of programs outside the Division. The first section summarizes those programs based primarily on Reactor Radiation Division (RRD) initiatives whereas the second and third sections summarize collaborative programs between RRD scientists and other NBS or non-NBS scientists respectively. The fourth section summarizes NBS work originating entirely outside the RRD which requires no collaboration with RRD scientists. The section entitled, "Service Programs" covers those programs originating outside NBS but for which RRD provides irradiation services. The remaining sections are self-explanatory.

FOREWORD

Due to mechanical difficulties during FY 80, the reactor operated only about six months during the period covered by this report. This severely curtailed the experimental program and is reflected in the reduced number of projects summarized here.

Appreciation is extended to F. J. Shorten of the Reactor Radiation Division for his extensive contributions to the editing, organization, and preparation of this report, and T. Hatley, T. Mangum, L. Sprecher, and S. Long for efforts in typing manuscripts.

A handwritten signature in dark ink, appearing to read "R. S. Carter". The script is cursive and fluid, with the first letters of each word being capitalized and prominent.

R. S. Carter
Chief, Reactor Radiation Division
National Bureau of Standards

ABSTRACT

This report summarizes all those programs which depend on the NBS reactor. It covers the period from July 1979 through June 1980. The programs range from the use of neutron beams to study the structure and dynamics of materials through nuclear physics and neutron standards to sample irradiations for activation analysis, isotope production, radiation effects studies, neutron radiography, and nondestructive evaluations.

Key words: Activation analysis; crystal structure; diffraction; isotopes; molecular dynamics; neutron; neutron radiography; nondestructive evaluation; nuclear reactor; radiation.

DISCLAIMER

Certain trade names and company products are identified in order to adequately specify the experimental procedure. In no case does such identification imply recommendation or endoresement by the National Bureau of Standards, nor does it imply that the products are necessarily the best available for the purpose.

TABLE OF CONTENTS

FOREWORD	iii
ABSTRACT	v
A. REACTOR RADIATION DIVISION PROGRAMS.	1
Mixed Crystals of $(\text{KCN})_x(\text{KB}_r)_{1-x}$	1
Neutron Scattering from Coherent Admixtures of Phonons with Libronic Excitations of Diatomic Impurities in Solids . .	1
Lattice Dynamics of βNbD^1	2
High Frequency Excitations in Metal-Hydrogen Systems	4
Theory of Quasielastic Neutron Scattering from Vanadium Deuterides at Large Momentum Transfers.	5
Joint Refinement of the X-Ray and Neutron Diffraction Data for Ribonuclease-A.	6
Use of the Pearson Type VII Distribution in Crystal Structure Refinements by the Profile Fitting Method	8
Estimates of Standard Deviations in Rietveld Powder Refinement.	20
Peak Shapes and Widths on the High Resolution Powder Diffractometer.	23
Optimum Strategy for Extracting Intensities from Noisy Data Collected with a Linear Detector.	25
Measurements for Nuclear Safeguards - NRC.	29
Nuclear Applications to Antiquities.	32
Comparison of Non-Reactor-Based Neutron Radiographic Facilities.	34
Measurement of the L/D Ratio	40
Resolution of a Radiographic Facility.	46
The Use of Neutron and X-Radiography to Evaluate Lithium/Iodine Pacemaker Batteries	50
Thermal Neutron Imaging Screen Development	57
Inclusion of Proton Spin in the Tunneling Wave Functions for Triangular Molecules of the Type XH_3 in Solids.	59

TABLE OF CONTENTS

Neutron-Antineutron Oscillations.	60
Microscopic Reversibility, Time-Reversal Invariance, and the Boltzmann H-Theorem.	62
Color Graphics and Imaging System	65
The Small-Angle Scattering Facility	66
B. RRD COLLABORATIVE PROGRAMS.	70
ErFe ₂ -- Finite Temperature Spin Waves.	70
Temperature Renormalization of Spin Wave Energies in HoCo ₂ . . .	74
Spin Glass-Ferromagnetic Phase Transition in Amorphous (Fe _x Ni _{1-x}) _{0.75} P _{0.16} B _{0.06} Al _{0.03}	76
Neutron Scattering Studies of the Magnetic Superconductor (Ce _{0.65} Tb _{0.35})Ru ₂	77
Ferromagnetic Phase Transition in the Reentrant Superconductor (Er _{0.11} Ho _{0.89})Rh ₄ B ₄	80
Magnetic Percolation in the Pseudobinary Superconductor (Ce _{1-x} Ho _x)Ru ₂	82
Neutron-Scattering Study of Spin Waves in the Antiferromagnet RbMnCl ₃	85
Structural Investigation of Th ₆ Mn ₂₃ D ₁₆	88
Preferential Ordering of MN and FE Atoms in Y ₆ (Fe _{1-x} Mn _x) ₂₃ . . .	91
Studies of Electron Density in Carbonate Minerals	93
Neutron Powder Diffraction Study of the Structure of Li ₂ ReO ₃ . .	96
Powder Neutron Diffraction Study of Chemically Prepared β-PbO ₂	100
Further Work on Geometrical Ambiguities in the Indexing of Powder Patterns.	110
Small-Angle Neutron Scattering Study of a Two-Phase Tungsten Alloy.	116

TABLE OF CONTENTS

Small-Angle Neutron Scattering Study of the Microstructural Development During Precipitation Strengthening of Ni Based Superalloys.	118
Thermal Motions in Ammonium Perchlorate.	124
The Detection of an Order-Disorder Phase Transition in a Molecular Crystal by Computer Molecular Dynamics.	128
 C. NON-RRD PROGRAMS	
Activation Analysis: Summary of 1980 Activities	130
Precision Gamma Ray and X-Ray Wavelengths.	159
Mass Assay of Standard Deposits.	161
Reactor Filtered Beams	163
Use of the Thermal Column at the NBS Reactor to Determine the Effective Mass of U-235 in a Miniature Fission Chamber. . .	163
Dynamic Scattering from Polymer Solutions.	171
Small-Angle Neutron Scattering on Atactic Polystyrene with High Labeled Chain Concentration.	176
Evaluation of Neutron Spectrum in the Intermediate-Energy Standard Neutron Field.	180
D. REACTOR OPERATIONS AND SERVICES.	183
E. SERVICE PROGRAMS	186
Activation Analysis Program of the Food and Drug Administration at the NBSR	186
U.S.G.S. Activation Analysis Program	189
F. PERSONNEL ROSTER	192
G. PUBLICATIONS	197

A. REACTOR RADIATION DIVISION PROGRAMS

MIXED CRYSTALS OF $(\text{KCN})_x(\text{KBr})_{1-x}$

J. M. Rowe and J. J. Rush

and

K. H. Michel
(UIA, Antwerp, Belgium)

and

S. Susman and D. G. Hinks
(Argonne National Laboratory, Argonne, IL)

and

S. Shapiro
(Brookhaven National Laboratory, Upton, NY)

In the past years measurements of neutron scattering on these mixed crystal systems have been extended in two ways. First, we have measured the interaction of tunnelling between levels of the ground state of a $(\text{CN})^-$ ion with the $[100]\text{TA}$ modes with $x = 0.0003$ using the triple-axis spectrometers at Brookhaven National Laboratory. This is the first direct spectroscopic observation of such an interaction, and it fully confirms the predictions based upon earlier results of polarized Raman scattering by Lüty and co-workers. At the same time we have extended and further refined our models for neutron scattering in systems with $x = 0.25, 0.50$ to include the concept of a dipole glass. We have developed theoretical models which explain most of the features observed, although several statistical mechanics problems persist.

NEUTRON SCATTERING FROM COHERENT ADMIXTURES OF PHONONS WITH LIBRONIC EXCITATIONS OF DIATOMIC IMPURITIES IN SOLIDS

R. C. Casella

Further analysis on this problem, the bulk of which was carried out during the prior period,¹ included discussion of the experimental

results of J. M. Rowe, J. J. Rush and collaborators² on the neutron scattering from the coherent state containing a tunnel-split component of the libronic ground state in KBr:CN^- . They observed an interaction in the T_{2g} configuration, as predicted by my analysis,³ which explained the earlier observed E_g interaction with the first libronic excitation. My results allow a reconciliation between the broad features of, on the one hand, the infrared and Raman data of F. Luty and co-workers at Utah, and on the other, the neutron data of the NBS-BNL-ANL team on KBr:CN^- and of R. M. Nicklow and collaborators at Oak Ridge on KCl:CN^- .^{3,4} These latter authors, who first proposed the coherent-admixture model, report some difficulty in fitting the detailed line shapes on the basis of a simple two-level version of the model.^{4,5} Nevertheless, the overall successes of the model are impressive.

-
1. R. C. Casella, *NBS Tech. Note No.* 1117, p. 26, (ed., F. Shorten) (1980).
 2. J. M. Rowe, J. J. Rush, S. M. Shapiro, D. G. Hinks, and S. S. Susman, *Phys. Rev.* **B21**, 4863 (1980).
 3. R. C. Casella, *Phys. Rev.* **B20**, 5318 (1979).
 4. R. M. Nicklow, Invited paper at the APS Solid State Meeting (March, 1980) and discussion thereafter.
 5. R. M. Nicklow, W. P. Crummett, M. Mosteller, and R. F. Wood, preprint (1980).

LATTICE DYNAMICS OF β NbD¹

A. Magerl

(University of Munich, Munich, Germany)

and

(National Bureau of Standards, Washington, DC)

and

J. M. Rowe

Recent measurements of the phonon dispersion of NbD_{0.85} both in the

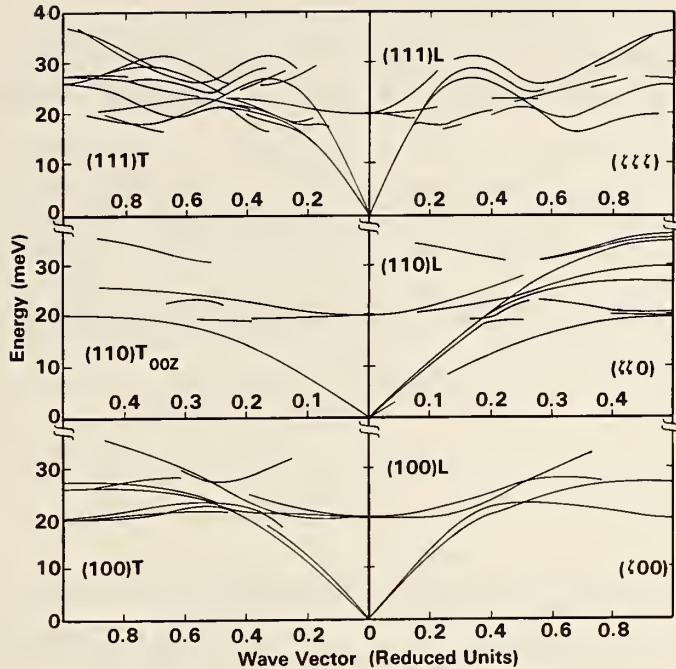


Figure 1. Phonon branches of β phase NbD shown in the Brillouin zone of the bcc lattice of the host metal Nb.

β phase and the α' phase by Shapiro et al.² have shown unexpected peaks throughout the Brillouin zone with little dispersion at about 18-19 meV.

We have calculated the phonon frequencies and the one phonon structure factor of β phase NbD with a simple Born-von Kármán model. The orthorhombicity of the crystal structure due to the ordering of the D and the multidomain nature of the crystals as used up-to-date was taken into account.

The salient feature from this model is the large number of observable phonon branches, as shown in figure 1. We want to emphasize the phonon modes at about 20 meV with a relatively large structure factor, which show up almost independent of the phonon wave vector. Careful investigation of the eigenvectors of these modes revealed that the structure factors for these modes are almost entirely due to a large vibrational amplitude of the Datons for particular modes in the β phase structure. Similar peaks observed in the α' phase may be attributed to the same mechanism and/or to short range order.

1. A. Magerl, J. M. Rowe, and D. Richter, "On the Observation of Low-Energy Excitations in NbD - A Simple Lattice Dynamical Model," (to be published).
2. S. M. Shapiro, Y. Noda, T. O. Brun, J. Miller, H. Birnbaum, and Kajitani, "Observation of Low-Frequency Excitations of Deuterium and Hydrogen in Niobium," *Phys. Rev. Lett.* 41, 1051, (1978).

HIGH FREQUENCY EXCITATIONS IN METAL-HYDROGEN SYSTEMS

A. Magerl

(University of Munich, Munich, Germany)

and

(National Bureau of Standards, Washington, DC)

and

J. J. Rush and J. M. Rowe

A new neutron spectrometer with an extremely high signal/background ratio has been put into operation recently. It is now possible to measure

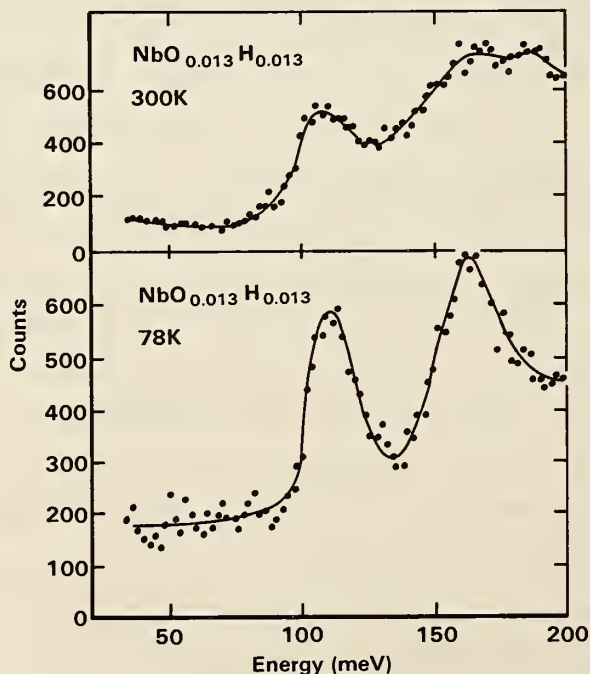


Figure 1. Shows as a first result the spectra of $\text{NbO}_{0.013}\text{H}_{0.013}$ at two different temperatures.

the vibrations of hydrogen atoms up to an energy of 200 meV in a so far unreached low concentration regime. These measurements are valuable to study the single defect behavior of the hydrogen atoms. We have successfully performed measurements on NbH_x with a concentration as low as $x = .001$ (atomic ratio).

Vibrational spectroscopy for systems like NbN_xH_y or NbV_xH_y ($.001 \lesssim x, y \lesssim .01$) can be used to provide a basic understanding of the thermodynamics of these ternary systems. Especially, information about the phase diagrams and thermodynamic potentials can be obtained from these measurements.

THEORY OF QUASIELASTIC NEUTRON SCATTERING FROM VANADIUM DEUTERIDES AT LARGE MOMENTUM TRANSFERS

N. F. Berk

Recent time-of-flight measurements by A. Magerl and H. Wipf¹ of neutron scattering from vanadium deuterides strongly suggest that at large momentum transfers ($4 \leq Q \leq 10 \text{ \AA}^{-1}$), the observed quasielastic intensity is dominated by incoherent scattering from vanadium atoms. The main source of this large- Q linewidth is believed to be phase incoherence produced by small, random displacements of the host atom equilibrium positions which are caused by the long-ranged interaction between the host atoms and the diffusing impurity nuclei. At present there is no specific theory of such large- Q , quasielastic neutron scattering from the host crystal, but a similar mechanism has been suggested for Mossbauer spectra that are anomalously broadened and shifted apparently as a result of interaction between the resonant nucleus and diffusing defects.^{2,3} Therefore, as a first approach to this difficult problem we are developing a theory along the lines originally taken by Krivoglaz and Repetskii¹ but with its range of applicability extended to the regimes of high impurity concentration and

large energy and momentum transfer. If a fit of experiment is possible with the theory, it will provide information both about the impurity diffusion and the dynamical response of the host atoms to the diffusing species. We will also explore the possibility that the same mechanism produces a quasielastic contribution to coherent neutron scattering.

-
1. A. Magerl and H. Wipf, private communication.
 2. M. A. Krivoglaz and S. P. Repetskii, *Sov. Phys. Solid State* B, 2325 (1967).
 3. A. Bläsius, R. S. Preston, and U. Gonser, *Proceeding of the Frühjahrstagung der Deutschen Physikalischen Gesellschaft*, 1978.

JOINT REFINEMENT OF THE X-RAY AND NEUTRON DIFFRACTION DATA FOR RIBONUCLEASE-A

Lennart Sjölin and Alexander Wlodawer
(National Institutes of Health, Bethesda, MD)

and

(National Bureau of Standards, Washington, DC)

Neutron diffraction experiments on single crystals of proteins allow direct locating of the positions of hydrogen atoms, leading to elucidation of additional details of the enzymatic mechanism, enzyme-substrate interaction, and the structure of bound solvent. The difficulty in interpretation of neutron diffraction results lies in an inherently lower quality of neutron data compared to analogous x-ray intensities, due to low fluxes of neutron sources and high background caused by inelastic scattering by hydrogen present in the sample. In addition, aliphatic side chains are difficult to locate at moderate resolution, since scattering of carbon is almost exactly balanced by that of attached hydrogens.

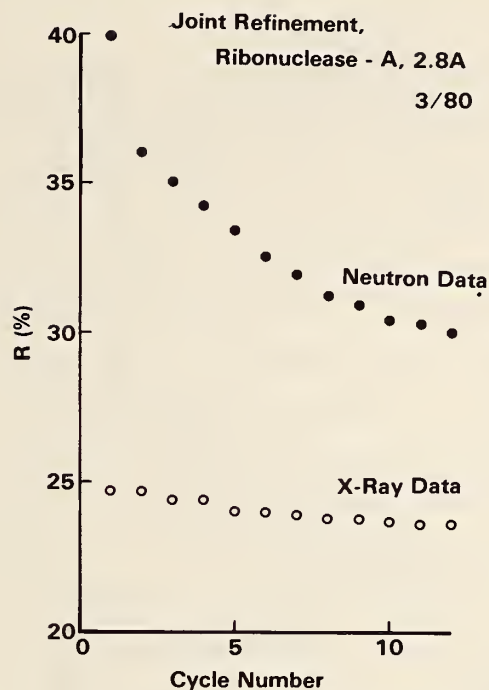


Figure 1. Progress of the joint x-ray neutron refinement of ribonuclease A.

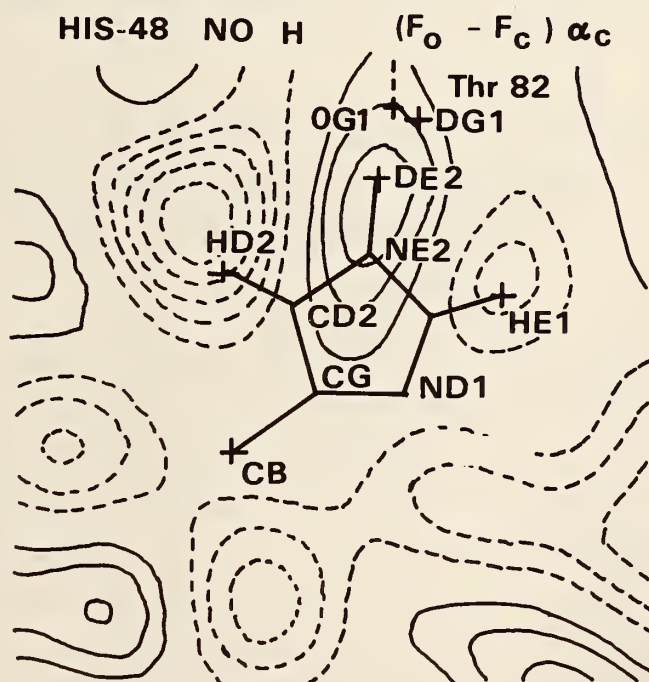


Figure 2. Difference Fourier map showing one of the histidine side chains. Hydrogen atoms in negative density, deuterium in positive density.

For these reasons, a procedure for joint refinement of neutron and x-ray data has been established. A conjugate gradient refinement program of Konnert and Hendrickson was modified to allow simultaneous refinement against both types of data. The procedure was tested by refining the data in a range of 2.8 - 10 Å obtained from monoclinic crystals of ribonuclease-A. The number of observed x-ray reflections was 2899 and neutron reflections 2549. The starting model was obtained by appending calculated hydrogen positions to the coordinates refined on the basis of x-ray data alone at 2.5 Å ($R = 25.2\%$). All hydrogens attached to oxygen or nitrogen were assumed to be exchanged for deuterium, while those attached to carbon were assumed not to exchange. The initial neutron R factor was 39.9%. In 11 cycles of joint refinement, the x-ray R factor dropped to 23.6% and neutron to 30.0%. Difference Fourier maps allowed correction of positioning and assignment of a large number of hydrogens, and the process is continuing. Diffraction data have also been collected for extending the resolution to 2.0 Å.

USE OF THE PEARSON TYPE VII DISTRIBUTION IN CRYSTAL STRUCTURE REFINEMENTS BY THE PROFILE FITTING METHOD

A. Santoro and E. Prince

Crystal structure refinement by profile fitting of powder diffraction data was originally developed for the neutron diffraction technique (Rietveld, 1969). The reason for this is due to the fact that the instrumental function of neutron diffractometers in general conforms closely to a Gaussian distribution. The case of x-ray powder data is more complex. Instrumental x-ray peak shapes are non-Gaussian and have been described, more or less successfully, by means of Lorentzian or Cauchy functions (e.g., Klug and Alexander, 1974), or by a composite of several Lorentzians (Huang and Parrish, 1975a, b), or by means of

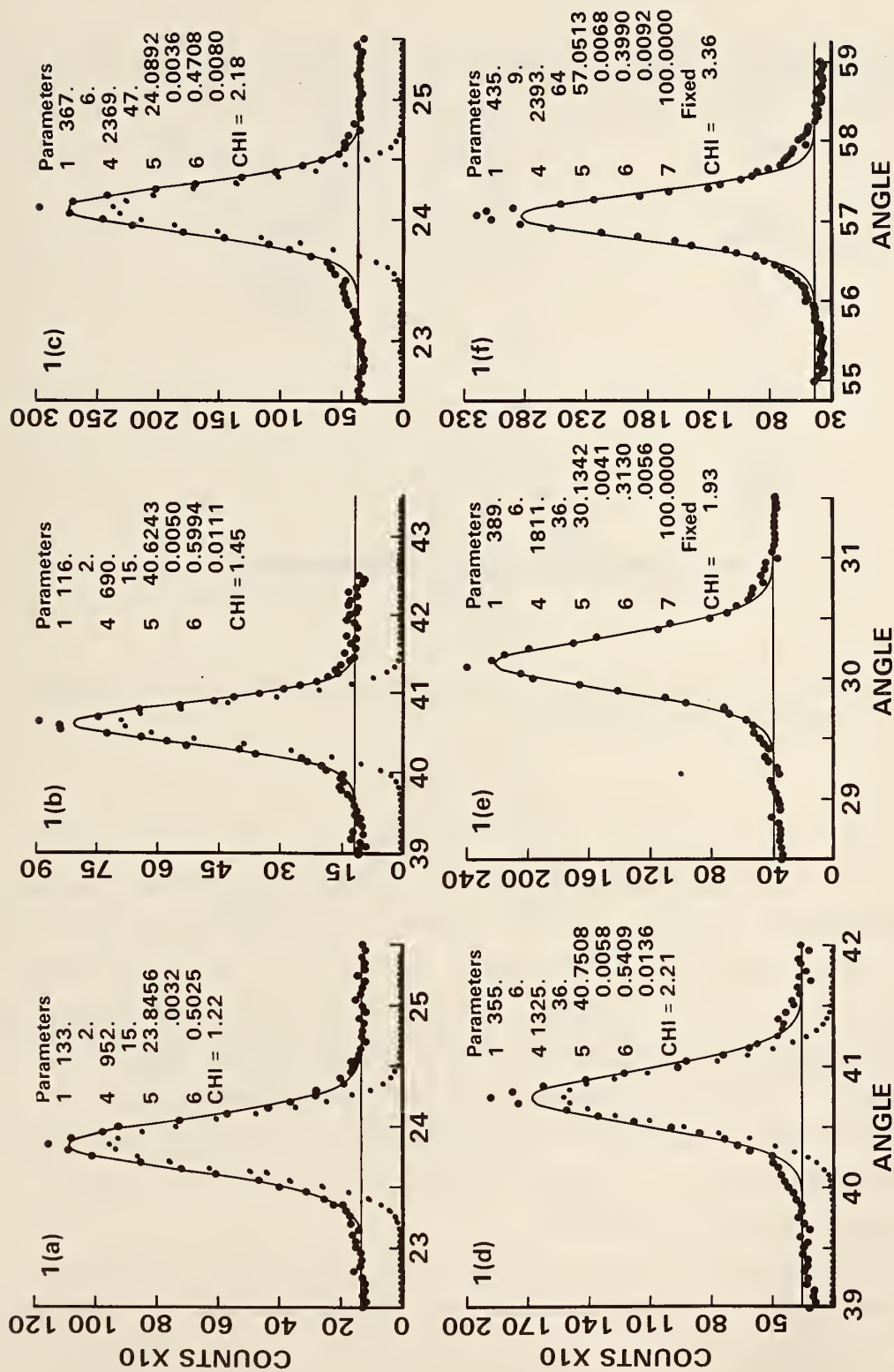


Figure 1. Gaussian least-square fits of single peaks in the powder patterns of Li_2ReO_3 (a,b), LiReO_3 (c,d), and Fe_3O_4 (e,f).

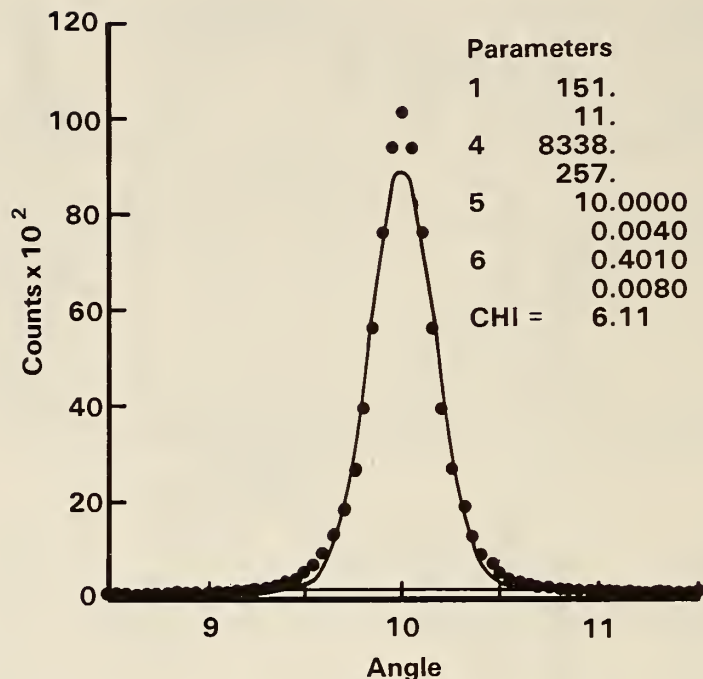


Figure 2. Gaussian least-squares fit of a "modified" Lorentzian calculated from the equation

$$y = y_0 \left[1 + \frac{(x - x_0)^2}{2a^2} \right]^{-2}$$

"modified" Lorentzians (Sonneveld and Visser, 1975; Malmros and Thomas, 1977; Khattak and Cox, 1977). Recently Hall, Veeraraghavan, Rubin, and Winchell (1977) have proposed the use of the Pearson type VII distribution (Elderton and Johnson, 1969), and this function has been applied to profile refinement by Immirzi (1978, 1980) in a study of isotactic polypropylene. The important feature of the Pearson distribution is that it can be varied gradually from a Gaussian to a Lorentzian, through the modified Lorentzian, by simply changing the value of one of the parameters defining the function.

In the course of a powder neutron diffraction study of Li_2ReO_3 , LiReO_3 , and Fe_3O_4 , it became apparent that the neutron diffraction peaks produced by samples of these compounds could not be described by a Gaussian function. Examples of Gaussian least-squares fits of these

peaks are shown in figure 1. To a degree, all the peaks of figure 1 appear quite similar to Lorentzian or modified Lorentzian distributions fitted with Gaussian functions (figure 2).

Under these circumstances it is not possible to carry out a refinement of the structures with the original program developed by

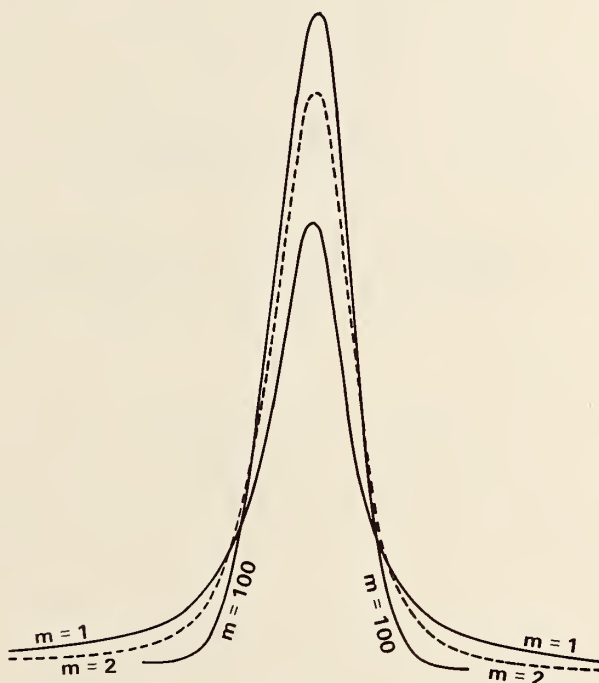


Figure 3. Calculated Pearson VII distributions for $m = 1, 2$, and 100 . The curve with $m = 100$ is indistinguishable from a Gaussian. The functions were calculated so that they have the same full width at half maximum and the same value of the area I .

Rietveld (1967), because it is based on the assumption of peaks with Gaussian intensity distribution. We are therefore in the process of generalizing our refinement procedure by using Pearson type VII functions.

The Pearson type VII distribution for the least-squares calculations is

$$y(x) = y_0 \left[1 + \frac{(x - x_0)^2}{ma^2} \right]^{-m} \quad (1)$$

Calling I the area under the curve, we have

$$I = \int_{-\infty}^{\infty} y_0 \left[1 + \frac{(x - x_0)^2}{ma^2} \right]^{-m} dx = 2 \int_0^{\infty} y_0 \left[1 + \frac{(x - x_0)^2}{ma^2} \right]^{-m} dx \quad (2)$$

Putting

$$z^{-1} = 1 + \frac{(x - x_0)^2}{ma^2} \quad (3)$$

we obtain

$$\begin{aligned} I &= \int_0^1 y_0 a m^{\frac{1}{2}} z^{m-3/2} (1 - z)^{-\frac{1}{2}} dz \\ &= y_0 a m^{\frac{1}{2}} B(m - \frac{1}{2}, \frac{1}{2}) = y_0 a m^{\frac{1}{2}} \frac{\Gamma(m - \frac{1}{2}) \Gamma(\frac{1}{2})}{\Gamma(m)} \\ &= y_0 a (m\pi)^{\frac{1}{2}} \frac{\Gamma(m - \frac{1}{2})}{\Gamma(m)} \end{aligned} \quad (4)$$

The full width w_p , at the level that is $1/p$ of the maximum can be easily obtained because

$$\left[1 + (w_p/2)^2 / (ma^2) \right]^{-m} = 1/p, \quad (5)$$

or

$$w_p = 2a \left[m(p^{1/m} - 1) \right]^{1/2} . \quad (6)$$

For the full width at half maximum H

$$H = 2a \left[m(2^{1/m} - 1) \right]^{1/2} \quad (7)$$

By combining the previous expressions, the Pearson type VII distribution can be written

$$y(x) = I \, 2 \left[(2^{1/m} - 1)/\pi \right]^{1/2} \frac{\Gamma(m)}{\Gamma(m - 1/2)} \frac{1}{H} \left[1 + \frac{4(x - x_o)^2}{H^2} (2^{1/m} - 1) \right]^{-m} \quad (8)$$

For $m = 1$ we have

$$a = H/2 , \quad y_o = (2I)/(H\pi)$$

and

$$y(x) = I \frac{2}{\pi} \frac{1}{H} \left[1 + \frac{4(x - x_o)^2}{H^2} \right]^{-1} \quad (9)$$

This is the Lorentzian or Cauchy function. For $m = 2$, since

$$\frac{\Gamma(m)}{\Gamma(m - 1/2)} = \pi^{1/2} = 2\pi^{-1/2}$$

we obtain

$$y(x) = I \frac{4(2^{1/2} - 1)^{1/2}}{\pi} \frac{1}{H} \left[1 + \frac{4(x - x_o)^2}{H^2} (2^{1/2} - 1) \right]^{-2} , \quad (10)$$

which is the so-called "modified" Lorentzian introduced by Sonneveld and Visser (1975) and used by Malmros and Thomas (1977) and by Khaltak and Cox (1977).

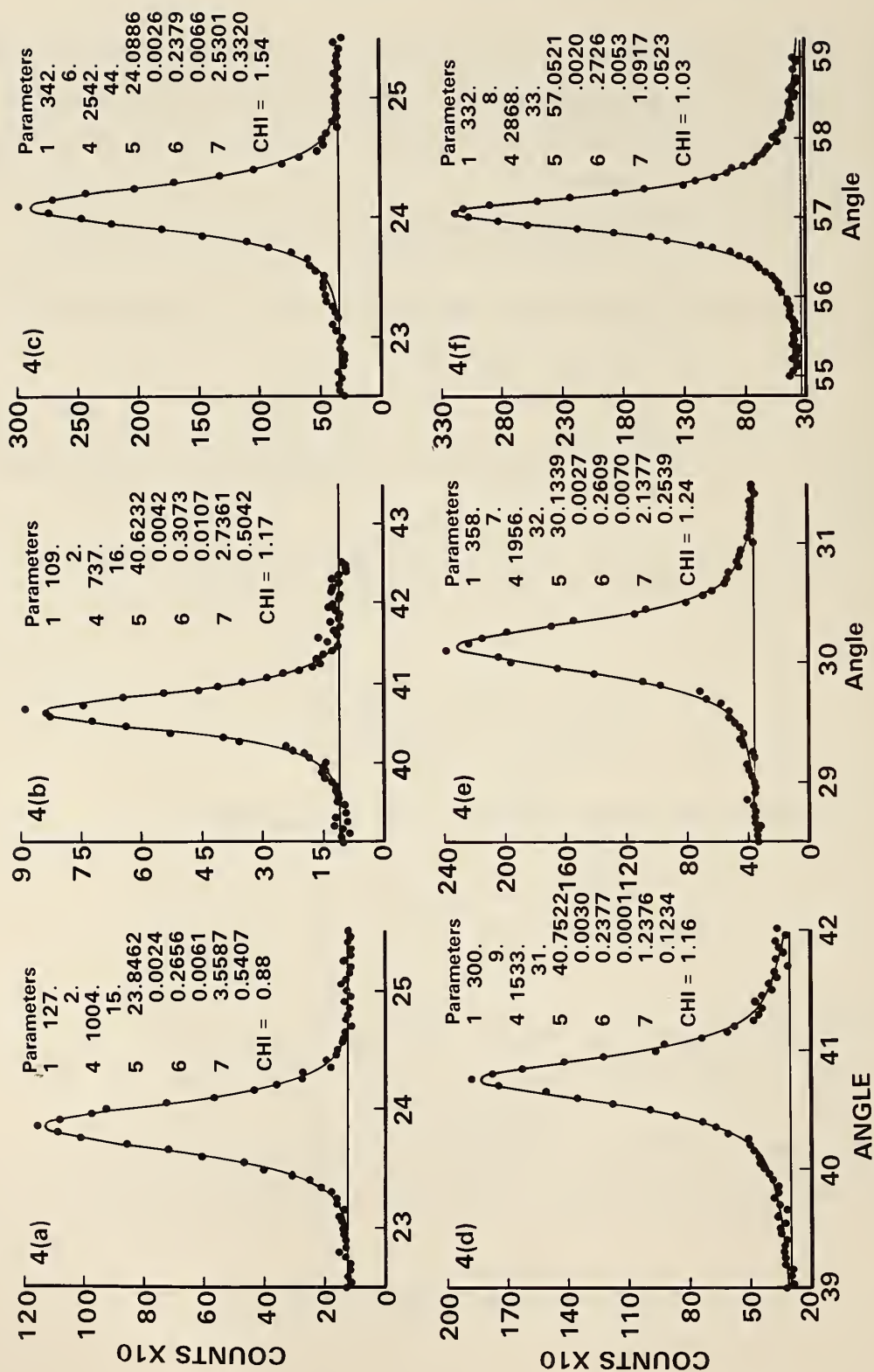


Figure 4. Pearson type VII fits of the same peaks of figure 1, i.e., peaks from Li_2ReO_3 (a,b), LiReO_3 (c,d), and Fe_3O_4 (e,f).

For $m \rightarrow \infty$ the expansion of $[1 + m^{-1}(x - x_0)^2/a^2]^{-m}$ according to the binomial series, becomes identical with the expansion of the exponential $\exp[-(x - x_0)^2/a^2]$. In addition, since

$$\lim_{m \rightarrow \infty} \frac{\Gamma(m)}{m^{\frac{1}{2}}(m^{\frac{1}{2}} - \frac{1}{2})} = 1$$

we have

$$y_0 = I/a\pi^{\frac{1}{2}}$$

and the function can be written

$$y(x) = I 2(\ln 2/\pi)^{\frac{1}{2}} \frac{1}{H} \exp \left[-(4\ln 2) \frac{(x - x_0)^2}{H^2} \right] \quad (11)$$

which is the Gaussian function used almost exclusively until recently in profile fitting refinements.

Examples of Pearson type VII functions, calculated with $m = 1$, $m = 2$, and $m = 100$, are shown in figure 3.

Figure 4 shows the peaks of figure 1 fitted with the Pearson type VII distribution. The values of χ for these fits are systematically lower than the corresponding ones obtained with the Gaussian function (figure 1). This is a clear indication that the Pearson distribution is more appropriate than the Gaussian to treat the diffraction data from the samples analyzed in this study.

Non-Gaussian peak shapes produced by neutron diffraction are caused by the physical conditions of the samples, rather than by instrumental factors. For example, particular distributions of crystallite sizes could be responsible for the observed effects. (Figure 5, in fact, shows that some of the peaks of figures 1 and 4 can be fitted equally well with two Gaussian functions with the same means but

different widths.) Structural distortions, and the consequent strains induced in the structure, may also cause a more or less pronounced departure from a Gaussian distribution.

Under these circumstances there are no physical reasons why m , the parameter appearing in equation (6) which defines the peak shape, should be constant over the entire 2θ angular range. In fact, in the case of Fe_3O_4 , the value of m varies with 2θ as indicated in figure 6. It seems that at low values of the diffraction angle the peak shape is close to a modified Lorentzian, while at high values of 2θ a Lorentzian distribution is more appropriate to describe the observed peaks. It is indeed difficult to find a physical justification for this kind of behavior, and no studies of this type have been reported so far in the literature for either neutron or x-ray diffraction data. If the variation of m with 2θ can be described by some suitable function, it can be incorporated into the refinement procedure.

In figure 7, H , the full width at half maximum, is plotted vs. 2θ for a number of single peaks in the powder pattern of Fe_3O_4 . Clearly, the behavior of $H(2\theta)$ can be described quite adequately in this case by the equation

$$H = U \tan^2 \theta + V \tan \theta + W \quad (12)$$

which is used in the original program written by Rietveld (1969).

It has to be expected that in a significant number of cases, the variations of m and H with 2θ will be more irregular than those shown in figures 6 and 7. For example, when peak shapes are dictated by crystallites with odd crystal habits (such as plate-like or needle-like) and particular size distributions, m and H may change from reflection to reflection in an apparently unrelated way, and reflections close to one another in 2θ may well have widely different values of m and H . In these cases the Rietveld technique is not applicable, and refinement will be possible only if some other procedure can be used to decompose overlapping peaks into the contributions from individual Bragg reflections.

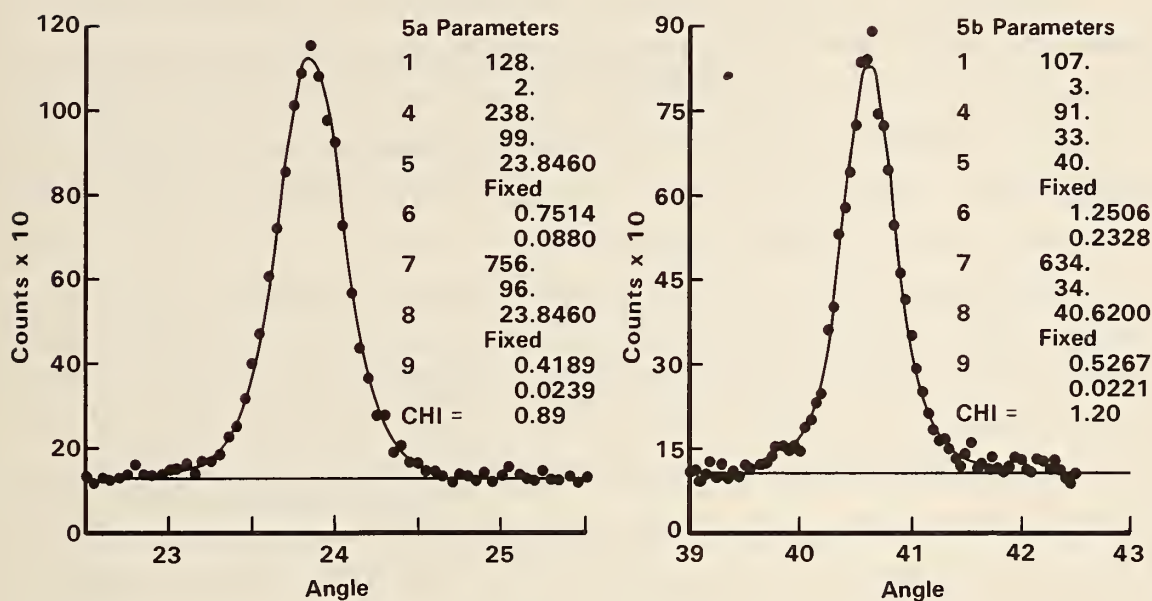


Figure 5. The two peaks of Li_2ReO_3 fitted by two Gaussians exactly superposed and having different full widths at half maximum.

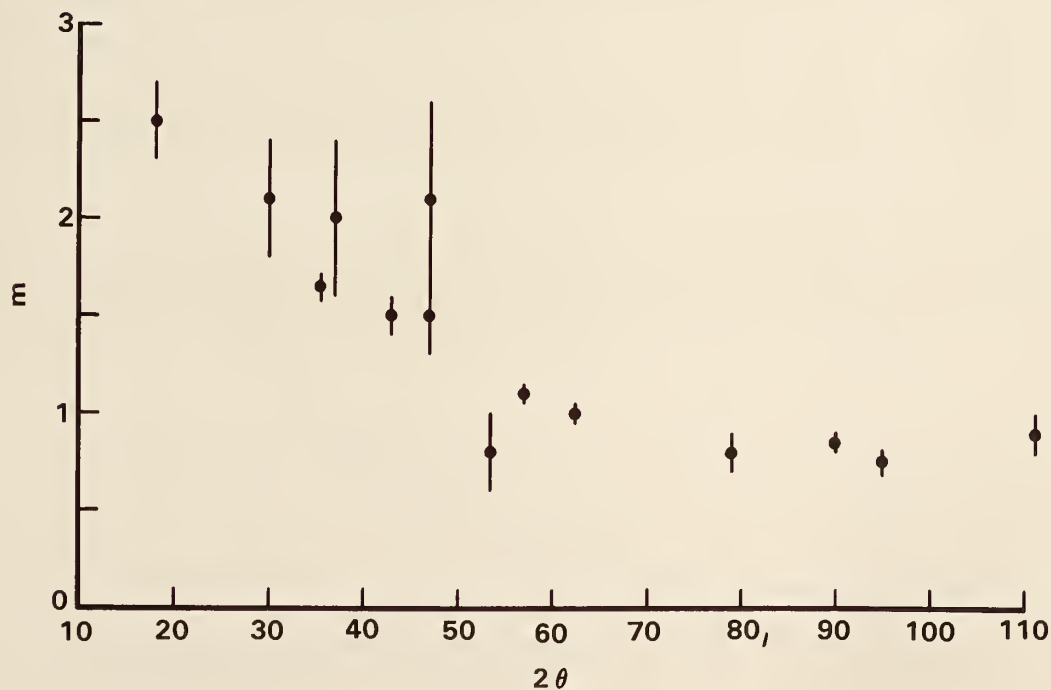


Figure 6. Plot of m versus 2θ for Fe_3O_4 .

In light of the above results, it seems that the angular dependence of m and H must be ascertained by analyzing the powder pattern prior to the profile refinement proper, and that the profile fitting programs should be modified so that the variation of these two parameters can be taken properly into account. Work in this direction is presently being done in our laboratory.

It is hardly necessary to emphasize the importance of finding a function which adequately describes the peak shape in the case of x-ray diffraction. Such function would permit the extension of structural profile refinement methods to the x-ray case and, by least-squares fitting individual peaks, would also allow to determine with high precision the height, angular position, and width of the peaks. This, in turn, would greatly facilitate the use of automatic indexing procedures and upgrade the quality of the information available in powder data files. Work is, therefore, planned to find if the Pearson distribution is also adequate for the x-ray powder technique.

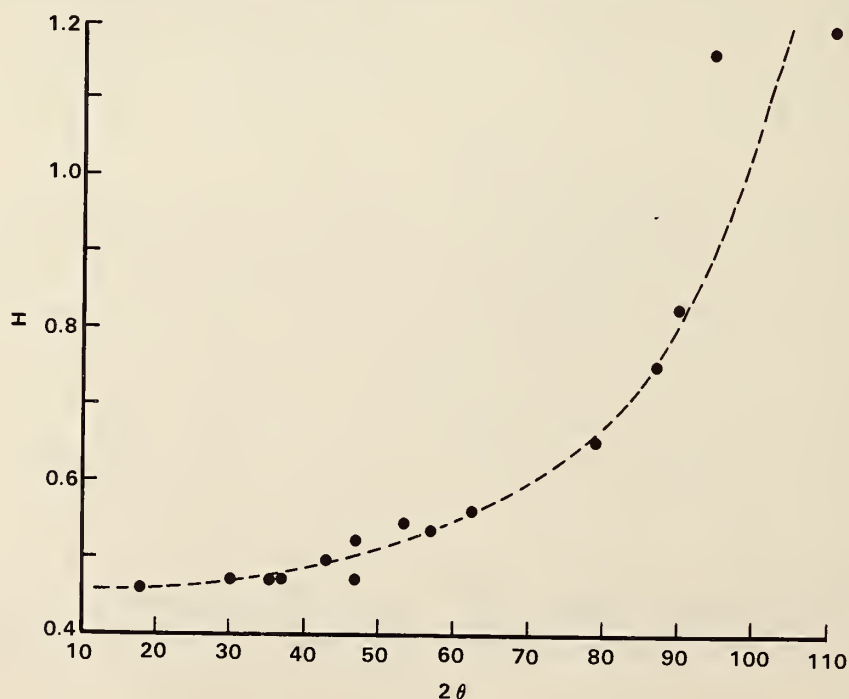


Figure 7. Plot of H versus 2θ for Fe_3O_4 .

-
1. W. D. Elderton and N. L. Johnson, *Systems of Frequency Curves*, Cambridge Press, New York, pp. 77-78 (1969).
 2. M. M. Hall, V. G. Veeraraghavan, H. Rubin and P. G. Winchell, *J. Appl. Cryst.* 10, 66-68 (1977).
 3. T. C. Huang and W. Parrish, *Acta Cryst.* A31, S198 (1975).
 4. C. P. Khattak and D. E. Cox, *J. Appl. Cryst.* 10, 405-411 (1977).
 5. H. P. Klug and L. E. Alexander, *X-ray Diffraction Procedures*, J. Wiley, New York, 2nd edition, p. 635 (1974).
 6. A. Immirzi, *11th International Congress of Crystallography*, Collected Abstracts, Warsaw (1978).
 7. A. Immirzi, private communication (1980).
 8. G. Malmros and J. O. Thomas, *J. Appl. Cryst.* 10, 7-11 (1977).
 9. H. M. Rietveld, *J. Appl. Cryst.* 2, 65-71 (1969).
 10. E. J. Sonneveld and J. W. Visser, *J. Appl. Cryst.* 8, 1-7 (1975).

ESTIMATES OF STANDARD DEVIATIONS IN RIETVELD POWDER REFINEMENT

E. Prince

In a recent paper Sakata and Cooper¹ assert that the standard deviations of refined parameters are estimated incorrectly in the Rietveld² method of refinement, which fits a model to the total powder pattern. They base their argument on an analysis in which expressions are derived for estimating the standard deviation by the Rietveld method and by an alternative method using the integrated intensities of individual peaks. They then compare the results of the two methods as applied to several experimental data sets, and observe that the standard deviations estimated by the Rietveld method are, in these cases, smaller than those estimated by the integrated intensity method.

An important difference between the two methods lies in the way that they estimate the intensities of individual resolved peaks. In the integrated intensity method the intensity of the k th peak, I_k , is given by

$$I_k = \sum_{i=i_0}^{i_f} Y_i - Nb, \quad (1)$$

where Y_i is the intensity at point i , N is the number of points in the peak, b is the background level, and the sum is taken over those points whose intensity exceeds background. Assuming Poisson statistics, the variance of I_k , $\sigma^2(I_k)$, is given by

$$\sigma^2(I_k) = \sum_{i=i_0}^{i_f} Y_i + N^2 \sigma^2(b), \quad (2)$$

where $\sigma^2(b)$ is the variance of the background level, which is assumed to have been determined separately. In the Rietveld method it is assumed that that shape of the k th peak can be described by a function, $G(i,k)$, that is normalized, so that

$$\sum_{i=i_0}^{i_f} G(i,k) = 1. \quad (3)$$

I_k can then be estimated by finding the values of I_k and b that minimize the function

$$S = \sum_{i=i_0}^{i_f} w_i \left\{ Y_i - [I_k G(i,k) + b] \right\}^2, \quad (4)$$

where the weight, w_i , again assuming Poisson statistics, is equal to $1/Y_i$. In this case the variance of I_k is given by

$$\sigma^2(I_k) = 1 / \sum_{i=i_0}^{i_f} [G^2(i,k)/Y_i]. \quad (5)$$

Sakata and Cooper showed that expression (2) and (5) are identical if the background, b , is exactly zero. In the presence of background, however, even if the background is very well determined, so that $\sigma^2(b)$ is negligible, expression (5) is smaller than expression (2). The difference is about a factor of 2 if background and peak intensity are comparable. Therefore, if $G(i,k)$ is a good representation of the peak shape, the Rietveld method yields more precise estimates of peak intensities than does the integrated intensity method.

If the weights applied to different Bragg peaks are different, the refined parameters will also differ slightly. However, the fact that one set of parameter estimates differs from another does not imply that either is biased. In fact it is an established principle of statistical estimation that the estimates of model parameters are not biased by the choice of weight,³ although the weights do affect the estimates of standard deviations.

The integrated intensity method minimizes the function

$$M_I = \sum_{k=1}^{N_B} w_k (I_{k\text{obs}} - I_{k\text{calc}})^2, \quad (6)$$

where N_B is the number of Bragg peaks in the pattern and $w_k = 1/\sigma^2(I_{k\text{obs}})$, as given by equation (2). The Rietveld method minimizes the function

$$M_P = \sum_{i=1}^N w_i \left[(Y_i - b) - \sum_{k=k_1}^{k_2} I_{k\text{calc}} G(i,k) \right]^2 \quad (7)$$

where $w_i = 1/Y_i$, N is the total number of points in the pattern, and the sum over k includes all reflections that contribute to Y_i . If the pattern consists entirely of resolved peaks, the two methods can be compared.

Equation (7) can be rewritten in the form

$$M_P = \sum_{k=1}^{N_B} \left[w'_k (I_{k\text{obs}} - I_{k\text{calc}})^2 + \sum_{i=1}^{N_k} w_i \left\{ Y_i - b - I_{k\text{obs}} G(i,k) \right\}^2 \right] \quad (8)$$

where N_k is the number of points contributing to the k th reflection and $w'_k = 1/\sigma_k^2(I_k)$ as given in equation (5). This expression consists of two sets of terms that may be viewed as a sum of squares involving the difference between observed and calculated values of the integrated intensity and a sum of squares involving observed and calculated intensities within a single peak. Except for the differences in weights, as discussed above, the first set of terms is identical to equation (6), while the second is a sum of terms like those in equation (4). The statistic

$$S_L^2 = \sum_{k=1}^{N_B} w_k (I_{k\text{obs}} - I_{k\text{calc}})^2 / (N_B - P), \quad (9)$$

where P is the number of refined parameters, is known as the "lack of fit mean square." The statistic

$$S_R^2 = \sum_{k=1}^{N_B} \sum_{i=1}^{N_k} w_i [Y_i - b - I_{k\text{obs}} G(i,k)]^2 / (N - N_B) \quad (10)$$

is known as the "replication mean square." Each of these is an unbiased estimate of the overall variance, and they have χ^2 distributions with $(N_B - P)$ and $(N - N_B)$ degrees of freedom, respectively. The ratio S_L^2/S_R^2 should be approximately equal to one, because the two quantities are estimates of the same thing and has the F distribution with $(N_B - P)$ and $(N - N_B)$ degrees of freedom. A statistical test based on the F distribution may be used to determine whether the model is an adequate fit to the data.

If the model fits the data, the standard deviations calculated by the Rietveld method will be smaller than those calculated by the integrated intensity method by an amount that reflects the difference between equation (5) and equation (2). Contrary to the assertion of Sakata and Cooper, differences that exceed this amount are due not to incorrectness in the Rietveld procedure but to lack of fit between model and data.

-
1. M. Sakata and M. J. Cooper, *J. Appl. Cryst.* 12, 554 (1979).
 2. H. M. Rietveld, *J. Appl. Cryst.* 2, 65 (1969).
 3. A proof of the fact that the choice of weights does not bias the parameter estimates appears in *Applied Regression Analysis* by N. R. Draper and H. Smith (John Wiley and Sons, New York), page 80.

PEAK SHAPES AND WIDTHS ON THE HIGH RESOLUTION POWDER DIFFRACTOMETER

E. Prince

A theoretical analysis by Caglioti, Paoletti, and Ricci¹ suggested that the individual peaks from a neutron powder diffractometer can be represented by Gaussian curves with widths that can be described, as a function of scattering angle, by the formula

$$H^2 = U \tan^2 \theta + V \tan \theta + W$$

Experimental studies² have shown that this formula described the pattern moderately well, but that the actual widths are larger than would be calculated from the Caglioti et. al. formula given the actual divergences of the various collimators. It has also been observed experimentally that the parameters U, V, and W must be refined for each powder pattern, that they can be markedly different for different substances, and that they tend to be very highly correlated. Because it seemed that the very sharp peaks of the BT-1 powder diffractometer might represent conditions beyond the assumptions of the UVW model,

and because the determination of magnetic moments, which often depend critically on a few strong, low angle peaks, it appeared to be desirable to make a careful study of actual shapes and widths.

To facilitate this study a computer program has been written which can be run interactively. It takes designated angle ranges from a binary file of data that have been PREPPed for input to the Rietveld program, to the peak region, and puts out the position, height, width, background, finds a peak within the range, fits a Gaussian-plus background function and goodness-of-fit parameter, so that the adequacy of the Gaussian shape model may be assessed.

Figure 1 is a summary of some preliminary results from this study. The solid curve is calculated from the UVW formula using the parameters from a profile refinement of α -alumina, using the pattern from which the

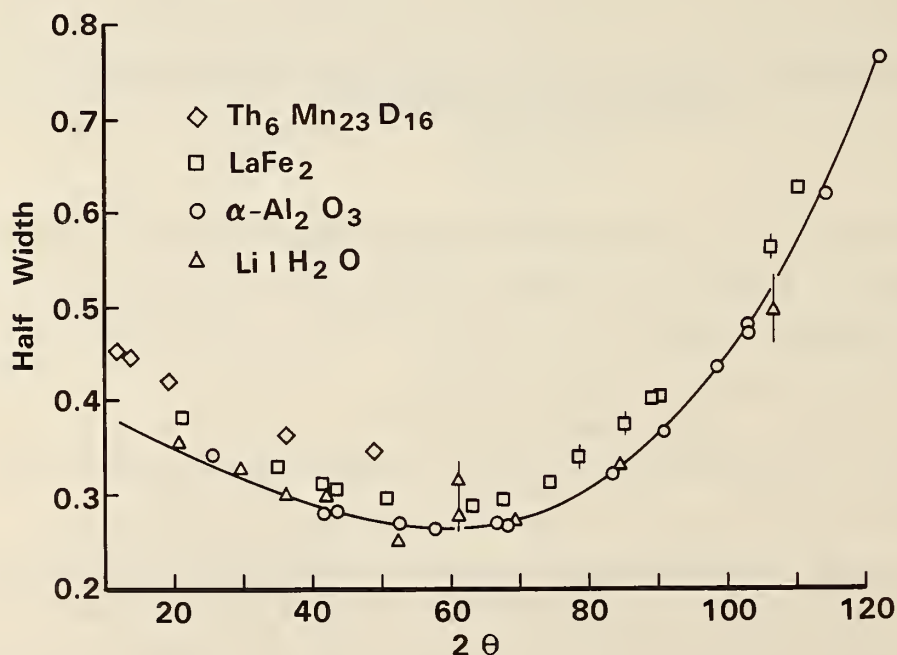


Figure 1. Peak widths on the high-resolution powder diffractometer for various components.

width points marked with circles were taken. The fit of the formula is quite good over the range of this well-resolved pattern, and it may be taken, at least tentatively, as an indication of true instrumental resolution when the sample is a well-crystallized, and strain-free powder. The points marked by squares come from an alloy that is, presumably, imperfectly annealed, and the diamonds come from an alloy that has been hydrided in the solid state, again, presumably, well below the annealing temperature. These samples show different degrees of what is probably strain broadening. The indication is that these patterns differ from the α -alumina pattern primarily in an addition to the width that is nearly constant with angle, and that the shape of the curve is relatively unaffected. Studies of magnetic moments will require much more information in the low angle region, below $20^\circ 2\theta$.

-
1. Caglioti, Paoletta, & Ricci, *Nucl. Instr.*, 3, 223-228 (1958).
 2. Santero, Maiezio, Roth, & Minor. *NBS Tech. Note* 1117, 94-110 (1980).

OPTIMUM STRATEGY FOR EXTRACTING INTENSITIES FROM NOISY DATA COLLECTED WITH A LINEAR DETECTOR

Lennart Sjölin and Alexander Wlodawer
(National Institutes of Health, Bethesda, MD)

and

(National Bureau of Standards, Washington, DC)

The problem of optimizing the signal-to-noise in the crystallographic data is of utmost importance to macromolecular crystallographers who have to measure thousands (or even hundreds of thousands) of reflections from each crystal. Since the total scattering is divided into so many reflections, the intensity of an average reflection is rather low and often not much different from the background. The signal-to-noise

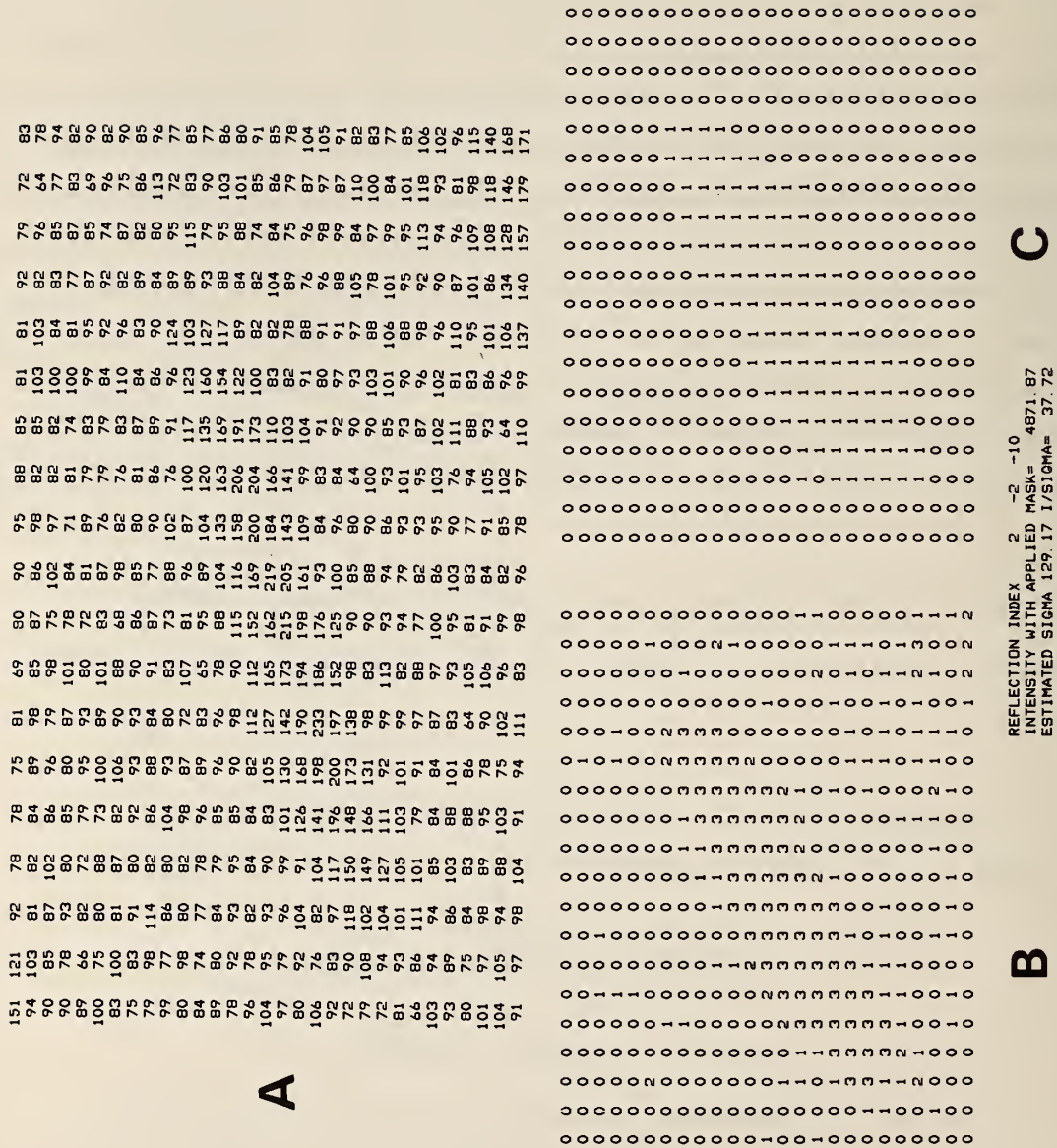


Figure 1. The effect of a nine-point parabolic smoothing procedure.

problem is particularly acute in the collection of neutron scattering data from protein crystals, in which strong incoherent scattering from hydrogen atoms creates very high background which could be lowered only by complete exchange of deuterium for hydrogen. This work was initially directed to improving the quality of data collected from the crystals of ribonuclease-A on a flat-cone diffractometer equipped with a position-sensitive linear detector and subsequently extended to other methods of data collection.

The procedure we created (the "dynamic mask procedure") is designed to calculate the position and extent of a reflection peak in a box containing, in addition, some background points in the presence of considerable noise. It is equally applicable to one-, two-, and three-dimensional data, but in what follows we will concentrate on the two-dimensional case, since extension of the method is straightforward.

Let us assume that a particular reflection is completely enclosed within a box and that no other reflections are intruding into the background. Since the noise level is high (see figure 1), any point within the box may be found to be above the average background level, but only the points belonging to the actual reflection are expected to be contiguous. Random noise can be suppressed by smoothing the data, by

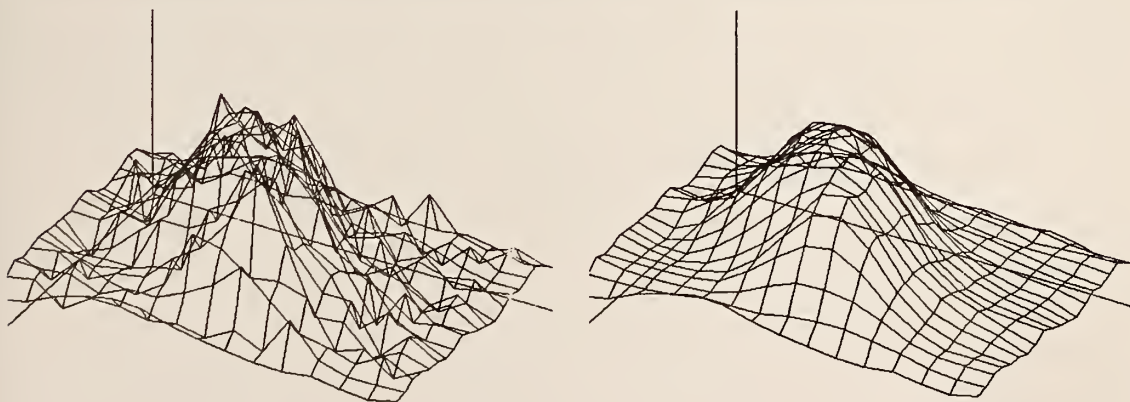


Figure 2. The dynamic mask procedure applied to a two-dimensional data array, showing: (a) the raw data from the linear detector; (b) the "sigma array"; and (c) the final mask calculated from the "sigma array".

including at each point some contribution from its neighbors. We have chosen a generalized version of the formula used by Spencer and Kossiakoff (1980):

$$\begin{aligned}
 I_{i,j} = & A \cdot (I_{i-1, j-1} + I_{i-1, j+1} + I_{i+1, j-1} + I_{i+1, j+1}) \\
 & + B \cdot (I_{i, j-1} + I_{i, j+1} + I_{i-1, j} + I_{i+1, j}) \\
 & + C \cdot I_{i,j}
 \end{aligned}$$

The best values found for very noisy data were $A=1$, $B=2$, and $C=3$, providing strong smoothing effects. For less noisy data, decreased contribution of the neighbors gave better results. The effect of different smoothing constants can be seen in figure 1. It is also evident that this procedure somewhat widens the peak boundary.

Once the data have been smoothed, it is possible to apply a "statistical filter" to distinguish between the data belonging to the peak and to the background. These procedures were modified in the neutron case to include the initial estimate of the background from the "universal background" data. Once the background level and its variance have been established, either directly on the basis of the points unlikely to contain peak information or on the basis of the universal background, the background is subtracted from each point and a flag is set, depending on whether the net intensity exceeds the background by less than $\sigma(0)$, between σ and 2σ (1), 2σ and 3σ (2), over 3σ (3). This so called "sigma-array" can be seen in figure 2. It is quite evident that the peak is contiguous, while the noise in the background points is random. We can now create a mask for this reflection from the contiguous part of "sigma-array," including all points flagged 1, 2, or 3. We call this mask "dynamic," since it is calculated independently for each medium or strong reflection and its shape, size, and position of the center are not constrained.

Integrated intensities are now calculated from the original data array by summing all elements indicated as peak by the mask and subtracting their background. The procedure has been used to collect ~20,000 reflections from a ribonuclease-A crystal. The refinement of the neutron data is in progress and will be reported later.

-
1. S. Spencer and A. Kossiakoff, *J. Appl. Cryst.*, to be published.

MEASUREMENTS FOR NUCLEAR SAFEGUARDS - NRC

Y. T. Cheng, M. Ganoczy, and D. A. Garrett

The continuing effort for Nuclear Safeguards project was devoted to 1) further development of software and 2) the final detail designs of the facility.

By utilizing the self indication effect for each different isotope, one can then attempt to analyze an unknown sample made of U-233, U-235, U-238 and/or Pu-239 nondestructively. The equation of self indication effect for individual isotope sample indicates that the detector response, S_k , is proportional to the energy sum of the product of $\phi(E)$, the transmitted neutron flux, and $\sigma_{F_k}(E)$, and the fission cross section of the detector material, k , i.e.

$$S_k \propto \int \phi(E) \sigma_{F_k}(E) dE = \int \phi_0(E) e^{-\sigma_T(E)X} \sigma_{F_k}(E) dE \quad (1)$$

where $\phi_0(E)$ is the initial neutron flux and $\sigma_T(E)$ is the total macroscopic cross section of sample isotope, and X is the thickness of the sample.

A collection of highly-enriched ($\geq 95\%$) samples U-233, U-235, U-238 and Pu-239 in the forms of metallic disks and with thickness ranging from 5 to 270 mils will be obtained for our use. Equation 1 enables the calculating of $\phi_0(E)$'s apart from a yet to be determined normalization constant with the measured detector response S_k and known

values of $\sigma_T(E)$'s and $\sigma_F(E)$'s. The relative $\phi_0(E)$ vs. E curve can be derived with different sample and detector material combinations and thus lends itself for easy cross checking. However, as it has been discussed earlier, the best sensitivity will be obtained when one uses the same material for both sample and detector. Furthermore, the relative $\phi_0(E)$ vs. E curve can be checked with that obtained using other methods. This provides an independent means of beam characterization and a chance to evaluate the self indication technique as a whole.

Once the calibration for the detecting system using known sample types and thicknesses has been established, one can then attempt to differentiate and quantify among U-233, U-235, U-238 and Pu-239 in an unknown sample. Equation 1 for a mixed composition sample becomes

$$S_k \propto \int \phi_0(E) e^{-\sum_{i=1}^4 \sigma_{T_i}(E) X_i} \sigma_{F_k}(E) dE \quad (2)$$

where i can be of U-233, U-235, U-238 and Pu-239 and k will be U-233, U-235, Pu-239 or Pu-241 because the fission cross sections of U-238 is very small.

If $\sigma_{T_i}(E) X_i < 1$ and we drop 3rd and higher order terms then

$$\begin{aligned} e^{-\sum_{i=1}^4 \sigma_{T_i}(E) X_i} &\approx \prod_{i=1}^4 [1 - \sigma_{T_i}(E) X_i + \frac{1}{2} \sigma_{T_i}^2(E) X_i^2] \\ &\approx 1 - \sum_{i=1}^4 \sigma_{T_i}(E) X_i + \frac{1}{2} \sum_{i=1}^4 \sum_{j=1}^4 \sigma_{T_i}(E) \sigma_{T_j}(E) X_i X_j \end{aligned}$$

and Equation 2 becomes

$$\begin{aligned} S_k &\propto \int \phi_0(E) e^{-\sum_{i=1}^4 \sigma_{T_i}(E) X_i} \sigma_{F_k}(E) dE \\ &\approx S_k^0 - \sum_{i=1}^4 K_{ik} X_i + \sum_{i=1}^4 L_{ik} X_i^2 + \sum_{i \neq j} M_{ijk} X_i X_j \end{aligned} \quad (3)$$

REACTOR RADIATION DIVISION PROGRAMS

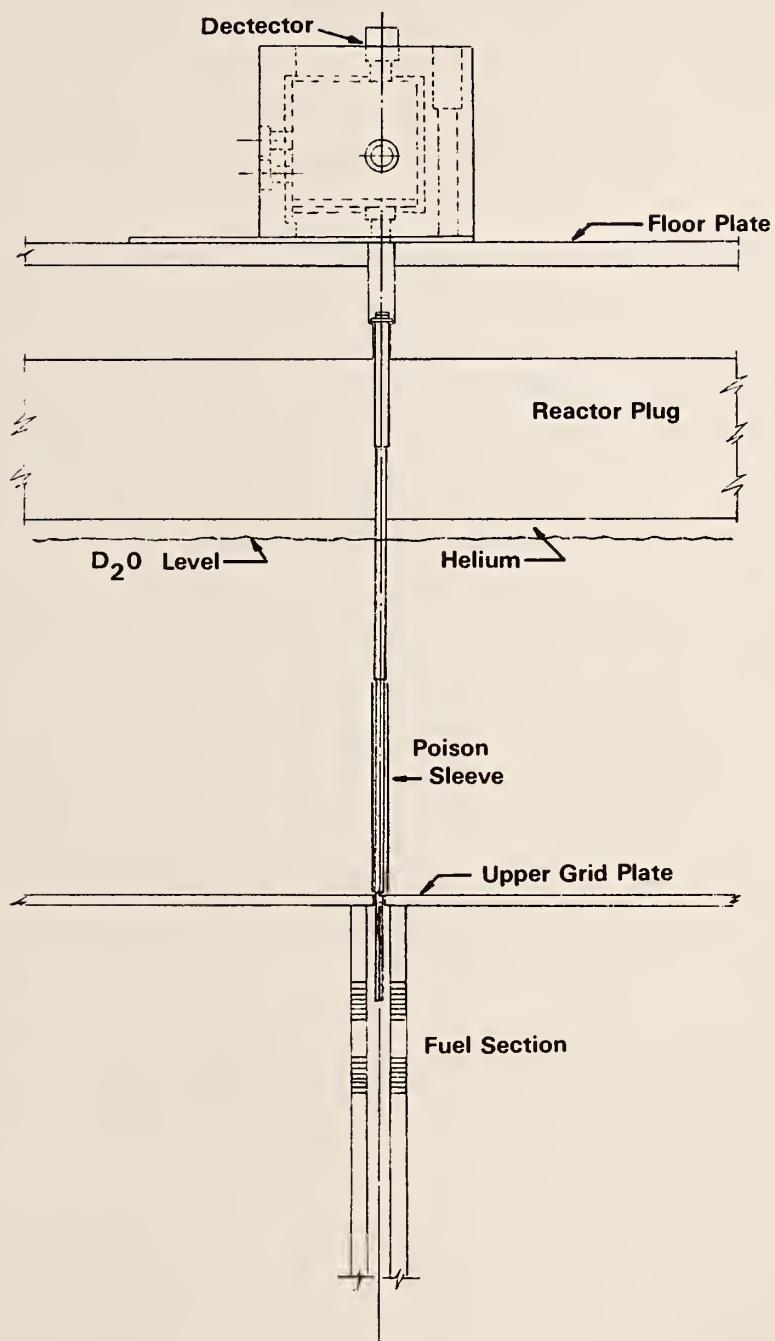


Figure 1. Schematic drawing of the Nuclear Safeguards Facility

$$\text{where } S_k^0 \equiv \int \phi_0(E) \sigma_{F_k}(E) dE$$

$$K_{ik} \equiv \int \phi_0(E) \sigma_{T_i}(E) \sigma_{F_k}(E) dE$$

$$L_{ik} \equiv \frac{1}{2} \int \phi_0(E) \sigma_{T_i}^2(E) \sigma_{F_k}(E) dE$$

$$\text{and } M_{ijk} \equiv \int \phi_0(E) \sigma_{T_i}(E) \sigma_{T_j}(E) \sigma_{F_k}(E) dE$$

S_k^0 is proportional to the detector response with no sample and the values of K_{ik} and L_{ik} can be extracted from the series expansion of Equation 1 for each unmixed sample. M_{ijk} can be calculated from the $\phi_0(E)$ vs. E curve and known values of $\sigma_{T_i}(E)$, $\sigma_{T_j}(E)$ and $\sigma_{F_k}(E)$.

The effect of dropping 3rd and higher order terms in the series expansion is small. Since the average values for $\sigma_T(E)$ is less than 200 barns and if we assume a typical sample thickness of 25 mils, the effect will only be ~0.7%. We then apply equation 3 to each and different fission detector looking over the same unknown sample. A computer program has been written to solve these multiple equations for various X's.

The final detail design of the facility has successfully gained the approval of NBSR Hazards Evaluation Committee.

NUCLEAR APPLICATIONS TO ANTIQUITIES

Y. T. Cheng, M. Ganoczy, and D. A. Garrett

During the past year we concluded the first phase and started the second phase of the feasibility study to employ nuclear technology for authenticating and studying reportedly valuable oil paintings. The project is funded by the Smithsonian Institution and the National Gallery of Art.

REACTOR RADIATION DIVISION PROGRAMS

The first phase of this project was conducted using a TRIGA reactor at the Armed Forces Radiobiology Research Institute (AFRRI), Bethesda, Maryland. Three test paintings were studied by both thermal-neutron induced-autoradiography and high-resolution gamma ray spectroscopy. The autoradiographs of test paintings show the usefulness of this technique.

The main emphasis of the initial phase, aside from establishing the necessary expertise in technical and skill areas, is to assess the suitability of the AFRRI reactor for this particular purpose. The requirements are that the reactor at its present condition or after reasonable modification can provide a 4' X 6" (or larger) thermal neutron field having a flux of $3 \times 10^9 \text{ n-cm}^{-2}\text{-s}^{-1}$ (or higher), and the unwanted high energy neutron and gamma ray components should be low.

The following table compares the doses received by the painting from both gamma and fast neutron radiation of the Brookhaven National Laboratory Medical Reactor Facility, The Armed Forces Radiobiological Research Institute and the proposed NBS reactor thermal column. As references, one should note that the painting receives a dose of ~ 20 Rads during a typical x-ray study. Based on the measurements made for the background radiation inside the exhibition room of the National Gallery of Art, a painting would receive approximately 150-200 Rads over a projected lifetime of 1,000 years. The radiation doses listed in the table are physical doses (in units of the rad) received by a typical painting^T during the neutron-autoradiography study. All numbers are normalized to a thermal neutron fluence of $8 \times 10^{12} \text{ n-cm}^{-2}$ except for the BNL graphite reactor where a fluence of $3.6 \times 10^{12} \text{ n-cm}^{-2}$ was used.

	BNL Graphite Reactor	BNL Medical Reactor	AFRRI Reactor	NBSR
Gamma Ray Dose	5500	1800	1500	~ 10
Fast Neutron Dose	38	80	70	~ 01

The present stage of radiation damage study indicated that for inorganic materials (pigments) 10^6 Rads or more are required before any

macroscopic changes of its properties can be detected. The threshold for organic materials (medium, varnish, supports, etc.), especially hydrogenous materials are lower (10^5 Rads). The doses which the painting received at the AFRRI reactor were 50 to 100 times less than the threshold. However, there is always an uneasiness toward the situation that one is proposing to have our national treasures exposed to radiations. A thorough microscopic study of the radiation damage is very involved and tedious due to the many varying factors (types of radiations, rate and amount of radiation, materials mixing, etc.), and its ability for simulating and predicting long term radiation effects is at best, uncertain.

This prompted the start of the second phase of the project, i.e., to conduct a feasibility study of modifying the NBSR thermal column for neutron-induced autoradiography use. The initial dosage measurements indicate the integrated fluence of 8×10^{12} n-cm⁻² is comparable to the 20 Rads dose in an x-ray study of painting, while the fast neutrons contributed an insignificant amount, i.e., less than 0.1 rad.

COMPARISON OF NON-REACTOR-BASED NEUTRON RADIOGRAPHIC FACILITIES

W. L. Parker and D. A. Garrett

The work reported here is sponsored by the U. S. Naval Ordnance Station at Indian Head, Maryland, and has involved visiting three operating neutron radiographic facilities of different types which do not use a reactor. Radiographs were taken of explosive devices supplied by the Navy and of various test objects and quality indicators.

Measurements were made of the L/D at different distances from the aperture, and the size and position of the effective aperture determined. A measure of the neutron to gamma ratio has been obtained, and the uniformity of the beam measured.

REACTOR RADIATION DIVISION PROGRAMS

The most important property of the facility, of course, is the length of time required to get a satisfactory radiograph. This is determined by the uses to which the facility will be put.

Non-technical features of the facility of interest are: maintenance and operating costs, downtime experience, and the amount of technical help needed for operation.

The three facilities visited were a Cf-252 source plus multiplier at the Mound Laboratory in Miamisburg, Ohio, a 2.5 MeV Van de Graaf neutron generator plus moderator at the Pantex Plant near Amarillo, Texas, and a D-T fast neutron generator plus moderator being developed at the Advanced Technology Center of the Vought Corporation in Grand Prairie, Texas, for the Army Materials and Mechanics Research Center.

1. Mound Laboratory

The Mound Facility uses a Cf-252 source to provide the original neutrons (by spontaneous fission) which are then multiplied and moderated by the multiplier. This is a subcritical reactor with a kof 0.990 which produces a thermal neutron multiplication of 28 times. The strength of the Cf-252 source at the time of the visit was about 25 milligrams.

It is the largest, heaviest, and most expensive of the facilities and would probably require the most construction if an existing building can not be used. It has a vertically-down beam, and the construction expense and amount of shielding required could be considerably reduced if a vertically-up beam is acceptable so that most of the shielding is supplied by the earth.

Measurements of L/D by the NBS method were made using radiographs of both the Aerotest and the NBS test objects. The results indicate that the effective aperture is about 2.5 inches in diameter and about 12 inches downstream (toward the object) from the aperture end of the collimator. This reduces the maximum available L/D from the nominal value of 107 ($=240/2.25$) to approximately 90.

Measurements of the film densities of a radiograph for which only part of the film was covered by a converter give $D_{\gamma}/D_n = 0.25$. At L =

240 inches the density falls off by 8 percent at 8 inches from the center of the film.

At the maximum available L/D a 12 hour exposure on SR film with a vapor-deposited Gd converter gives a density of 1.60.

The facility is often used at an L/D of about 36. At this setting the resolution at a distance of one inch from the cassette should be about 1.5 line pairs per mm. The resolution attainable at one inch should be close to 3.9 line pairs per mm at the maximum L/D.

One of the attractive features of the facility is the fact that it can be left unattended. This permits overnight exposures without additional labor costs.

For the same L/D and the same density the radiographs compare favorably with those from the NBS facility.

2. Pantex Plant

The facility at the Pantex Plant uses a Van de Graaf accelerator to produce a beam of 2.5 MeV deuterons which strike a beryllium target to produce neutrons by the $^9\text{Be}(d,n)^{10}\text{B}$ reaction. These neutrons are then moderated.

The Van de Graaf accelerator is mounted vertically with the beam coming down to strike the target at center of the moderator. There are two horizontal collimators, although only one beam seems to be in use at the moment. The Van de Graaf and the moderator could probably be made portable, but it might be difficult. Shielding requirements are probably less stringent than for the Californium multiplier.

Measurements of L/D by the NBS method were made using the Aerotest object only on four radiographs and the NBS object only on one radiograph. It is apparent from the values of L/D and the shape of the shadow patterns that the aperture is square. The effective aperture is about 2.6 inches square and located about 5 inches downstream from the aperture end of the collimator. Because of the size of the room and backscatter from the wall the maximum distance from the aperture is 10 feet which gives a maximum L/D of about 44.

Measurements of the film densities with and without a converter give $D_Y/D_n = 0.22$. At $L = 10$ ft. the density falls off by only 3 percent at 8 inches from the center of the film.

At the maximum available L/D a 4 hour exposure on SR film using a vapor-deposited Gd converter gives a density of about 2.1.

The facility is often used at an L of 6 feet which gives an L/D of about 26. At this setting the resolution at one inch from the cassette is 0.85 line pairs per mm. The maximum resolution attainable at one inch would be about 1.5. (it is shown in the previous report that resolution using a square aperture is roughly 18 percent less than that for a circular aperture of the same size.)

One drawback is that the Van de Graaf requires constant supervision with an operator present continually while the facility is in use. The major maintenance problems arise from the rupturing of the Be target. It has the definite advantage over the other two systems of not having a source which is continuously degrading. It can have the same problems as any other active vacuum system.

The radiographs compare favorably with those from the NBS facility.

3. Vought - Advanced Technology Center

The Vought facility uses as a neutron source a sealed tube generator which produces 14 MeV neutrons by the $^3\text{H}(d,n)^4\text{He}$ reaction. These neutrons are then moderated.

It is the smallest of the facilities and is semi-portable. It will be taken from Texas to the Yuma Proving Ground for testing. It is so designed that the source-moderator-collimator combination can be rotated through 180° to provide a beam in any direction from vertically-up to vertically-down. Shielding requirements should be about the same as for the Van de Graaf system, or less because of the lower neutron production.

Measurements of L/D by the NBS method were made from radiographs of the Aerotest object only. Although the aperture of the facility is reported to be square, both the values of L/D and the shape of the shadow patterns indicate that the effective aperture is approximately a 2.5 inch circle

about 30" below the top of the cover plate over the end of the collimator. These are the design values. It was said that there could be a reason for a square aperture to appear to be circular, but it is not known what that explanation is.

An optimum position of the cassette seems to be about 13 inches above the cover plate, giving an L/D of about 17. The optimum radiograph at this distance was made using M film and an experimental, proprietary screen being developed for Vought by Nuclear Enterprises, Inc. A 2 hour exposure produced a density of 1.23. The quality of the radiographs is not quite as good as if SR film and a Gd converter had been used but this would require prohibitively long exposure times. The quality is certainly acceptable.

For this position and L/D the resolution at one inch would be about 3/4 line pair per mm (3 line pairs per mm at 1 cm).

Measurements of the densities with and without a converter give $D_Y/D_n = 0.20$. The density falls off by about 10 percent at 6 inches from the center of the film.

This facility has a definite advantage over the other two because of its small size and portability. Vought is developing a real-time imaging system to be used with it, but it was not demonstrated.

Aside from the low flux, with resulting long exposure times, even for low resolutions, the other major difficulty would be operating expense. The warranty on a tube is 200 hours of operation before the intensity drops below 50 percent of its original value. At \$15,000, or more, per tube the system could become quite expensive to operate if any large volume of work is to be handled.

The facility does not seem to require constant supervision as does the Van de Graaf generator, but it is not presently left unattended for any lengthy periods of time.

4. Summary

The Vought facility is the smallest and lightest of the three and could most easily be made portable. If it is used on a regular basis the operating costs would be high - \$3,000 for a 40 hour week if the tube must be replaced after its warranty period. Its biggest drawback, however, is the neutron production rate which is about five percent of that of the other two facilities. This means prohibitively long exposure times or small values of L/D which will limit the resolution attainable.

The Mound facility and the Pantex facility have roughly equal rates of neutron production. At a medium L/D (of the order of 50) very satisfactory radiographs can be made in a 4 hour exposure, which can, of course, be reduced by using faster film-converter combinations than SR with vapor-deposited Gd.

The Cf multiplier would probably require a larger capital investment and may involve licensing procedures which could limit its use. If the Californium must be paid for, the materials cost would be more than for the Van de Graaf generator but less than for the Vought system if the latter is in continual use. The constant supervision required for the Van de Graaf would cut down considerably on the operating cost advantage of the Cf multiplier.

It seems safe to say that any new neutron radiographic facility must be custom designed to fit the uses to which it will be put.

MEASUREMENT OF THE L/D RATIO

W. L. Parker and D. A. Garrett

The last report of this work¹ describes a method for determining the L/D ratio for a neutron radiographic facility from microdensitometric measurements made of the shadow images of a series of small, identical, and parallel linear obstacles placed at uniformly increasing distances from the image plane. Also described were the test objects used--one borrowed from Aerotest Operations and one built at the National Bureau of Standards.

The report also defines the important parameters: L and h--the distances of the source and obstacle from the image plane, respectively, and $D = 2R$ and d_o --the widths of the source and the obstacle, respectively.

The method consists of approximating the microdensitometer tracings by trapezoids and measuring the widths of the base (w_d) and the top (w_c) of the trapezoid. When w_d and w_c are plotted vs. h, the resulting plots should be approximately straight lines from whose slopes the value of L/D can be determined.

Work this year has been largely concerned with a theoretical treatment of the images to be expected when the source is circular instead of linear, as was assumed in the earlier treatment.

1. Theory

The detailed analysis will be published elsewhere and only the results are given here.

One of the most important derived parameters is the value of h for which the umbra goes to zero. As was shown previously¹ it is given by

$$b = Ld_o/D. \quad (1)$$

For a parallel linear source and linear obstacle the shadow patterns will be symmetrical trapezoids whose height will be constant as long as $h < b$ with w_d increasing and w_c decreasing as h increases until the pattern becomes a triangle when $h = b$. For $h > b$, the pattern is again a trapezoid whose height decreases, while w_d and w_c both increase as h increases. The area of the trapezoid should remain constant.

For the case of a circular source and linear obstacle when $h < b$ the pattern will have a constant central region and will approximate a trapezoid with rounded corners. When $h > b$, there is no constant region, and the patterns deviate more and more from a trapezoid as h increases.

Figures 1a and 1b are calculated shadow patterns for the same parameters ($L/D = 68.8$, $h = 0.25, 0.75, 1.25, \dots, 4.25$ inches) for the linear source--parallel linear obstacle and the circular source--linear obstacle, respectively. Figure 1c is a reproduction of microdensitometer tracings from a radiograph taken with the same parameters. The agreement of figures 1b and 1c is excellent although, if the two figures are superimposed, there are some slight discrepancies.

The slopes of the plots for w_d and w_c are found by fitting the data by linear regression to equations of the form

$$w = a_0 + a_1 h(1-h/L)^{-1}. \quad (2)$$

The slope values: a_{1d} , a_{1c} and a_{1c+} are defined in the last report.¹ The average slope is defined as follows:

$$a_{lav} = (2a_{1d} + a_{1c-} + a_{1c+})/4 \quad (3)$$

The theoretical value of a_{lav} is MD/L , where M is the linear magnification of the microdensitometer.

It follows then, that

$$(L/D)_{exp} = M/a_{lav} \quad \text{Linear-Linear (4)}$$

where $(L/D)_{exp}$ represents the value of L/D obtained by this method.

The case of a circular source and linear obstacle is different. As is evident from figure 1b, the patterns are approximately trapezoidal only for quite small values of h . Furthermore, when $h > b$ there is no region of constant illumination. It is assumed that the measurement line when $h < b$ is drawn through the "half-power point" with the slope of the shadow pattern at that point, and that the intersections of this line with the top and bottom of the trapezoid determine w_d and w_c . When this

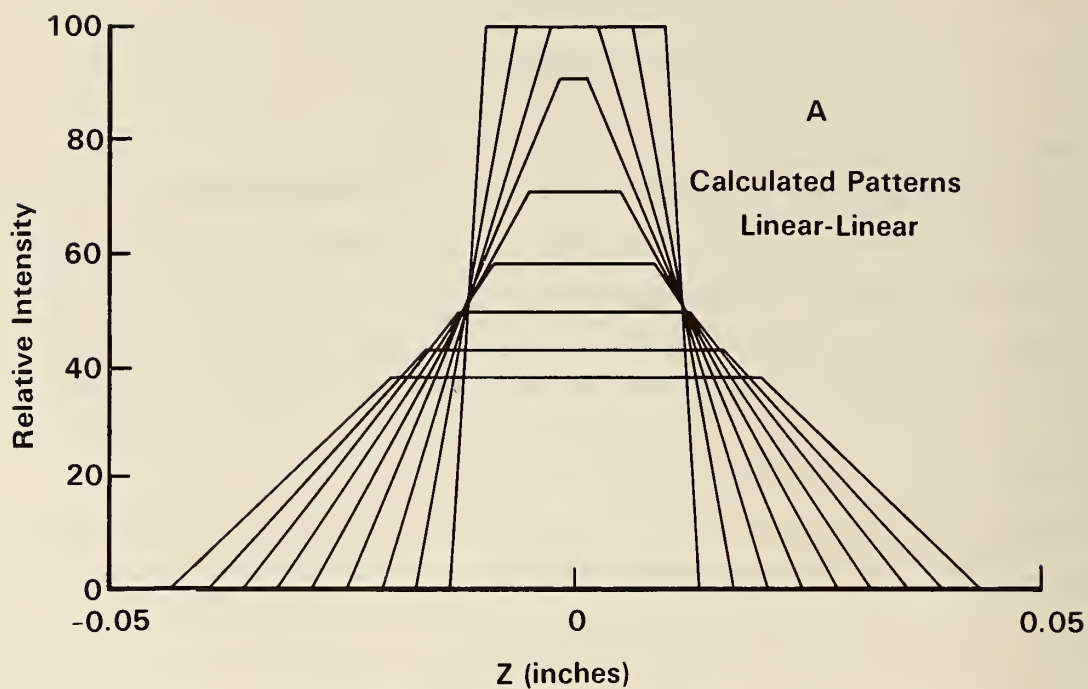


Figure 1(a). Shadow patterns for Linear Source - Parallel Linear Obstacle.

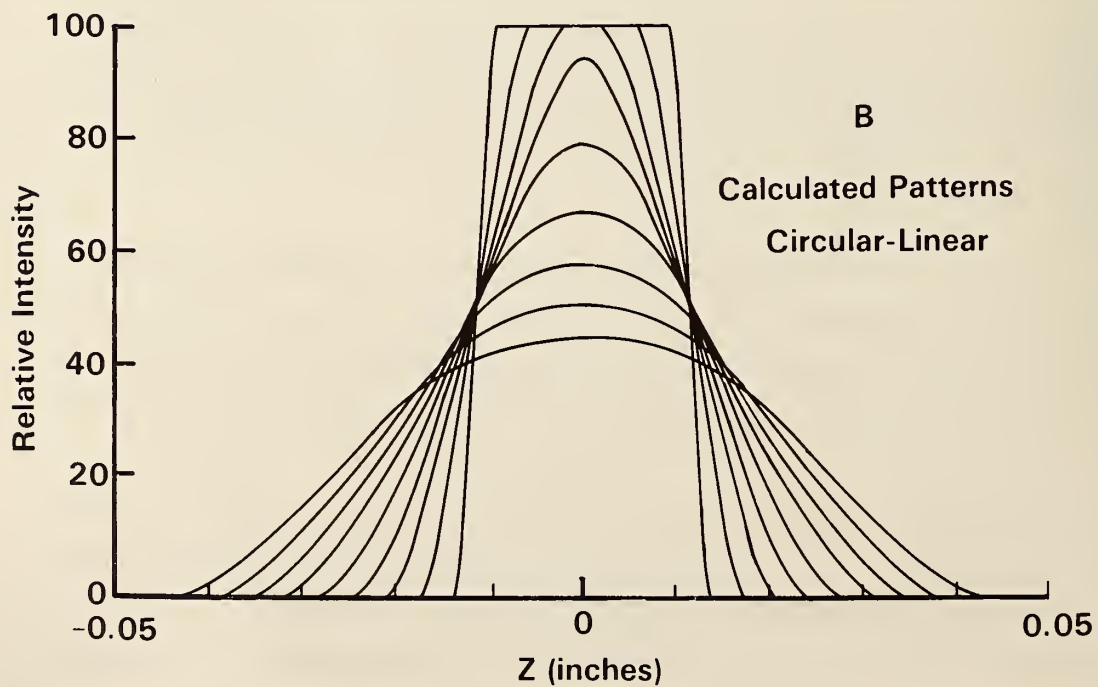


Figure 1(b). Shadow patterns for Circular Source - Linear Obstacle.

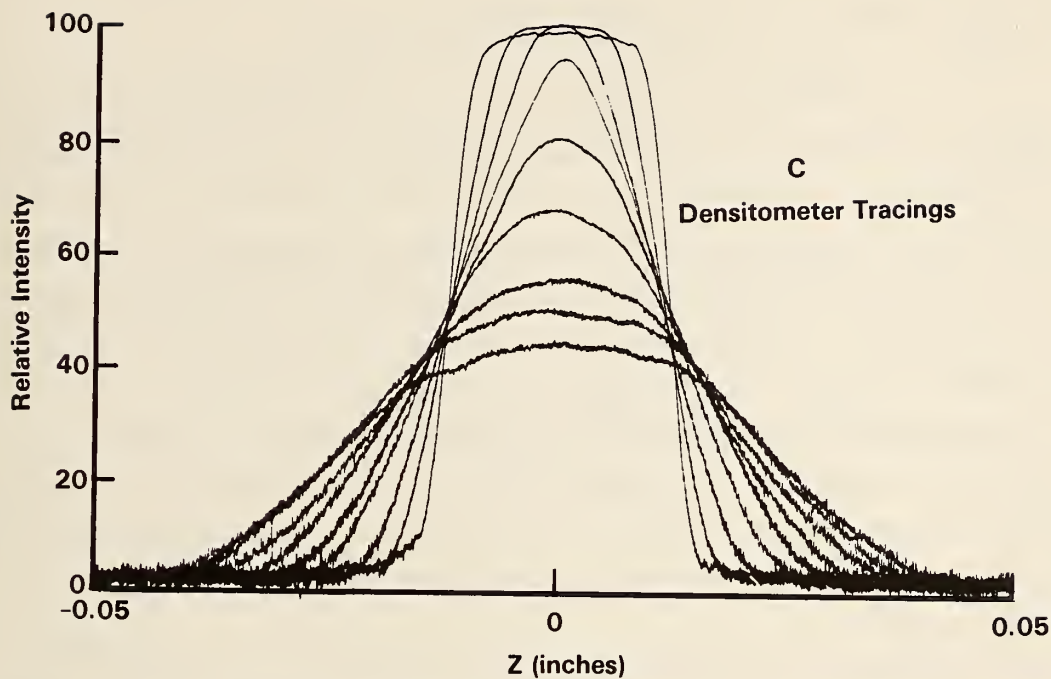


Figure 1(c). Densitometer tracings for radiograph with same parameters as figures 1(a) and 1(b).

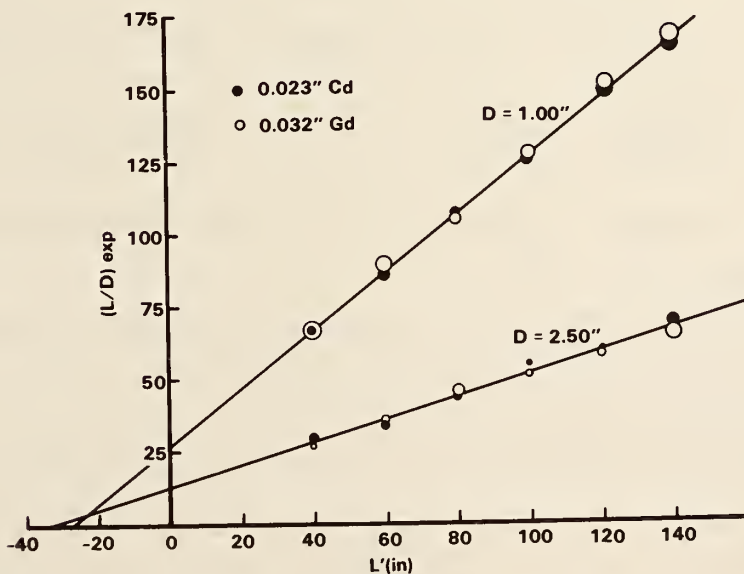


Figure 2. Measured values of $(L/D)_{\text{exp}}$ for NBS reactor.

is done, it is found that $a_{lav} = M(\pi/4)D/L$ and

$$(L/D)_{exp} = \pi M/4 a_{lav}. \quad \text{Circular-Linear (5)}$$

When $b < h < 2b$, the plot of w_d vs $h(1-h/L)^{-1}$ is still very close to a straight line. It can be shown that a_{ld} for this range will differ from that for $h < b$ by only a few percent. Since measurement errors are normally of this order of magnitude, the present technique uses a value of a_{ld} obtained for measurements for $0 < h < 2b$. Values of w_c for $h > b$ are not used and $a_{lav} = (a_{ld} + a_{lc-})/2$.

It is apparent that the effect of going to a circular source, at least when $h < b$, has been to replace D by $\pi D/4$. In other words, the normalized patterns for a circular source will approximate those for a linear source whose width is $(\pi/4)D$. This agrees very well with the experimental results.

The method described here which leads to equation (4) or (5) will be called the NBS method of determining L/D .

The NU method developed by the Aerotest Operations group uses only w_c . Linear regression is used to find an expression such as equation (2) for w_c which is then extrapolated to find the value of h for which $w_c = 0$. The resulting value of h shall be called b_{exp} . It is found that the resulting values of L/D are

$$(L/D)_{NU} = b_{exp}/d_o, \quad \text{Linear-Linear (6)}$$

$$(L/D)_{NU} = \pi b_{exp}/4d_o. \quad \text{Circular-Linear (7)}$$

2. Experimental Results

The NBS method of determining L/D has now been used at the NBS 10 MW Research Reactor and at three non-reactor-based facilities. The range of L/D measured is from 12 to 170.

Figure 2 shows the results of measurements from twelve radiographs taken at the NBS facility of the NBS test object described in the last report.¹ The size of the circles indicates the standard error. The straight lines were obtained by linear regression to fit the equation

$$(L/D)_{\text{exp}} = L_o/D + L'/D. \quad (8)$$

L' is measured from the face (biological shield) of the reactor and L_o , the distance of the source behind the reactor face is measured to be 32 inches.

The values of L_o and D resulting are within the standard error of what would be expected. Although a_{ld} and a_{lc} may differ by as much as twenty percent of their average, the NBS method appears to correct for whatever artifacts are producing the discrepancy.

Similar results have been obtained from the radiographs taken at the non-reactor-based facilities, thereby increasing confidence in the validity of the method.

The values of $(L/D)_{\text{exp}}$ derived from a set of radiographs taken with the same parameters as those for another set, but with a 0.070 inch lead sheet between the test object and the cassette, agreed with those derived from the normal set to within the standard error with the fluctuations being random. Accordingly it is felt that the results are not affected by capture gamma rays from the obstacles or background gamma rays from the reactor.

The values of $(L/D)_{\text{NU}}$ obtained from equation (6) or (7) agree generally to within 10 percent with the values of $(L/D)_{\text{exp}}$ obtained from equation (4) or (5); but the internal consistency of the results from the NU method does not seem to be as good as that from the NBS method.

The NBS method is preferred to the NU method for two reasons: first, it uses more of the available data. In fact, for small values of L/D , the number of measurements of w_d used will be at least twice the number of measurements of w_c used. Second, the NU method uses the value of d_o , which may not be known to the desired accuracy, while the NBS method depends only on the fact that all the obstacles have the same width.

-
1. W. L. Parker and D. A. Garrett, *NBS Techn. Note* No. 1117 (ed. F. J. Shorten, 1980).

RESOLUTION OF A RADIOGRAPHIC FACILITY

W. L. Parker and D. A. Garrett

The common measure of resolution in radiography is line pairs per unit length--usually per millimeter. For an array of parallel linear obstacles of the same width, d_o , separated by a distance between their sides equal to their width and situated at a given distance from the image plane, what is the minimum d_o for which adjoining objects will be recognized as separate? The resolution, n , will be a unit length divided by twice the minimum value of d_o .

What should be taken as the criterion for resolution? For the diffraction pattern of two parallel identical slits the Rayleigh criterion is that the first minimum of one pattern shall fall on the central maximum of the other. This results in the intensity midway between the two maxima being $0.8106 = 8/\pi^2$ times the maximum intensity.

For the following discussion it is convenient to introduce two dimensionless parameters defined as follows:

$$\alpha = b/h = Ld_o/2Rh, \quad (1)$$

$$\sigma = d_o/R = 2\alpha h/L \quad (2)$$

If the Rayleigh position criterion is applied to the shadow patterns it is found that the intensity at the midpoint of the composite pattern is about 1.33 times the maximum for either pattern alone in the linear-linear case, and about 1.14 times in the circular-linear case. The patterns will not be resolved.

An obvious solution, which will be called the "Rayleigh intensity criterion", is to make the midpoint intensity of the composite pattern be 0.8106 times the maximum intensity for a single pattern.

In the linear-linear case, when $b < h < 2b$, the two trapezoids overlap to give two trapezoidal "peaks" with an inverted trapezoidal "valley" in between. The Rayleigh intensity criterion gives the following result for the α required for resolution:

$$\alpha_{\text{res}} = (1+\sigma)/(1+8/\pi^2) \quad \text{Linear-Linear (3)}$$

The circular-linear case is more complicated and involves finding the value of α which will satisfy the equation

$$I(d_0)/I(0) = 4/\pi^2. \quad (4)$$

$I(z)$ is the normalized intensity of the shadow pattern at a point whose abscissa is z and involves both algebraic and inverse trigonometric functions. The ratio can be expressed as a function of α and σ only. For a given value of σ the resulting transcendental equation can be solved by Newton's method. The resulting values of α_{res} are found to be almost a linear function of σ , at least for small values of σ , given by

$$\alpha_{\text{res}} = 0.4494 + 0.566\sigma \quad \text{Circular-Linear (5)}$$

The expression is correct to better than a percent for the range $0 < \sigma < 0.10$.

Figure 1 is a plot of the composite shadow patterns (calculated for $\sigma = 0.0184$) which just meet the criteria for resolution. All intensities are normalized to the value of the maximum ($h < b$) for the linear-linear case (a square source whose side is equal to the diameter of the circular source).

Figure 2 shows the patterns for both sources calculated for the value of α which just gives resolution for the square source. Each pattern is normalized to its own maximum. It is obvious that if the pattern for the square source is just resolved, the pattern for the circular source is very well resolved.

Figure 3 shows the patterns for that value of α which just gives resolution for the circular source. The pattern for the square source is perhaps recognizable as being produced by two separate obstacles, but it is certainly not resolved in the usual meaning of the word.

It is convenient to introduce a parameter $k = 2\alpha_{\text{res}}$. Combining the definitions of n and α gives

$$k = (L/D)/nh \quad (6)$$

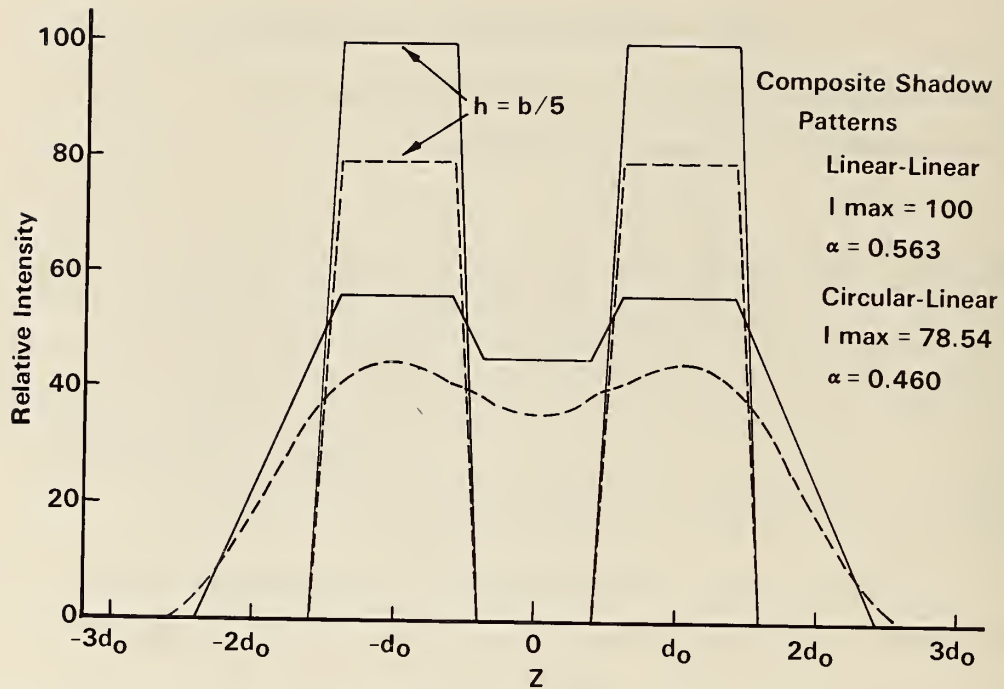


Figure 1. Patterns at the Rayleigh intensity criterion.

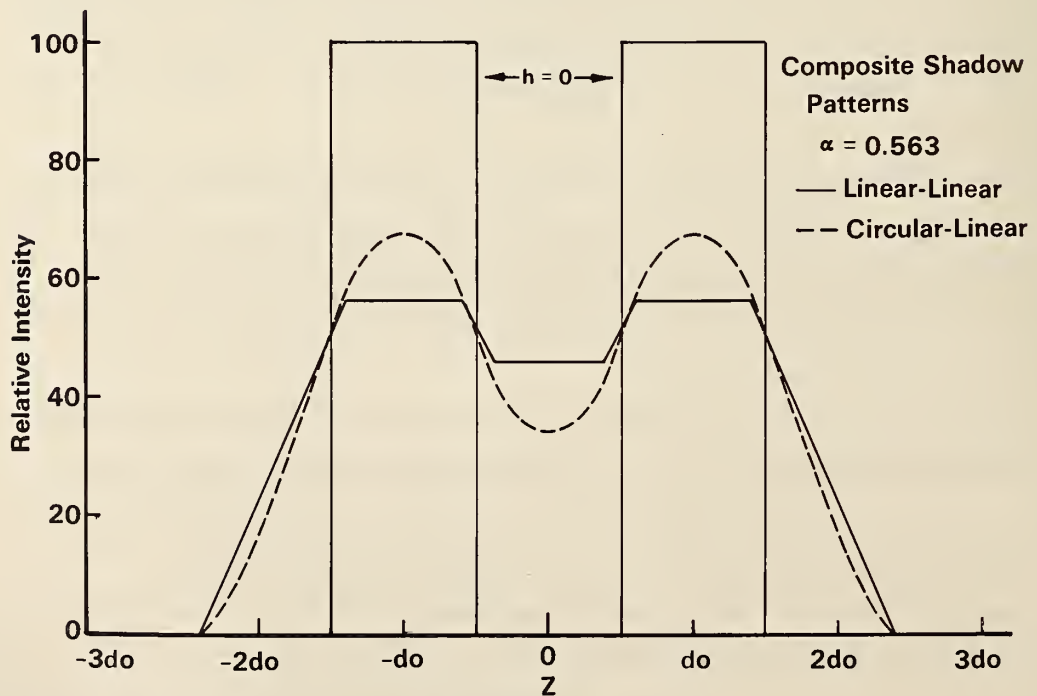


Figure 2. Patterns for Linear-Linear Resolution.

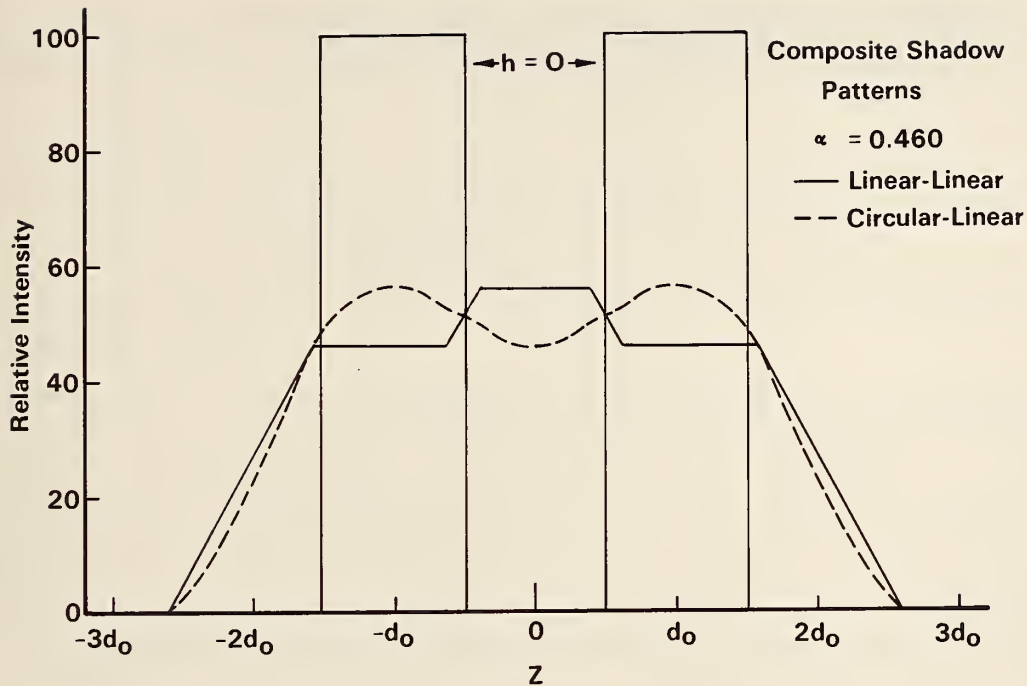


Figure 3. Patterns for Circular-Linear Resolution.

Equation (6) can be solved for any of the three quantities of interest:

$(L/D)_{\min}$, h_{\max} , or n .

In dealing with something as subjective as resolution accuracy to a few percent should be sufficient. It is found that a value of 0.02 for σ is representative of most of the cases which will be encountered. The standard values of k are taken to be those for $\sigma = 0.02$:

$k = 0.92$, Circular Source

$k = 1.13$. Square Source

As an example, the NBS facility was recently used to radiograph a small jet engine. The (L/D) was 170, and the source is circular. One of the regions of interest was 200 mm from the cassette. Equation (6) gives $n = 170/184 = 0.92$ line pairs per mm or about 23 line pairs per inch. Detail of the order of a millimeter would just be observed. Had a square source of the same size been used, the resolution would have been reduced to 19 line pairs per inch.

THE USE OF NEUTRON AND X-RADIOGRAPHY TO EVALUATE
LITHIUM/IODINE PACEMAKER BATTERIES

D. A. Garrett

and

R. C. Steinbring

(Wilson Greatbatch, Ltd., Clarence, NY)

and

M. Ganoczy

A program, initiated by the Food and Drug Administration (FDA), has used neutron radiography for studying internal changes in lithium/iodine batteries during accelerated discharge. Neutron radiographs were compared with x-ray radiographs and the results indicate that the two techniques are complementary to each other.

The lithium/iodine battery system is the most widely used power source for cardiac pacemakers and has amassed an outstanding reliability record.¹⁻²

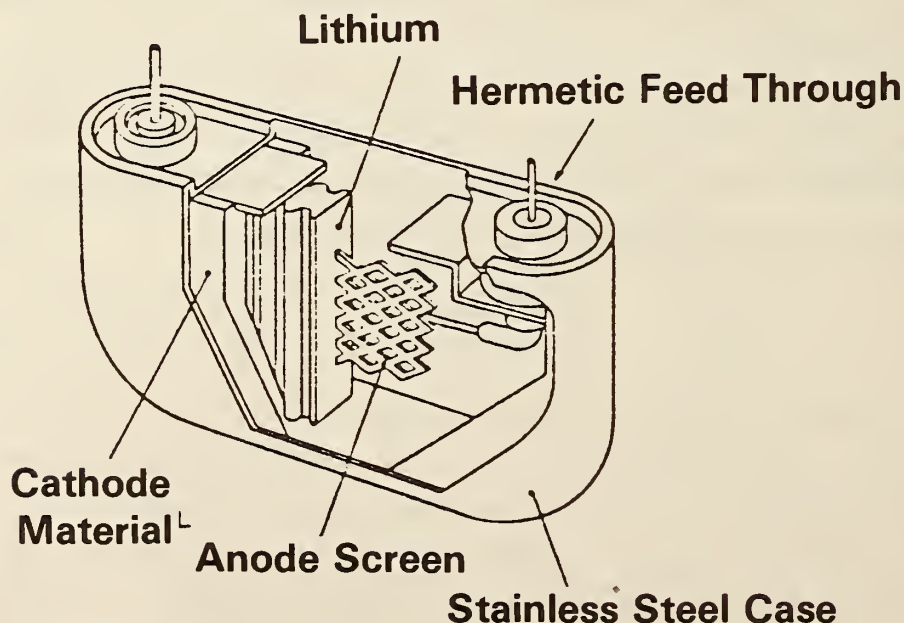


Figure 1. Sketch of a typical lithium/iodine battery showing various components and structures.

REACTOR RADIATION DIVISION PROGRAMS

Wilson Greatbatch Ltd., a major manufacturer of lithium/iodine cells, has supplied the batteries for this program. These cells consist, primarily, of:

- A. a central lithium anode
- B. the charge transfer complex of 20 parts iodine to 1 part polyvinylpyridine $(C_7H_7N)_n$.

These components are hermetically sealed in a stainless steel case as shown in figure 1.

In general, cells of this type have been designed to power cardiac pacemakers for periods greater than 5 years. The lithium-iodine reactions and the role of the polyvinylpyridine (PVP) have been studied and extensively evaluated by destructive techniques. However, this presentation describes the application and results of two nondestructive techniques utilizing neutron and x-radiography. The neutron radiographic portion of this program was funded by the Food and Drug Administration (FDA) and used the expertise and facilities of the National Bureau of Standards (NBS).

The x-ray exposures, accelerated discharge of the cells, and destructive test correlations were performed by the Reliability Group at Wilson Greatbatch Ltd. (WGL).

Eighteen cells from three typical WGL pacemaker battery models were utilized on this program. Only the results on one model, the 761/15, is discussed in this presentation since it was the only model which could be conveniently neutron radiographed in the vertical direction. Although neutron radiography is a very sensitive technique it requires lengthy time exposures. In this program, it was necessary to make 2 hour at a flux of 10^4 n - cm - sec - 1 neutron exposures to clearly define the inner structure of cells which are 8.6 mm thick and 15 mm high.

The neutron radiographic facility of NBS consists of a 10 megawatt nuclear reactor which utilizes enriched uranium (U-235) and is cooled and moderated by heavy water (D_2O). For the neutron radiographic purposes of this program, a thermal neutron flux of approximately 1.4×10^5 neutrons/cm²/sec was directed through a 5 inch beam tube. In order to minimize non-collimated neutrons the tube was lined with a lithium carbonate

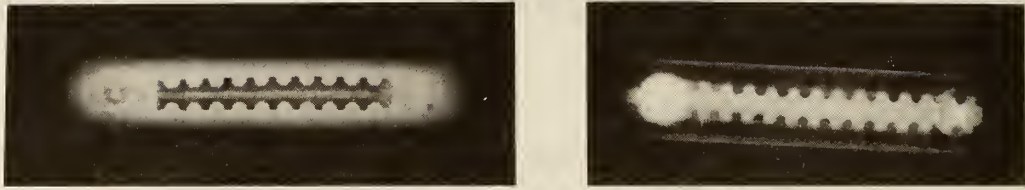


Figure 2. Comparative radiographs of a fresh Model 761/15 battery. Note the light anode in the neutron radiograph indicating strong neutron absorption and dark image in the x-ray illustrating low x-ray absorption.



Figure 3. Comparative radiographs of the same battery as shown in figure 2 but discharged .450 Ah. Note light areas on neutron radiograph which correspond to dark streaks on x-ray. These are probably areas of high PVP content.



Figure 4. Same battery as previous figures but discharged a total of .685 Ah. Note the void formations in upper right area. Also note the lithium iodide layer clearly outlined on the x-ray.

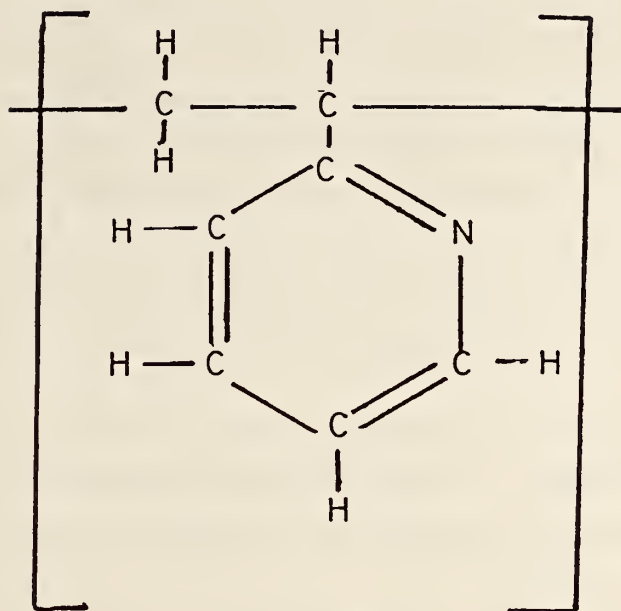


Figure 5. Sketch of the Polyvinylpyridine monomer showing the 7 hydrogen atoms, 7 carbon atoms and 1 nitrogen atom.

absorber. Also, it was necessary to use thick lead and bismuth filters to absorb high energy gamma rays which are also produced within the reactor.

The result is an excellent collimated beam of neutrons with a small apparent aperture, thereby producing a radiograph of excellent clarity and resolution. The batteries were positioned in this beam in front of a gadolinium (Gd) conversion screen which was held in firm contact with a single-emulsion type SR film by means of a vacuum cassette. This type of technique has been described more fully by H. Berger of NBS.³

The x-radiographs of the cells were made at the WGL facility with a 160 Kilovolt x-ray generator and using type AA industrial x-ray film.

The batteries were radiographed using the two NDT techniques as fresh batteries and, periodically, as they were discharged under controlled accelerated conditions in the WGL electrical test facility. The units were discharged by placing a 10K ohm load resistor across the terminals

and electrical readings were made periodically until the batteries had discharged approximately .2 ampere-hour (Ah) of their capacity. At this load, the model 761/15 will discharge .2 Ah in about 35 days.

The batteries were then shipped to NBS for the neutron radiographs and were subsequently returned to WGL for x-radiography and the next discharge cycle.

During this phase of the program the batteries were discharged .685 Ah in three stages, which is approximately 50% of the rated capacity of this model.

Upon completion of the latest test cycle one unit was cross-sectioned and the microscopic detail was compared to the radiographs of the techniques. The results show that the techniques are complementary and give considerable insight into cell dynamics.

It is well known that x-rays are generally absorbed in proportion to the atomic number and density of the material they pass through. As a result low density, low atomic number materials such as lithium ($N=3$) are relatively transparent to x-rays and as a result appear as dark images on the x-ray film. However, iodine ($N=53$) absorbs x-rays strongly and appears as a light or opaque film image.

Neutrons behave much differently in that they are absorbed by the process of neutron capture, or scatter, a nuclear process, which is dependent on the cross-sections of the atoms of the material being radiographed. As a result materials with low atomic numbers may exhibit high neutron absorbing cross-sections.⁴ Indeed, lithium is a good absorber and hydrogen ($N=1$) is one of the most efficient scatterers. Neutron and x-ray mass absorption coefficients relating to the battery materials are given in table 1.

It can be seen in figures 2A and 2B that the components of the cell are imaged quite differently and are nearly direct opposites in their dark and light images. The lithium anode can be clearly seen in both radiographs but is light in appearance on the neutron radiograph and dark in the x-radiograph.

As the cell was discharged to .450 Ah (figures 3A and 3B) the dark iodine rich areas are well defined on the neutron radiograph and fingers of cathode material containing hydrogen rich PVP, which have been partially depleted of iodine, can be readily seen as nearly white areas. In the x-ray image at this stage, the PVP rich areas show up as dark streaks.

In the next figures, 4A and 4B, where the cells have been discharged .685 Ah, several interesting features can be seen. These include the formation of voids at the inner case surface and the well defined lithium iodide layer in the x-ray image. It is interesting to note that the voids appear to be almost identical on both film images i.e., voids are seen as dark areas. The voids can be attributed to shrinkage of the internal ingredients due to the more dense lithium iodide formation. This shrinkage has been calculated and observed by other workers.⁵

At this stage of discharge approximately 2.8 grams of iodine have been used up in forming the lithium iodide layer. Since the charge transfer complex is becoming depleted of iodine the hydrogen component of the PVP monomer takes on a much more prominent role in the neutron absorption process. As shown in figure 5, the PVP monomer contains seven hydrogen atoms in addition to 7 carbon atoms and 1 nitrogen atom giving a total monomer weight of 105. Since hydrogen has an absorption cross-section of 48.5, it's presence can be used as a tracer for locating and tracking the PVP.

In the original fresh battery, the iodine to PVP weight ratio in the charge complex was 20:1. At this stage of discharge (.685 Ah) the ratio has now changed to approximately 14:1 or an increase in concentration of PVP of about 1.4 times. While the hydrogen constituent is only 7/105 of this, it becomes very significant because of it's very high absorption coefficient.

In figure 4A, the PVP shows up as light areas positioned between the corrugations of the anode. In the corresponding x-ray image the PVP shows up as dark streaks. These areas can also be seen on the cross-section of this battery (figure 6).

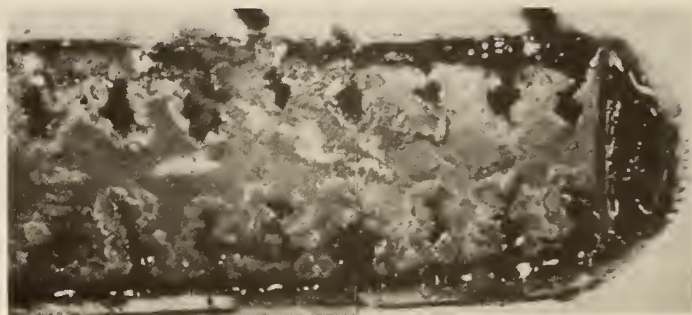


Figure 6. Cross-section of WGL 761/15 cell after .685 Ah discharge showing Lithium, Lithium Iodide layer, Iodide-PVP charge transfer complexes and voids.

Table 1. Mass Absorption Coefficient of Lithium/Iodine Battery Components.

	NEUTRON	X-RAY
Lithium	3.7 units	.125
Iodine	.036	1.33
Hydrogen (in PVP)	48.5	.28
Carbon (in PVP)	.26	.142
Nitrogen (in PVP)	.48	.143
PVP Composite	3.5	.152

It can be seen from this series of comparative radiographs that the two techniques give considerable insight into the battery dynamics. By using the techniques to complement each other and by utilizing the mass absorption coefficients it is possible to track the battery constituents as a function of cell discharge. Neutron radiography offers significant information on systems of this type as a function of cell discharge. It's nondestructive nature makes it an extremely valuable tool.

1. Greatbatch, W. *Proc. of Symposium on Power Sources for Biomedical Implantable Applications*, 1980, pp. 3-15.
2. Liang, C. C. and Holmes, C. F., "Performance and Reliability of the Lithium/Iodine Battery" *Journal of Power Sources* 5 (1980), pp. 3-13.
3. Berger, H. "Detection Systems for Neutron Radiography" *Standardization News, ASTM* Vol. 4, No. 3 1976.
4. Garrett, D. A., Berger, H. "The Technological Development of Neutron Radiography" *Atomic Energy Review* 15 2 (1977).
5. Skarstad, P. M., Owens, B. B., Untereker, D. F. "Volume Changes on Discharge in Lithium/Iodine (PVP) Cells" Abstract 23 *Proceedings of Electrochemical Soc.* Vo. 77-2, Oct. 1977.

THERMAL NEUTRON IMAGING SCREEN DEVELOPMENT

D. A. Garrett and J. J. Barrow

The most efficient method of imaging thermal neutron beams is utilizing a physical mixture of ${}^6\text{LiF}$ and $\text{ZnS}(\text{Ni})$ suspended in a low Z binder which is transparent to the light emission of the $\text{ZnS}(\text{Ni})$. The ZnS is caused to fluoresce by the decay products from the ${}^6\text{Li}(\text{n}, {}^3\text{H}) {}^4\text{He}$ reaction. A light-sensitive film is employed to register the imaged neutron beam.

One problem encountered with this type of screen is that it is partially transparent to the light generated in the screen matrix, one contributing factor to the grainy image produced. We proposed to produce a segmented screen which is divided into a pixel matrix, preventing cross-talk and subsequent graininess in the finished radiography. In other words, the radiograph would appear as newsprint on a microscopic scale. Although this in itself represents grain, if properly fabricated, each pixel would be of uniform density.

The first problem to be solved was to locate a binder which was neither exothermic, i.e., a two component mix, nor one which depended upon volatilization for setting. Either of these phenomena would cause difficulties in fabrication since it has been decided to extrude the $^6\text{LiF/ZnS}$ into a fine mesh, e.g. 500 lines/in, between two fused quartz plates coated with mold release. Mixture shrinkage or nonvolatilization would have resulted.

We decided to attempt to employ a UV curing optical cement as the binder. To accomplish this, a mold release had to be coated on each of the quartz plates. Several silicone mold releases were tried, however cured under the influence of the UV radiation. It was found that a common household grease release used in the kitchen, would work, but was messy. It was then discovered through the adhesive manufacturer, that certain mylars would pass the UV curing the adhesive, however not adhering to the adhesive. These were tried with success.

Several parameters in the $^6\text{LiF/ZnS}$ must still be determined, e.g., light output as a function of particle size, LiF/ZnS ratio for optimum light emission and the amount of binder required for a stable screen. Using 30μ dia particles of each component, the optimum LiF/ZnS ratio appeared to be a bell-shaped curve centered at the 50 w/o LiF -50 w/o ZnS ratio. The error bars were quite large, however, and methods of achieving a high degree of reproducibility must still be developed. the 50 w/o/50 w/o mixture determination did differ from previous work in the field.

INCLUSION OF PROTON SPIN IN THE TUNNELING WAVE FUNCTIONS FOR TRIANGULAR MOLECULES OF THE TYPE XH_3 IN SOLIDS

R. C. Casella

I have done a group-theoretical analysis of the combined space-spin tunnel states for such systems, of which the CH_3 group in nitromethane (CH_3NO_2) is an example. The latter has been studied extensively by S. F. Trevino via neutron scattering (among other) techniques.¹ My analysis employs an approximation due to A. Hüller. For sufficiently strong covalent bonding, the probability of single-proton exchange is small compared with that for double exchange of the protons. The latter results from a rigid rotation of a molecule through tunnel barriers in a solid and does not require breaking a covalent bond. In an approximation where one ignores bond breaking entirely, the only requirement of the Fermi statistics is that the wave function be totally symmetric under double exchange. Since, for a triangle, the improper rotations (reflections) correspond to single proton exchange, I consider only proper rotations. In the absence of spin, the two non-trivial irreducible representations, T_1 and T_2 , stick together as a consequence of time-reversal symmetry, T . The three spin-1/2 protons allow construction of spin states with total spin 3/2 and 1/2. Using double-exchange projection operators, I have constructed spin states which are eigenstates of the S^2 Casimir operator and which belong to the irreducible representations A, T_1 , or T_2 . Time reversal invariance, in the guise of Kramer's degeneracy, again plays a role. I have combined the spin and space wavefunction to construct tunnel states which include both spin and T -invariance effects. I have also considered the case when one can no longer neglect the breaking of covalent bonds, constructing states which are totally antisymmetric under single proton exchange. Generally, the effect of bond breaking is expected to result in small fine-structure splitting when the rigid molecule approximation is a good one. Further work in this area is planned.

NEUTRON-ANTINEUTRON OSCILLATIONS

R. C. Casella

Recent gauge theories unifying the strong with the electroweak interactions have led to the possibility that baryon number, B may not be conserved.¹ The previously unquestioned rule, $\Delta B = 0$, provides, for example, for the stability of the proton against the decays $\text{proton} \rightarrow \text{positron} + \text{photon}$, $\text{proton} \rightarrow \text{positron} + \text{pions}$, etc.. It does so by assigning $B = 1$ to the proton and $B = 0$ to the decay products on the right hand side of these reactions. The deep mine experiment of Reines yields an upper bound on the rate of the ($|\Delta B| = 1$) decay of the proton; the reciprocal is an experimental lower bound on the proton lifetime, namely 10^{30} years. Once the $\Delta B = 0$ rule is challenged, the possibility of $|\Delta B| = 2$ process such as oscillations between neutrons ($B = 1$) and antineutrons ($B = -1$) enters. Because of a recent proposal² to employ the NBS reactor for the purpose of setting a bound on the period of (or discovering) those conjectured oscillations I have begun a study of the associated phenomenology. Provided the ambient magnetic field is suitably suppressed, I find that, for sufficiently short flight times t

$$P_n(t) = (\omega t)^2. \quad (1)$$

Here, $P_n(t)$ is the probability that a neutron released from a nucleus at $t = 0$ will, upon interaction with a target at time t , be found to have converted to an antineutron by an ideal detector of, say, the annihilation products. For a flight path ~ 10 meters, a thermal neutron of speed $\sim 10^3$ meters/sec. will impinge on a target at $t \sim 10^{-2}$ sec.. There exist two crude theoretical estimates³ for ω : $\omega \sim 10^{-6}$ sec.⁻¹ and $\omega \sim 10^{-5}$ sec.⁻¹. From Eq.(1), these estimates imply that 10^{10} neutrons per second impinging on a target-detector of 100% efficiency will yield a count rate of ~ 30 counts per year and ~ 10 counts per day, respectively. For $t = 10^{-2}$ sec., it is necessary that the ambient magnetic field be reduced

1. S. F. Trevino and W. H. Rymes, preprint (1979).

to $\lesssim 10^{-3}$ gauss along the flight path for Eq.(1) to hold. A more detailed report of these preliminary findings, which are in essential agreement with other studies,⁴ is being prepared.

-
1. J. C. Pati and A. Salam, *Phys. Rev. Lett.* 31, 661 (1973), H. Georgi and S. L. Glashow, *Phys. Rev. Lett.* 32, 438 (1974). R. N. Mohapatra and R. E. Marshak, *Phys. Rev. Lett.* 44, 1316 (1980).
 2. W. C. Sauder, private communication.
 3. The smaller estimate is due to S. Glashow (Lectures at Cargese Summer School, 1979) and the larger is due to Mohapatra and Marshak, Ref. 1.
 4. These may be found in various unpublished preprints by M. Baldo-Ceolin, by R. Mohapatra and R. Marshak and by R. Wilson.

MICROSCOPIC REVERSIBILITY, TIME-REVERSAL INVARIANCE, AND THE BOLTZMANN H-THEOREM

R. C. Casella

This very old subject has resurfaced in three contexts. (i) Microscopic time-reversal invariance T is known to be broken, as a consequence of the observed CP violation in the neutral K meson system, either by invoking the CPT theorem, or by direct analysis of the juxtaposition of data from several experiments.¹ (ii) Deviations from equilibrium play an important role in recent theories explaining the preponderance of matter vs. antimatter in the Universe.² (iii) Molecular dynamics calculations often begin with distributions which deviate from equilibrium and actually follow the approach thereto. My analysis, thus far, is limited to quantum statistics. Two ways of obtaining the H-theorem are considered. The first employs microscopic reversibility, $A_{ba} = A_{ab}$, where A_{ba} is the probability per unit time for a system to undergo a transition from the state $|a\rangle$ to the state $|b\rangle$. The second does not assume microreversibility, invoking only unitarity of the Heisenberg S-matrix. Both start with the assumption that the temporal evolution of the distribution among states of an ensemble of isolated physical systems is governed by a master equation,³

$$dP_a/dt = \sum_b (A_{ab}P_b - A_{ba}P_a). \quad (1)$$

$P_a(t)$ is the probability that an arbitrarily selected system is in the state $|a\rangle$ at time t . In terms of the S matrix, I find

$$A_{ba} = 2\pi |t_{ba}|^2 \delta(E_b - E_a) \quad (2)$$

where $S = 1 + iT$ and t_{ba} is an element of the reduced T matrix

$$T_{ba} = 2\pi t_{ba} \delta(E_b - E_a). \quad (3)$$

In terms of the entropy,

$$S = - \sum_a P_a \log P_a, \quad (4)$$

the H-theorem reads,

$$dS/dt \geq 0. \quad (5)$$

Assuming microreversibility, the master equation becomes

$$dP_a/dt = \sum_b A_{ab} \times (P_b - P_a). \quad (6)$$

From Eq. (4) and Eq. (6),

$$dS/dt = \sum_{a,b} A_{ab} \times (P_a - P_b) \log P_a. \quad (7)$$

Again using $A_{ab} = A_{ba}$, Eq. (7) can be written in the form

$$dS/dt = \frac{1}{2} \sum_{a,b} A_{ab} \times (P_a - P_b) \log (P_a/P_b). \quad (8)$$

Since the right-hand side of Eq. (8) is manifestly positive, the H-theorem follows immediately.

Unitarity of the S matrix implies

$$\sum_b A_{ba} = \sum_b A_{ab}. \quad (9)$$

Thus, Eq. (6) follows from Eq. (1), even when microscopic reversibility does not hold. That is, even if $A_{ba} \neq A_{ab}$, Eq. (6) and Eq. (7) are still valid, but Eq. (7) no longer implies Eq. (8). Nevertheless, from the property that $S = \sum_a f(P_a)$, where $f(P)$ is a concave-downwards function of P , the H-theorem can be shown to follow from Eq. (6) and Eq. (9).

By relating the coefficients A_{ba} directly to the S-matrix elements,

S_{ba} , it is possible to examine the effect of various symmetry operators of S on the master equation. These operators include T = time reversal, P = parity, and C = charge conjugation, alone or in various combinations, such as CPT . I find that T invariance does not necessarily imply the microscopic reversibility condition, $A_{ba} = A_{ab}$. However, under special circumstances, such as a system of spinless particles, the combined PT operation does; whence, if P is a good symmetry, T -invariance and microscopic reversibility are then equivalent. Also, in first Born approximation, hermiticity of the interaction hamiltonian leads to microscopic reversibility, independently of whether the hamiltonian is invariant under C , P , or T , alone or in combination. However, this result does not generalize to higher orders in the perturbation expansion since the T-matrix is generally not hermitian. (If it were, the optical theorem would imply zero cross sections for all reactions.)

Breakdown of microreversibility generally leads to the well-known Poincaré cycles. But this does not contravene the result that, for an isolated system in equilibrium, all states, $|a\rangle$, $|b\rangle$, $|c\rangle$, ... which are somehow interconnected by the master equation (and, hence lie on the energy shell) are equally probable. This fact, together with the CPT theorem, has implications with respect to the net generation of matter in the early Universe.² I plan to investigate this and related questions somewhat further.

-
1. R. C. Casella, *Phys. Rev. Lett.* 21, 1128 (1968), 22, 554 (1969), and references therein.
 2. S. Weinberg, *Phys. Rev. Lett.* 43, 1566 (1979). F. Wilczek and A. Zee, *Phys. Rev. Lett.* 43, 1571 (1979).
 3. C. N. Yang and C. P. Yang, preprint (1979) and references therein.

COLOR GRAPHICS AND IMAGING SYSTEM

N. F. Berk and J. M. Rowe

An important component of the SANS data acquisition and processing facility being developed here¹ is a new color graphics and imaging system which will be used to display and analyze data from the area detector. The system comprises a high-resolution raster scan color TV monitor for image display, associated video boards and a microprocessor for picture and color control, and an interface with our minicomputer for software image processing.

The imaging function of the device can be viewed in mathematical terms as producing a mapping of a two-dimensional data field onto a color field. Specifically, each element of the area detector can be mapped onto a picture element of the video monitor and assigned a color value according to the value of the measured scattering intensity. In this way the neutron data can be immediately visualized as a new data field in which regions of equal scattering intensity are at once identifiable by their colors. Moreover, the color mapping function can be manipulated interactively without erasing the image from the screen. This makes it possible to visually average the data in different ways and to probe regions of the data field in great detail while the image is being displayed. We anticipate that these capabilities will have a significant impact on the processing and analysis of small angle neutron spectra, particularly when they are complex and strongly anisotropic.

Since installing the imaging system in early 1980, we have been learning its many characteristics and have devoted a considerable effort to improving and extending the software package supplied by the vendor. We have also developed our own image processing programs and have undertaken preliminary applications of the system to simulated small angle data. In addition, we are hopeful of developing other scientific applications of the new imaging device. For example, we have explored its use in the display of real-time random walks of various kinds, including self-avoiding walks in which path color serves to identify previously visited points without

having to store a large vector in the host computer.

-
1. C. J. Glinka, J. M. Rowe, and J. G. LaRock, this report.

THE SMALL-ANGLE SCATTERING FACILITY

C. J. Glinka, J. M. Rowe and J. G. LaRock

The new facility for small-angle neutron scattering (SANS) described in the 1979 progress report¹ is presently under construction at the NBSR. An overhead and side view of the design of the new instrument is shown in figure 1.

The key element of the SANS instrument is a large area position sensitive proportional counter which will enable data over the entire small-angle region to be recorded simultaneously. Two area detectors of the Borkowski-Kopp type² have been purchased³ for the instrument, a primary detector with a 65cm X 65cm sensitive area and a smaller back-up detector with an active area of 25cm X 25cm. To date, the smaller detector has been received and has met all performance tests. For example, figure 2 shows a typical measurement of the spatial resolution and linearity of the 25cm X 25cm detector. For this measurement a cadmium mask with a row of 1.5mm diameter holes spaced 2.5cm apart was placed over the face of the detector which was then scanned through a collimated 1cm diameter neutron beam. The detector response is linear to a high degree as can be seen by the open circles in figure 2 which are the channel numbers of the measured peak positions on the right-hand scale. The spatial resolution of the detector is given by the peak width which are 4mm (FWHM).

The data acquisition system associated with the area detector, shown schematically in figure 3, has been assembled and is now undergoing testing. The positional information for each neutron detected is contained

NBS SANS SPECTROMETER

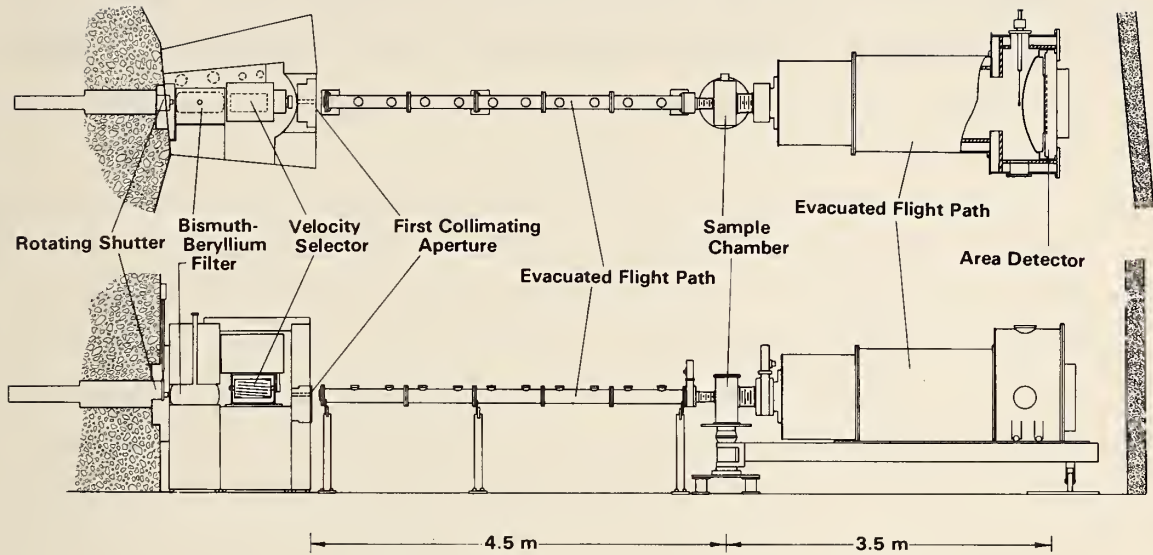


Figure 1. Overhead and side views of the layout of the new SANS facility.

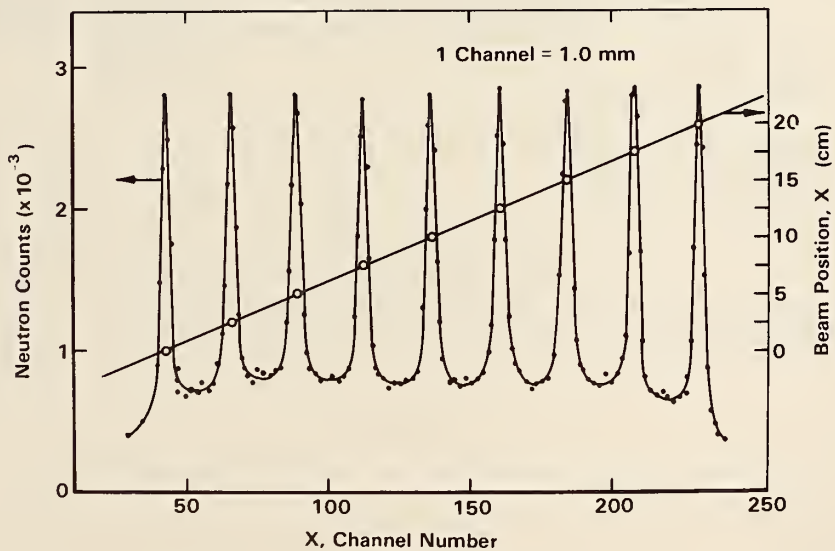


Figure 2. A typical measurement of the resolution and linearity of the 25cm X 25cm area detector for the SANS facility made by stepping a 1.5mm diameter beam across the detector in 2.5cm steps.

in the difference in rise times between the pulses produced at the two ends of each cathode². The two time intervals, for the x and y directions, are directly digitized by counting pulses from a crystal controlled 125Mhz are directly digitized by counting pulses from a crystal controlled 125Mhz

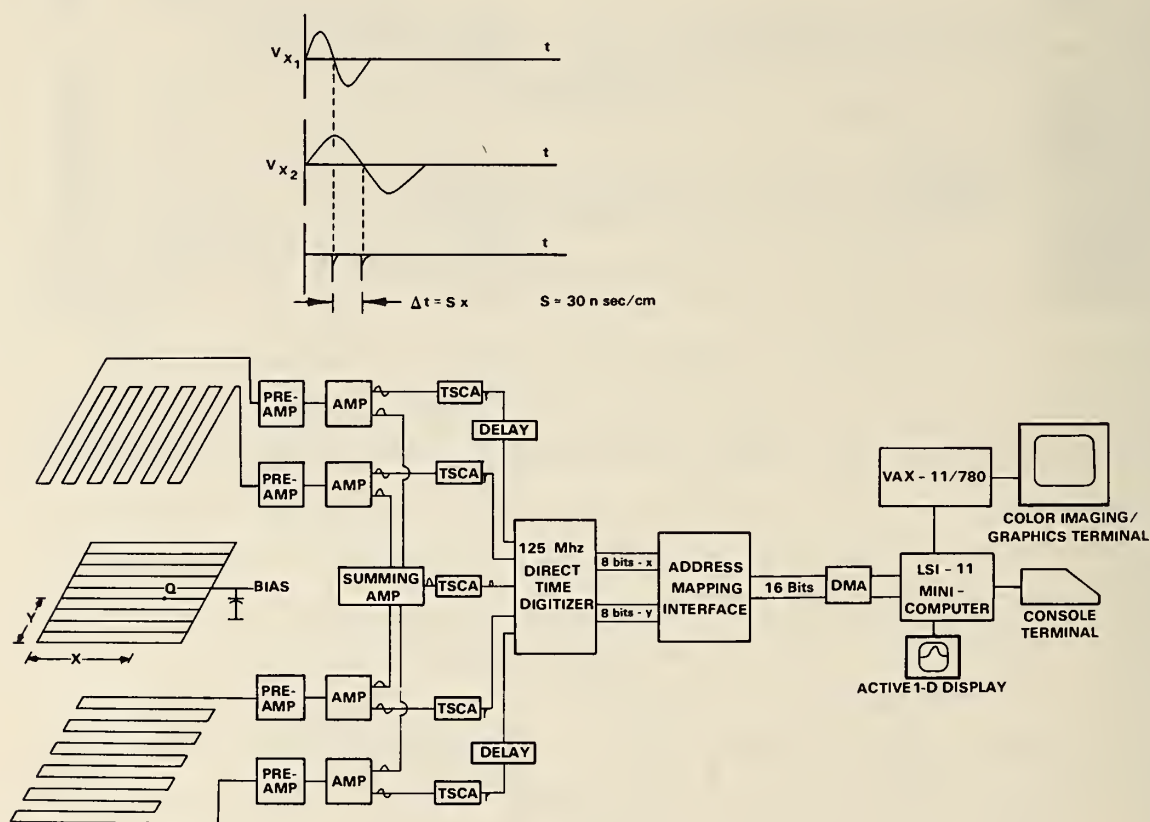


Figure 3. A schematic layout of the data acquisition system for the new SANS facility.

clock. Such a direct time digitizer⁴ eliminates the conversion time and reliance on analog signals inherent in the more conventional time interval measurement by means of a time-to-amplitude converter followed by an analog-to-digital converter. The clock frequency chosen provides 8-bits, or 256 channels, for both x and y directions. A custom hardwired interface then forms a 16-bit memory address from the digitized positional information. A standard DMA interface is used to transfer the address to a dedicated minicomputer which increments the corresponding location and checks for overflow. The throughput of this data acquisition system has been measured to exceed 50Khz and thus the maximum data rate of the system is limited by the detector response only ($\sim 20,000$ cps). An active display of one row of detector pixels will be provided to visually monitor the data collection. A completed data set can then be transferred to a VAX11/780 computer for data reduction and display on a color imaging terminal.

Delivery of the larger area detector is scheduled for the early Fall of 1980. The detector flight path and other mechanical components of the instrument are to be completed at about the same time. Full operation of the new SANS facility is anticipated in early 1981.

-
1. C. J. Glinka, et al., *NBS Tech. Note 1117*, F. Shorten, Ed., 33(1980).
 2. C. J. Borkowski and M. K. Kopp, *Rev. Sci. Instrum.*, 46, 951(1975).
 3. Technology for Energy Corp., Knoxville, TN.
 4. Designed and built by the Electronics Division, Argonne National Laboratory.

ErFe₂ -- FINITE TEMPERATURE SPIN WAVES

J. J. Rhyne

and

N. C. Koon

(Naval Research Laboratory, Washington, DC)

Magnetic spin excitations in the Laves-phase structure compound ErFe₂ have been studied previously in this laboratory^{1,2} at 4 K and at room temperature primarily. The observable 4 K ground state excitations shown in figure 1 consist of an in-phase spin precession acoustic mode with an anomalously large $q = 0$ gap of 8.3 meV plus a dispersionless mode representing an out-of-phase precession of the rare earth spins. The lack of dispersion reflects the vanishingly small exchange coupling between the rare earth spins. A higher energy in-phase mode of the iron spins is not shown in the figure.

At room temperature the acoustic mode shows essentially the same dispersion but is gapless. The flat optic mode remains degenerate at the zone boundary. Previous studies of the intermediate temperature behavior² of this flat mode revealed that both the low (c.f. 295 K) and high (c.f. 4 K) energy modes could be observed simultaneously with no apparent shift in energy as the temperature was varied. The intensity did, however, smoothly shift from the high energy excitations into the low energy mode as the temperature increased in a manner suggesting a magnetic exciton effect. A molecular field calculation² did, in fact, confirm this excited state spin wave behavior.

Mean field models can not account for the temperature or wave-vector dependence of the dispersive acoustic modes. Recently, careful measurements have been made of the acoustic mode at intermediate temperatures and have been compared to the results of a Greens function random phase approximation calculation.³ Figure 1a shows the calculated dispersion curves at room temperature and illustrates the large number of in-phase (dispersive) and out-of-phase (nondispersive) modes which

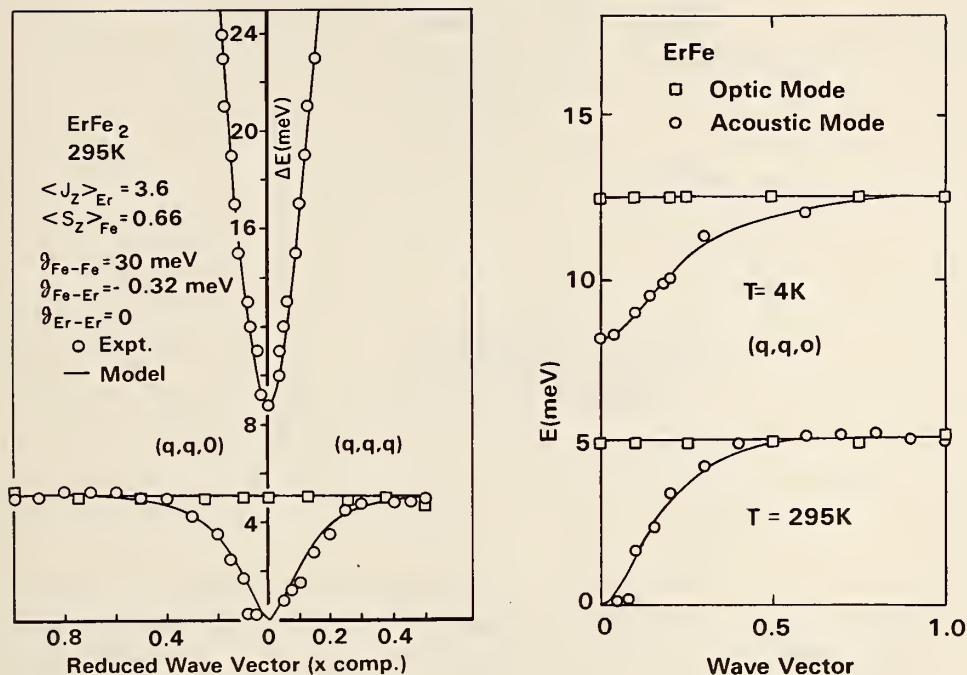


Figure 1a. Room temperature spin wave modes found for ErFe_2 (b) distinct high and low temperature pairs of in-phase (acoustic) and out-of-phase (optic) modes observed for ErFe_2 at 4 K and at 295 K.

are degenerate at the zone boundary. These modes originate from transitions between adjacent magnetic levels, and all but one pair represent excited state spin waves. The model calculation predicted two salient features which were checked by experiment: (1) the "acoustic" mode at room temperature shown in figure 1 actually consists of two separate modes (see figure 2) whose intensity varies inversely with q in such a manner as to appear to be one mode in a moderate resolution experiment. High resolution scans at 80 K for $q = 0.1$ did in fact confirm the existence of the two distinct in-phase modes as seen in figure 3 at almost precisely the predicted energies and relative intensities (Gaussian fitted solid lines in figure). (2) the model also predicted that the $q = 0$ intercept of the groundstate acoustic mode (higher energy dispersive mode in figure 1b) should increase with temperature. A careful study of the modes at $q = 0.1$ revealed this temperature depen-

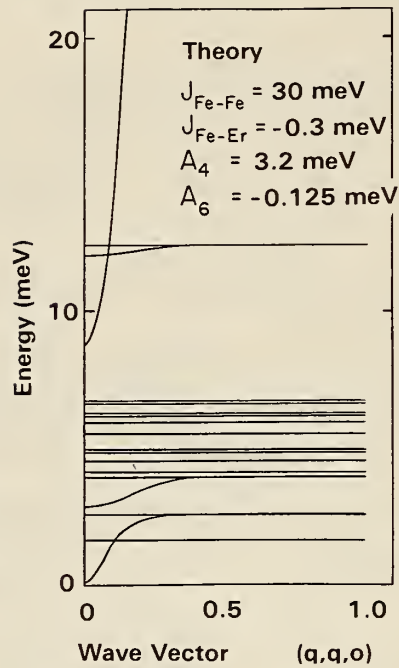


Figure 1c. Room temperature modes predicted by RPA theory for ErFe_2 using experimentally determined exchange and crystal field parameters. At the zone boundary in-phase (dispersive) and out-of-phase (flat) components of each mode are degenerate.

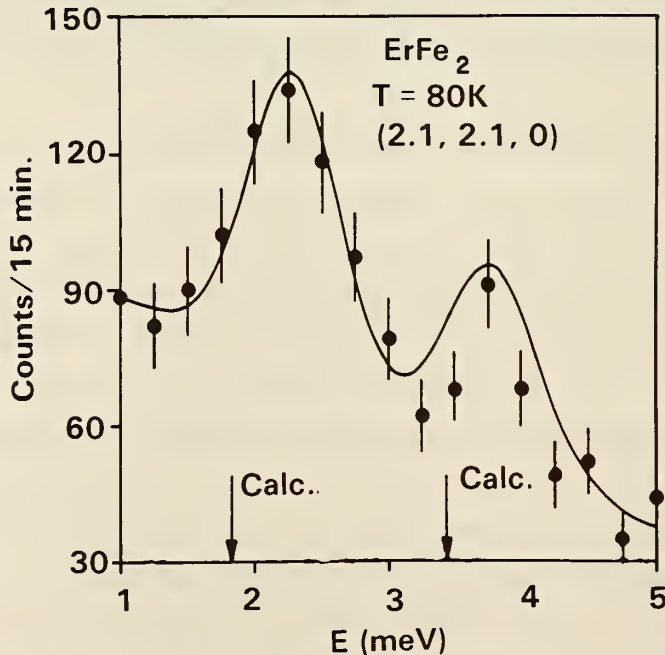


Figure 2. Simultaneous observation of two low lying dispersive modes which make up the single "acoustic" mode of figure 1a. The solid lines give the relative intensity as predicted by the RPA model.

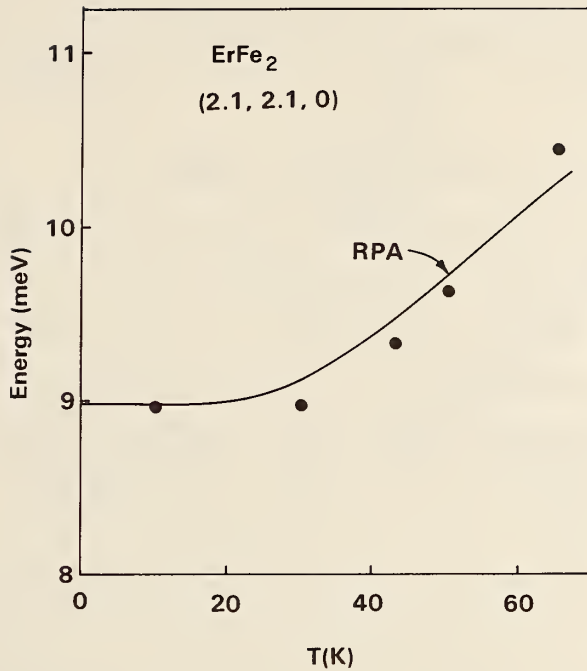


Figure 3. Temperature dependence of the energy of ground state acoustic mode of $q = 0.1$ compared to the prediction of the RPA model.

dence in very close agreement with theory as shown in figure 3.

These experimental results and the agreement with the RPA model calculation provides a relatively complete insight into the finite temperature excitations in ErFe_2 .

-
1. J. J. Rhyne and N. C. Koon, *J. Appl. Phys.* 49, 2133 (1978).
 2. N. C. Koon and J. J. Rhyne, *Solid State Commun.* 26, 537 (1978).
 3. N. C. Koon and J. J. Rhyne, *Intl. J. Magnetism* (proc. ICM, Munich, 1979), to be published in 1980.

TEMPERATURE RENORMALIZATION OF SPIN WAVE ENERGIES IN HoCo_2

J. J. Rhyne

and

N. C. Koon

(Naval Research Laboratory, Washington, DC)

The Laves-phase compound HoCo_2 has the $[110]$ direction as the easy magnetic axis at low temperature. In the range 12–16 K, the spin direction gradually changes from the $[110]$ direction into the $[100]$ direction. This shift in easy axis accompanies a rather large change in crystal field energies which is directly observable by neutron scattering.¹

Figure 1 shows the observed ground state modes in HoCo_2 at 4 K. The two flat modes are crystal field-like transitions from the ground state to first and third excited states as seen from the energy level

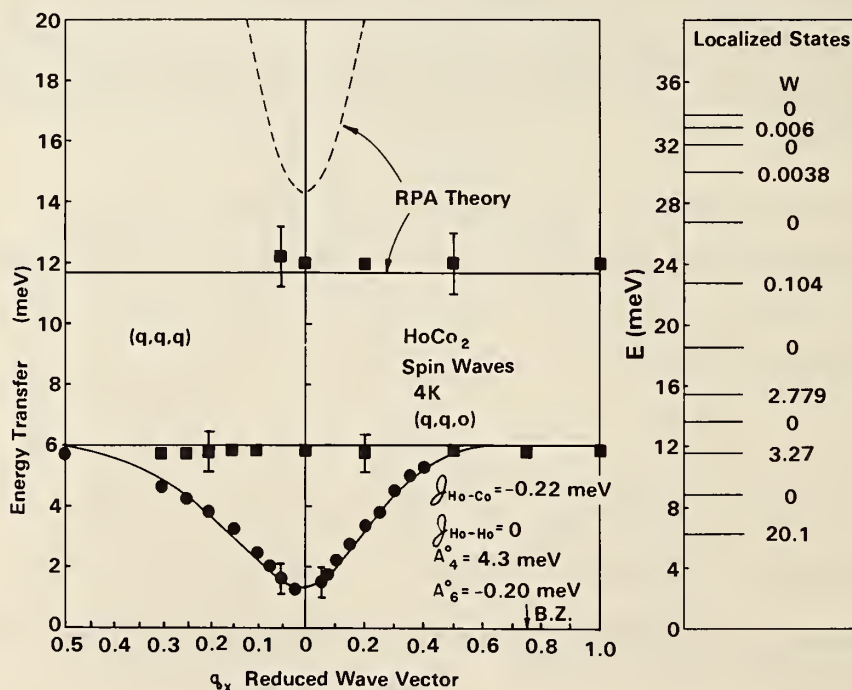


Figure 1. Dispersion relation for HoCo_2 at 4 K for the $[110]$ easy axis direction. The solid lines and the energy level diagram are the result of an RPA calculation using the exchange and crystal field parameters shown.

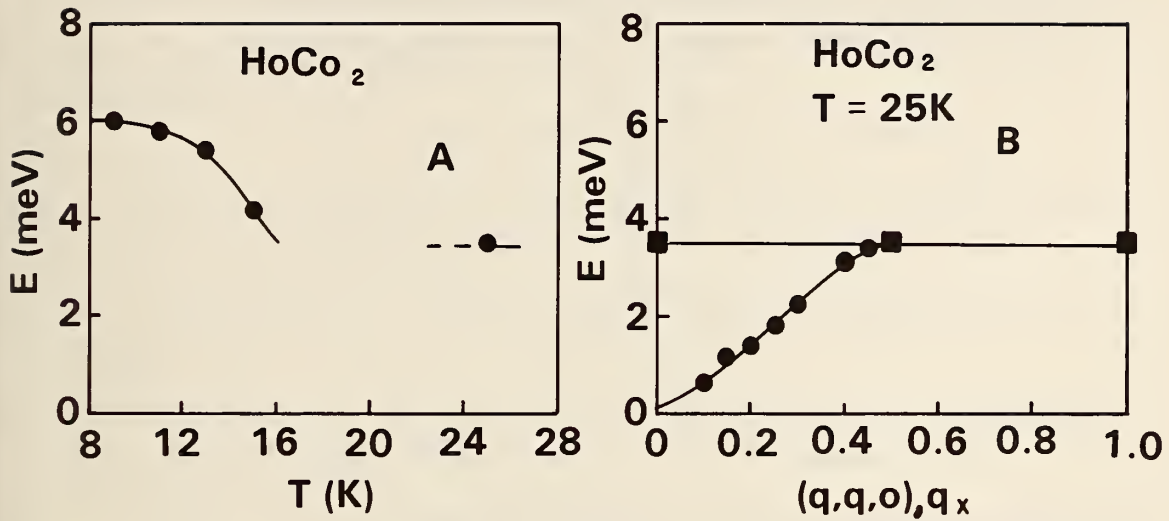


Figure 2. (a) Lowest optic mode energy in the spin reorientation temperature range. The spins slowly rotate from the $[110]$ direction to the $[100]$ direction in this temperature range. (b) Dispersion curve for two lowest modes above the spin reorientation temperature along the $[q,q,\phi]$ propagation direction.

diagram on the right. The dispersive modes arise from an in-phase precession of the spins with the upper one reflecting only the cobalt sublattice. This mode has not been observed in the present work nor was it seen in ErCo_2 . The solid lines are the result of a Green's function random phase approximation (RPA) calculation of the mode energies using the exchange and crystal field parameters shown.

Figure 2a shows the effect of the spin reorientation on the energy of the lowest out-of-phase mode in the range below 25 K. The mode energy drops slowly from about 6 meV at 4 K to 3.6 meV when the reorientation is fully complete near 16 K. The dispersion curves for the acoustic and lowest optic modes above the reorientation temperature are shown in figure 2b.

1. N. C. Koon and J. J. Rhyne, Crystalline Field and Structure Effects in f-Electron Systems, edited by J. E. Crow, R. P. Guertin, T. W. Mihalisin, Plenum Publishers, p. 125 (1980).

SPIN GLASS-FERROMAGNETIC PHASE TRANSITION
IN AMORPHOUS $(\text{Fe}_x\text{Ni}_{1-x})_{.75}\text{P}_{.16}\text{B}_{.06}\text{Al}_{.03}$

J. W. Lynn

(University of Maryland, College Park, MD)

and

(National Bureau of Standards, Washington, DC)

and

J. J. Rhyne

and

H. S. Chen

(Bell Telephone Laboratory, Murray Hill, NJ)

The amorphous magnetic metal-metalloid systems such as $(\text{Fe}_x\text{Ni}_{1-x})_{.75}\text{P}_{.16}\text{B}_{.06}\text{Al}_{.03}$ have been found^{1,2} to be excellent examples of three-dimensional isotropic ferromagnets at high Fe concentrations. With the addition of nickel, which in this material behaves as a non-magnetic diluent, the transition temperature and average exchange interaction decrease. At sufficiently low concentrations the system is, in fact, no longer capable of supporting long-range magnetic order but rather undergoes a spin freezing phenomenon.^{3,4} We have been employing neutron scattering techniques to study the microscopic energetics of these random percolative systems.

The characteristic feature of a uniform ferromagnetic is a collective excitation whose energy E varies as the square of the momentum Q , $E = DQ^2$. Here D is a temperature dependent constant of proportionality which is maximum at $T = 0$ and monotonically falls to zero at $T = T_c$, the Curie temperature. Our measurements on a sample with $x = 0.4$ agree with this general behavior in that well defined spin waves which obey a quadratic dispersion relation are observed, and they renormalize toward zero energy as the Curie temperature ($T_c = 380$ K) is approached. Below ~ 80 K, however, D begins to decrease with decreasing temperature as the spin glass state is approached. Associated with this decrease in D is

an increase in the spin wave linewidths. Qualitatively similar behavior is found for the lower (nominal) concentration of $x = 0.2$, which has a Curie temperature of 118 K.

-
1. J. W. Lynn, G. Shirane, R. J. Birgeneau, and H. S. Chen, *AIP Conference Proceedings* 34, 313 (1976).
 2. R. J. Birgeneau, J. A. Tarvin, G. Shirane, E. M. Gyorgy, R. C. Sherwood, H. S. Chen, and C. L. Chien, *Physical Review* B18, 2192 (1978).
 3. S. M. Bhagat, M. L. Spano, H. S. Chen, and K. V. Rao, *Solid State Comm.* 33, 303 (1980).
 4. S. M. Bhagat, J. A. Geohegen, and H. S. Chen, *Solid State Comm.* (to be published).

NEUTRON SCATTERING STUDIES OF THE MAGNETIC SUPERCONDUCTOR $(\text{Ce}_{0.65} \text{Tb}_{0.35})\text{Ru}_2$

J. Fernandez-Baca and J. W. Lynn
(University of Maryland, College Park, MD)

and

(National Bureau of Standards, Washington, DC)

Neutron scattering measurements have been carried out on a polycrystalline specimen of $(\text{Ce}_{0.65} \text{Tb}_{0.35})\text{Ru}_2$ in order to study the crystal field splittings as well as the development of magnetic correlations at low temperatures.

At small wavevectors the intensity increases with the decreasing temperature indicating the development of ferromagnetic correlations. The intensity saturates at $T \sim 4$ K with no peak in its' temperature dependence. There is also no temperature dependence of the intensity of the {111} Bragg peak, so that there is no long range ferromagnetic order at this concentration. These observations agree with the results of Roth¹ and collaborators on the Tb system.

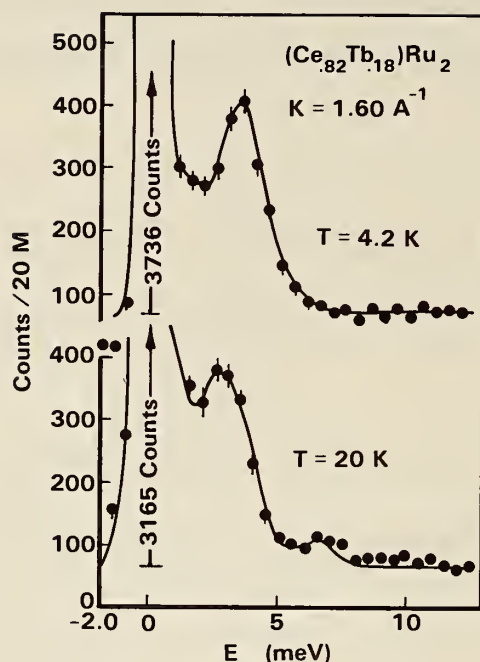


Figure 1. Inelastic scattering data from $(\text{Ce}_{0.65}\text{Tb}_{0.35})\text{Ru}_2$ at $T = 4.2\text{ K}$ and $T = 20\text{ K}$. At 4.2 K there is magnetic scattering which peaks at $\sim 3.3\text{ meV}$. At 20 K another transition appears at $\sim 6.6\text{ meV}$.

The system $\text{Ce}_{1-x}\text{Tb}_x\text{Ru}_2$ is a substitutional alloy in which the Tb^{3+} ions replace Ce randomly. The site symmetry is cubic² ($\bar{4}3m$) and has 12 Ru nearest neighbors and four Ce (or Tb^{3+}) next nearest neighbors. When situated in the crystal, the 13-fold degeneracy of the Tb^{3+} free ion is lifted, at least partially, by the effect of the electrical interaction of the neighboring ions. This splitting is very important for understanding the magnetic properties of the system since it determines the ground state of the ion. The simplest theoretical approach is given by the "crystal field model"³ in which the interaction is represented by an equivalent electrostatic field of the same symmetry. The most significant interaction on the Tb^{3+} sites is due to the 12 Ru nearest neighbors, so we may use, as a first approximation, cubic symmetry. This procedure has been found to give good results in the related system $(\text{Ce}_{1-x}\text{Ho}_x)\text{Ru}_2$.⁴

Inelastic scattering measurements (see figure 1) reveal the existence of an excitation at ~ 3.3 meV with additional scattering between 0.0 and 3.3 meV, at 4 K. At $T = 20$ K additional scattering appears at ~ 6.6 meV while the 3.3 meV peak appears to shift to lower energy. This scattering has been identified as magnetic since the intensity as a function of \vec{K} follows qualitatively the magnetic form factor $f(\vec{K})$ dependence. In comparison with the $(\text{Ce-Ho})\text{Ru}_2$ system, we note that the exchange interaction is significantly larger for Tb as evidenced by the higher spin freezing temperature (4 K for 35% Tb as compared to 2.0 K for 38% Ho) and by the observed width to the scattering which is presumably due to exchange broadening. Further measurements are in progress.

-
1. S. Roth, *Appl. Phys.* 15, 1 (1978), and references therein.
 2. W. B. Pearson, *Handbook of Lattice Spacings and Structures of Metals and Alloys*, Vol. 2, p. 67, Pergamon Press (1967).
 3. See, for example, M. T. Hutchings, *Sol. St. Phys.* 16, 227 (1964).
 4. J. W. Lynn, D. E. Moncton, L. Passell, and W. Thomlinson, *Phys. Rev. B* 21, 70 (1980); J. W. Lynn and C. J. Glinka, *J. Mag. and Magnetic Materials* 14, 179 (1979).

FERROMAGNETIC PHASE TRANSITION IN THE REENTRANT SUPERCONDUCTOR $(\text{Er}_{.11} \text{Ho}_{.89})\text{Rh}_4\text{B}_4$

J. W. Lynn

(University of Maryland, College Park, MD)

and

(National Bureau of Standards, Washington, DC)

and

R. N. Shelton

(Iowa State University, Ames, IA)

Pure ErRh_4B_4 becomes superconducting at $T_{c1} = 8.6$ K, then reenters the normal conducting phase at $T_{c2} = 0.9$ K¹ as it becomes ferromagnetic.² The substitution of Ho for Er increases the magnetic transition temperature, along with the reentrant superconductive transition T_{c2} while gently suppressing the upper superconducting transition. These three phase boundaries meet³ in a multicritical point at a concentration of 0.89 Ho and a temperature of ~ 6 K. We have prepared a sample slightly rich in Er such that the sample is superconducting over a small temperature interval; the multicritical point may then be reached by the application of hydrostatic pressure.⁴ Figure 1 shows the development of ferromagnetism at $T_m = 5.55$ K, as measured in the $\{101\}$ Bragg peak at ambient pressure. Susceptibility measurements on the same sample yield $T_{c1} = 5.7$ K, $T_{c2} = 5.4$ K, so that there appears to be a small temperature interval in which the ferromagnetism and superconductivity coexist. At low temperatures we obtain a magnetic moment $\mu_z = 7.78 \pm 0.3 \mu_B$, with the moment directed along tetragonal c axis. The reduced moment compared to the free ion value suggests that crystal field effects are important, and indeed crystal field transitions have been directly observed in inelastic neutron scattering spectra.

The nature of the magnetic transition is of some interest; the transition appears continuous and reversible. We also have noted that the intensity appears to be linear in $T - T_c$, which since

$$I \propto \left| \frac{T - T_M}{T_M} \right|^{2\beta} \quad (1)$$

would imply that $\beta = 1/2$, the mean field value. Mean field behavior has already been noted in specific heat data.³ In addition small angle scattering measurements reveal the absence of any critical scattering, although the paramagnetic scattering is easily observed. We thus conclude that the transition is indeed mean-field like. This behavior is most probably due to the proximity to the multicritical point, where the magnetization by itself is not the primary order parameter. The pressure dependent work is underway.

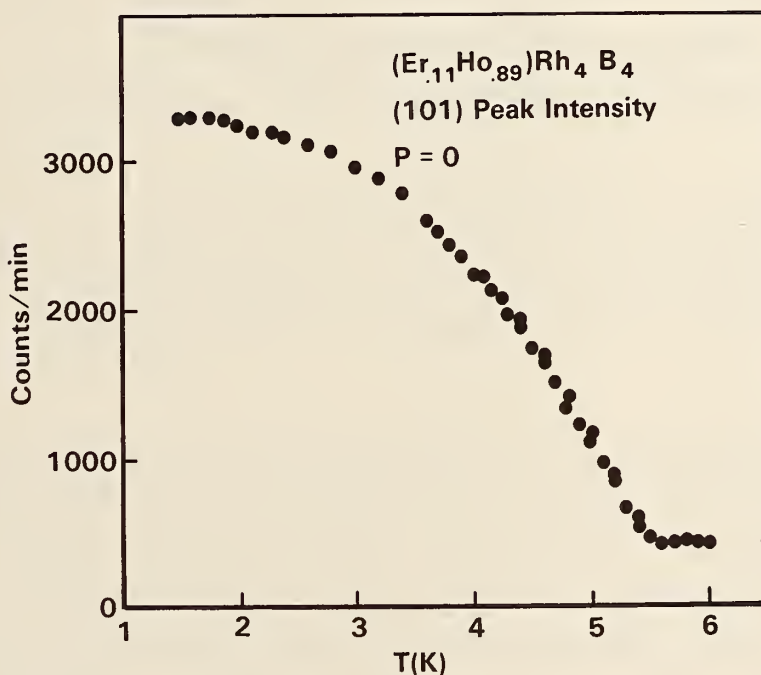


Figure 1. Intensity of the (101) Bragg peak as a function of temperature.

1. W. A. Fertig, D. C. Johnston, L. E. deLong, R. W. McCallum, M. B. Maple and B. T. Matthias, *Phys. Rev. Lett.* 38, 987 (1977).
2. D. E. Moncton, D. B. McWhan, J. Eckert, G. Shirane and W. Thomlinson, *Phys. Rev. Lett.* 39, 1164 (1977).
3. H. B. Mackay, L. D. Woolf, M. B. Maple and D. C. Johnston, *Phys. Rev. Lett.* 42, 918 (1979). Errata; 43, 89 (1979).
4. R. W. Shelton, C. U. Segre and D. C. Johnston, *Sol. St. Comm.* 33, 843 (1980).

MAGNETIC PERCOLATION IN THE PSEUDOBINARY SUPERCONDUCTOR $(\text{Ce}_{1-x}\text{Ho}_x)\text{Ru}_2$

J. W. Lynn

(University of Maryland, College Park, MD)

and

(National Bureau of Standards, Washington, DC)

and

C. J. Glinka

In the superconducting system $(\text{Ce}_{1-x}\text{Ho}_x)\text{Ru}_2$ small concentrations of Ho have been found to enhance the superconducting state while concentrations in excess of 30% are needed to suppress superconductivity. Central to the question of the interplay between ferromagnetism and superconductivity is the role that magnetism plays in this observed suppression. Investigations by Wilhelm and Hillenbrand¹ indicated that the ferromagnetic phase boundary (as determined by susceptibility) intersected the superconducting boundary at a concentration of 0.27 and a temperature of 1.6 K. Earlier neutron² work for $x = 0.27$ showed that ferromagnetic correlations do indeed develop at low temperatures, but the range of the correlations ceased to increase above 80 Å at a temperature of 0.5 K, and that no transition to long range order occurred.

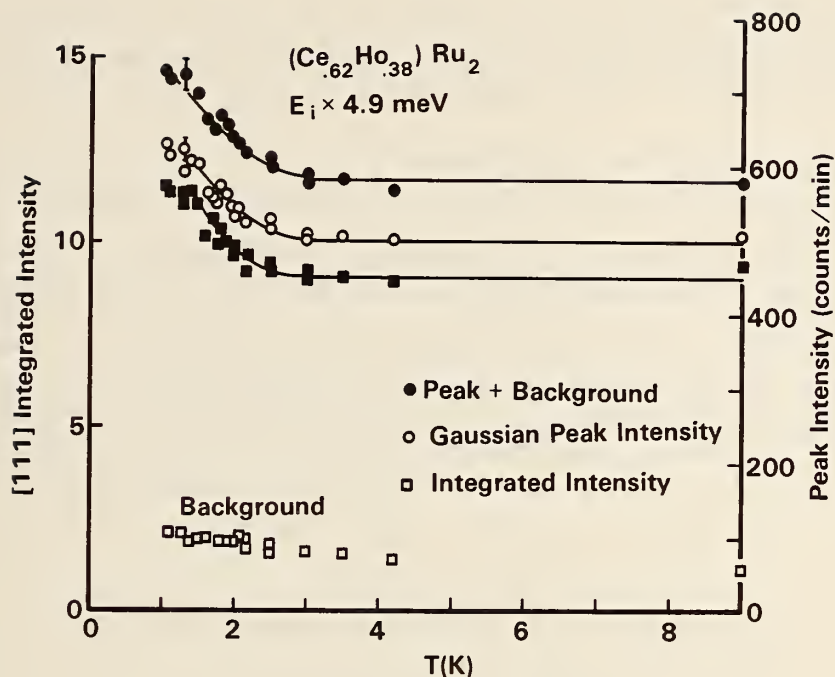


Figure 1. $\{111\}$ Bragg peak scattering as a function of temperature. The additional intensity below 2 K is the magnetic contribution to the scattering, which is limited in width by the instrumental resolution and signifies long range ferromagnetic order.

One possibility for the truncation of this transition is that the system is simply too dilute to support the ferromagnetic state. In this C-15 Laves phase the rare-earth ions occupy a diamond lattice, with a rather low coordination number of $z = 4$. If the coupling is dominated by nearest-neighbors then the percolation threshold³ P_c is 0.425, a concentration well above the magnetic-superconducting "coexistence" region. We might then interpret the suppression of the superconductivity at high concentrations as due to the increase of the average size of magnetic islands as the concentration increases, with the value of the ferromagnetic correlation range being bounded by this cluster size.

The actual exchange interaction may extend beyond nearest neighbors, which will reduce the percolation threshold, but the range may not be sufficient to produce long range order in the observed coexistence region.

To investigate this possibility we have carried out measurements on a sample with 38% Ho, which lies outside the superconducting region for all temperatures. The small angle scattering measurements still showed no characteristic peaks in the intensity as a function of temperature as might be expected for a ferromagnetic phase transition. Rather the scattering for $Q \gtrsim 0.05 \text{ \AA}^{-1}$ flattened off at $T \sim 2 \text{ K}$ in a fashion similar to the 27% alloy at 0.5 K. The scattering at smaller wave-vectors, however, continued to increase slowly with decreasing temperature. Thus in these data there is no indication of a ferromagnetic phase transition. Nevertheless figure 1 shows that below 2 K the intensity of the {111} Bragg peak increases, demonstrating that there is a spontaneous magnetization developing at low temperatures.

To interpret these data we note that for $p > p_c$ the system consists of finite clusters, which freeze at low temperatures, as well as an infinite cluster which will order at some temperature T_c . (If $p < p_c$ there are only finite clusters and hence there can be no long range order.) The observed scattering will be the sum of these two contributions,⁴ which may not exhibit a peak in the small-angle scattering as a function of temperature particularly if a substantial portion of the magnetic atoms belong to finite clusters. The strength of the magnetic Bragg scattering indeed shows that less than half the atoms belong to the infinite cluster. Calculations of the pair connectivity function are underway in order to make a detailed comparison between theory and experiment.

1. M. Wilhelm and B. Hillenbrand, *Z. Naturforsch. Teil A26*, 141 (1971); *J. Phys. Chem. Solids* 31, 559 (1970).
2. J. W. Lynn, D. E. Moncton, L. Passell and W. Thomlinson, *Phys. Rev. B21*, 70 (1980).
3. J. W. Essam, "Phase Transitions and Critical Phenomena," Vol. II, p. 197, ed. by C. Domb and M. S. Green (1972).
4. Below T_C (~ 2 K) there is also a contribution from domain wall scattering at the smallest wavevectors. The strength of this scattering is proportional to the order parameter and has been observed in other low temperature ferromagnets such as HoMo_6S_8 and $(\text{Er}_{1-x}\text{Ho}_x)\text{Rh}_4\text{B}_4$.

NEUTRON-SCATTERING STUDY OF SPIN WAVES IN THE

ANTIFERROMAGNET RbMnCl_3

H. A. Alperin

(Naval Surface Weapons Center, White Oak, MD)

and

(National Bureau of Standards, Washington, DC)

and

M. Melamud*

(NSWC and American University, Washington, DC)

RbMnF_3 is a transparent antiferromagnet with $T_N = 94\text{K}$. The structure is of the hexagonal BaTiO_3 -type belonging to the space group $P6_3/\text{mmc}$ with 6 formula units per unit cell; the six magnetic Mn ions occupy the 2a and 4f sites. Below T_N the magnetic structure consists of ferromagnetic planes stacked in the sequence $A(+)$, $B_1(-)$, $B_1(+)$, $A(-)$, $B_2(+)$, $B_2(-)$ along the c-axis. The spin direction is perpendicular to the c-axis. There are two kinds of sites in the Mn^{2+} ions; the A-sites (containing "lone spins") and the B-sites (containing much closer spin

*Permanent address: Nuclear Research Center-Negev, Beer Sheva, Israel.

pairs). The principal magnetic exchange interactions can therefore be described by J_{AB} and J_{BB} .

This study (at low temperature) of the spin wave spectrum of RbMnCl_3 was undertaken with the objective of answering the following question:

RbMnCl_3

4K

$$\text{--- Calculated} \left\{ \begin{array}{l} S_A = 2.4 \\ S_B = 2.5 \\ J_{BB} / J_{AB} = 1.65 \\ J_{AB} = 0.441 \end{array} \right\} \left\{ \begin{array}{l} 1.92 \\ 2.0 \\ 1.65 \\ 0.55 \end{array} \right.$$

○ □ Experimental

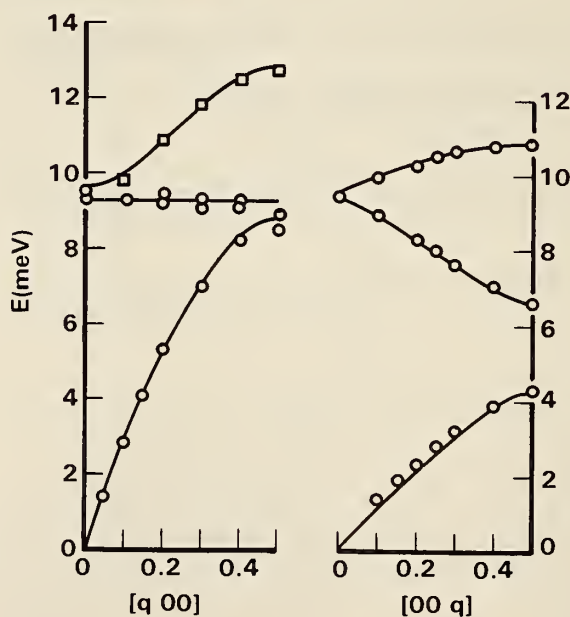


Figure 1. Spin wave dispersion spectrum of RbMnCl_3 . The solid curves are calculated according to the Heisenberg theory.

Are the magnetic interactions to be represented by the conventional Heisenberg model where J_{AB} and J_{BB} are of the same order of magnitude (probably acting via the intervening Cl ions -180° and 90° superexchange, respectively) or might RbMnCl_3 be representative of a new class of

magnetic materials; one in which the system is dominated by very strongly coupled spinpairs, which are in-turn, weakly coupled together, i.e. with $J_{BB} \gg J_{AB}$?

A large cylindrical single crystal ($\sim 2.5 \text{ cm}^3$ in volume) was used to collect data at liquid helium temperature on a triple axis spectrometer employing the constant-Q method, at a fixed scattering (final) energy of 14.7 meV. Measurements were performed with the scattering vector along three principal directions; [001], [110], and [100].

Samuelsen and Melamud¹ have derived expressions for the dispersion relations for both the conventional (Heisenberg) and the strong coupling models. For $J_{BB}/J_{AB} \gg 1$, although the (doubly degenerate) acoustic modes for the two models are similar, the (doubly degenerate) optic mode along the c-axis is split in the conventional case while it is not for the strong coupling model.

The experimental results immediately rule out the strong coupling model since two distinct optic branches were observed in the [00q] direction (and in other directions as well). Figure 1 shows the experimental results for the [q00] and [00q] directions and the curves calculated according to the Heisenberg theory. The fit is seen to be quite good. In performing the calculations, the spin moments on the A and B manganese atoms were allowed to vary. The two sets of parameters shown on the figure gave equally good fits to the data although the values for $S \approx 5/2$ are to be preferred. However, the ratio $J_{BB}/J_{AB} = 1.64 (\pm .1)$ is independent of the value of the moments and shows very clearly that in spite of the rather large difference between r_{AB} ($\sim 5\text{\AA}$) and r_{BB} ($\sim 3\text{\AA}$) the ratio J_{BB}/J_{AB} is not very large, indicating that superexchange rather than direct exchange is operative. The values of J_{AB} and J_{BB} found here are comparable to those found in other similar manganese halides.

1. E. J. Samuelsen and M. Melamud, *J. Phys. C: Solid State Physics*, 7, 4314 (1974).

STRUCTURAL INVESTIGATION OF $\text{Th}_6\text{Mn}_{23}\text{D}_{16}$

K. Hardman and J. J. Rhyne

and

K. Smith and W. E. Wallace

(University of Pittsburgh, Pittsburgh, PA)

The magnetic behavior of the isostructural compounds, Y_6Mn_{23} and $\text{Th}_6\text{Mn}_{23}$, are drastically altered upon hydrogenation. Y_6Mn_{23} is a ferromagnetic compound with $T_c = 486$ K and a bulk magnetization value of $13\mu_B/\text{f.u.}$ ¹ Upon hydrogen absorption the long range magnetic order vanishes. In contrast, $\text{Th}_6\text{Mn}_{23}$ is a Pauli paramagnet, while $\text{Th}_6\text{Mn}_{23}\text{H}_{30}$ exhibits long range magnetic ordering with $T_c = 329$ K and a bulk magnetization value of $18.5\mu_B/\text{f.u.}$ $\text{Th}_6\text{Mn}_{23}$ is a face centered cubic, space group $\text{Fm}\bar{3}\text{m}$, with 116 atoms per unit cell and four formula units per unit cell. There exists one Th site and four Mn sites (b , d , f_1 , and f_2).

The deuterium absorption isotherm shows a large plateau from 17 to 24 deuterium atoms. The sample was prepared at pressures just short of the plateau to obtain a single phase compound. The maximum number of deuterium atoms that can be experimentally absorbed into the $\text{Th}_6\text{Mn}_{23}$ is around 30. Neutron diffraction spectra at 4 and 295 K were collected using the high resolution 5-detector powder unit. The data were analyzed using the NBS profile fitting program based on the Rietveld method. Profile fitting programs are especially useful in studying the R_6T_{23} compounds in that they actually account for peak overlap which occurs predominately at high scattering angles.

The neutron diffraction fitted profile results determined that there were approximately 16 atoms of deuterium present in the compound and these atoms filled the f tetrahedral site and $2/3$ of the trigonal i sites. The atomic positions are shown on a two-dimensional projection along the z axis of $1/4$ the unit cell in figure 1. Figure 2 shows the neutron diffraction pattern and profile fit from the first two of the five detectors (Bragg angle range 10 – 55°). The χ value (weighted R-profile/R-expected) for the full spectrum from 10° to 115° for $\text{Th}_6\text{Mn}_{23}$

at room temperature is 1.58. Ideal structural models have generally been found to refine to χ^2 's ≤ 2 . This profile fit of the calculated model (smooth line) with the data (points) can be seen in figure 2.

This study has shown that the deuterium atoms in $\text{Th}_6\text{Mn}_{23}\text{D}_{16}$ occupy only the tetrahedral f site and trigonal i site. In contrast, Commadore et. al.² have found in $\text{Y}_6\text{Mn}_{23}\text{D}_x$ that deuterium atoms preferentially occupy both the octahedral a site and tetrahedral f and j sites.

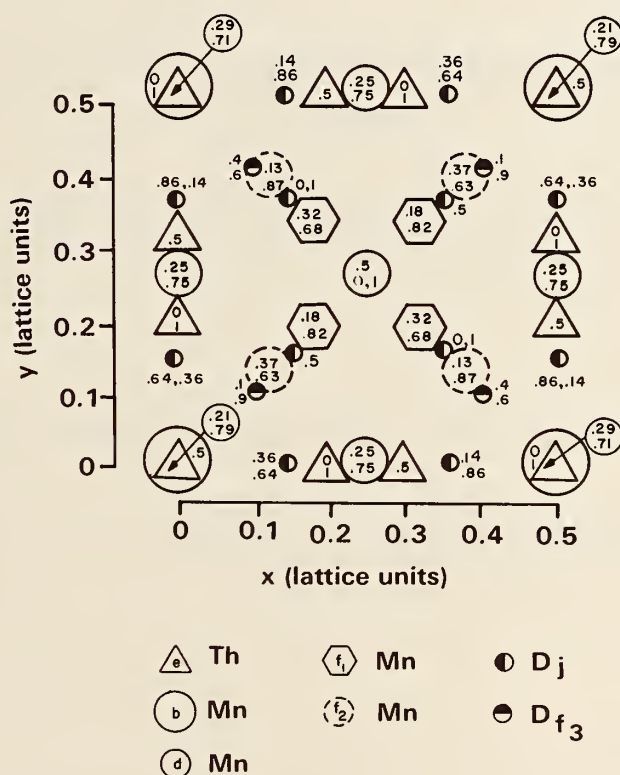


Figure 1. Two dimensional projection of atom positions along the $z[001]$ axis in $1/4$ of the unit cell of $\text{Th}_6\text{Mn}_{23}\text{D}_{16}$. The $z[001]$ coordinate is given for each site. The positions of all atoms are those obtained from the profile refinement fit.

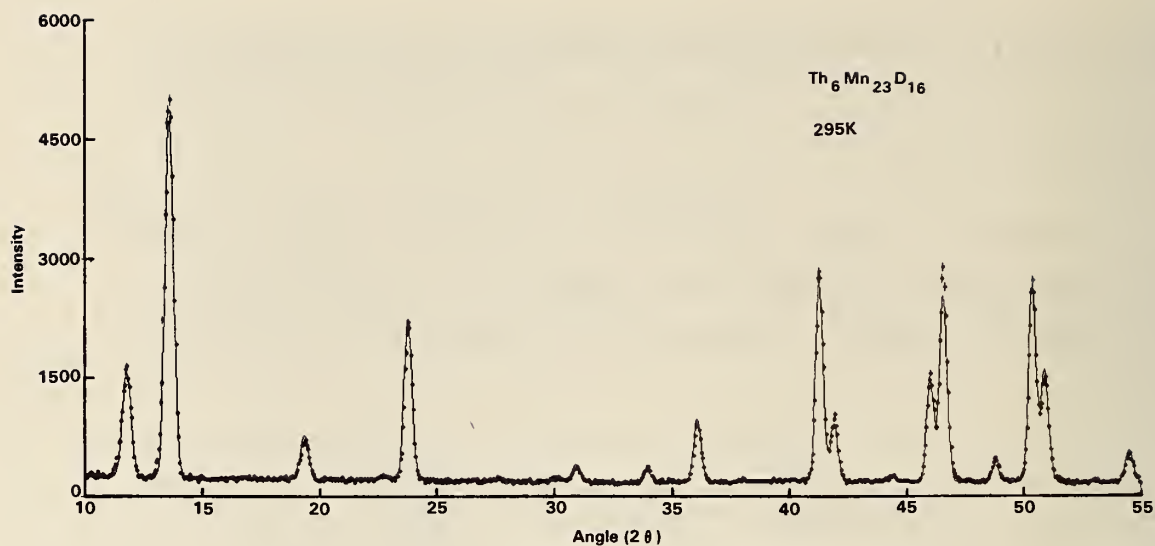


Figure 2. Experimental neutron scattering profile obtained from the first two detectors of the five detector NBS powder diffractometer. The solid line is the calculated model using the parameters in Table I.

-
1. S. K. Malik, T. Takeshita, and W. E. Wallace, *Solid State Comm.* 23, 599 (1977).
 2. M. Commandre, D. Fruchart, A. Rouault, D. Sauvage, C. B. Shoemaker, and D. P. Shoemaker, *J. de Physique* 40, L-639 (1979).

PREFERENTIAL ORDERING OF MN AND FE ATOMS IN $Y_6(Fe_{1-x}Mn_x)_{23}$

K. Hardman

and

W. J. James

(Department of Chemistry and Graduate Center for Materials
Research, University of Missouri-Rolla, MO)

The crystal structure of $Y_6(Fe_{1-x}Mn_x)_{23}$ compounds is face-centered cubic (Fm3m), isotypical with Th_6Mn_{23} .¹ There are four nonequivalent lattice sites occupied by Mn and/or Fe atoms, and one lattice site occupied by Y atoms. The intermediate compositions are particularly interesting in that the magnetizations and Curie temperatures are drastically reduced from those of the end members, Y_6Mn_{23} and Y_6Fe_{23} . In particular, there is no long-range magnetic ordering in the compositional region, $x = 0.5$ to 0.75 .¹ Although Fe-Mn interactions are expected to be antiferromagnetic and may compete with the ferromagnetic Fe-Fe, this does not account for the assumed paramagnetism of $Y_6(Fe_{1-x}Mn_x)_{23}$ system in the above compositional range. In many compounds, the long-range magnetic ordering of the Fe and Mn moments is dependent on the local chemical environment of these atoms. Previous studies (e.g. see reference 2) have assumed Mn and Fe atoms to be distributed stoichiometrically on each crystallographic site. However, atomic ordering in this system can strongly affect the local environment of the Mn and Fe and lead to significant changes in magnetic orders.

Neutron diffraction studies offer the most straight-forward approach in determining possible atomic ordering. The nuclear scattering data indicate very readily the degree of preferred ordering on nonequivalent crystallographic sites in that the nuclear scattering lengths of Mn and Fe differ in both sign and magnitude, $b_{Mn} = -0.37$ and $b_{Fe} = 0.95 \times 10^{-12}$ cm. The data were analyzed with the NBS version of the Rietveld profile method. In the refinement of the data, a constraint was imposed such that the sum of the Fe and Mn atoms would produce full occupancy at each transition metal site. This allowed a refined stoichiometry of the ternary to be determined.

Neutron diffraction data for several ternaries were collected to determine if preferential atomic ordering effects existed for the entire $Y_6(Fe_{1-x}Mn_x)_{23}$ system. The figure shows the degree of ordering as the % departure of Mn concentration from stoichiometry versus the overall Mn concentration. The most striking result is the preference of Fe atoms for the f_1 site and the preference of Mn atoms for the f_2 site. The Mn atoms exhibit a preference for the b site, especially if the f_2 site is occupied with a majority of Mn atoms. The d site appears to be stoichiometrically occupied in the Mn-rich ternary compounds but shows a preference for Fe atoms in the Fe-rich compounds. Since the b site contributes only 1 atom/f.u. and little ordering occurs on the d site, the atomic ordering of the ternary system is largely dependent on the two f sites. The greatest degree of atomic ordering occurs in the compositional range where the compounds are paramagnetic.

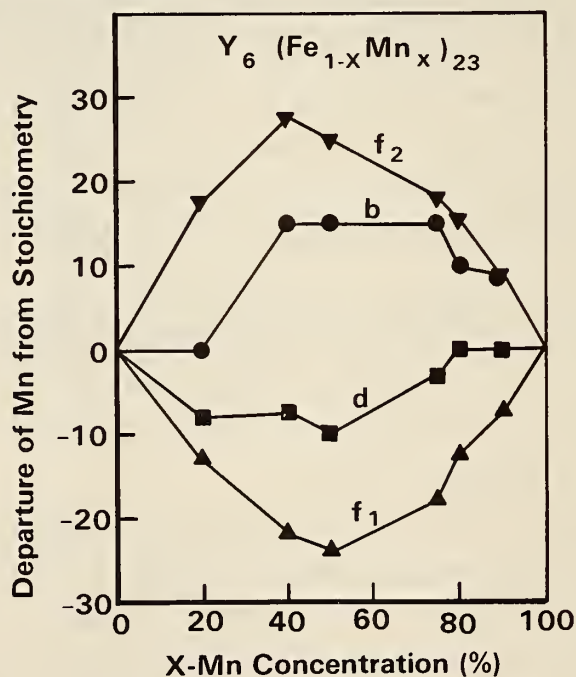


Figure 1. The % departure of Mn for stoichiometry vs. the overall Mn concentration. The positive % departure values represent Mn rich sites and the negative % departure values represent Fe rich sites.

1. H. R. Kirchmayr and W. Steiner, *J. Phys. Suppl.* 32, C1-665 (1971).
2. G. Hilscher and H. Rais, *J. Phys. F: Metal Phys.* 8, 511 (1978).

STUDIES OF ELECTRON DENSITY IN CARBONATE MINERALS

E. Prince

and

R. Peterson and G. V. Gibbs

(Virginia Polytechnic Institute and State University, Blacksburg, VA)

As part of studies of electron density distribution in carbonate minerals, neutron diffraction data sets have been collected from single crystals of two forms of CaCO_3 , calcite and aragonite, and from a crystal of magnesite, which is isomorphous with calcite, but with magnesium substituted for calcium. Crystal data for these crystals are given in table 1. Data were collected from two different crystals of calcite. With the exception of 00 ℓ reflections all reflections were observed in at least two symmetry equivalent positions, and most reflections were observed three times. The internal R factors between equivalent reflections were 3.1% and 2.5% for the larger and smaller crystal, respectively. Least squares refinement of structure and thermal parameters showed the effects of extreme secondary extinction, with more than 20% of reflections having correction factors (F_c^1/F_c) less than 0.3. The extinction parameter is strongly correlated with thermal parameters, and the anisotropic temperature factor tensors were non-positive definite, an unsatisfactory situation. Similar results were obtained from the crystal of magnesite. It may be possible to refine these structures by omitting the most severely extinguished reflections, or to determine reliable structure parameters from powder data. Otherwise electron density studies in these crystals will be extremely difficult.

For aragonite, an orthorhombic crystal, data were collected from three octants of the reciprocal lattice, and, again excepting 00 ℓ reflections, all reflections were observed at least twice, and most were observed three times. The agreement factor for equivalent reflections was 1.6%. The structure refined to a weighted agreement index of $R_w = 3.9\%$, and there was no evidence of important correlations between extinction and thermal parameters. Table 2 is a summary

Table 1. Crystallographic data for carbonate minerals.

		Calcite	Aragonite	Magnesite
Composition		CaCO_3	CaCO_3	MgCO_3
Space group		$\bar{R}3C$	Pmcn	$\bar{R}3C$
Cell constants	a	4.989 Å	4.9598 Å	4.637 Å
	b	--	7.9641 Å	--
	c	17.07 Å	5.7379 Å	15.023 Å

Reflections ($\lambda = 1.273\text{\AA}$, $2\theta_{\text{max}} = 120^\circ$)

observed	102	314	87
unobserved	9	15	0

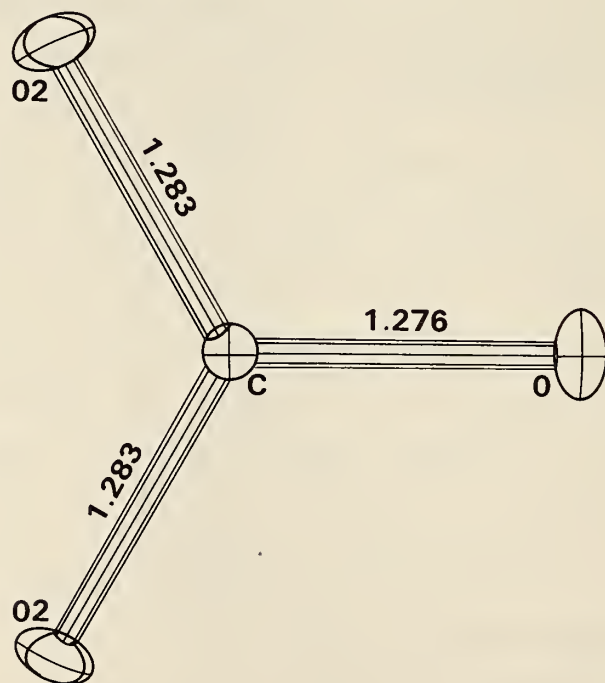


Figure 1. View of the carbonate group in aragonite, showing bond lengths and thermal ellipsoids.

of the structure parameters. As may be seen in figure 1, the shortest principal axes of the thermal ellipsoids of the two independent oxygen atoms are nearly parallel to the C-O bonds, as they should be.

Table 2. Refined structure parameters for aragonite. Thermal parameters are given as the coefficient of the expression $B = \beta_{11}h^2 + \beta_{22}k^2 + \beta_{33}l^2 + 2\beta_{12}hk + 2\beta_{13}hl + 2\beta_{23}kl$.

Parameter	x	y	z	β_{11}	β_{22}	β_{33}	β_{12}	β_{13}	β_{23}
Ca	.2500	.5849(1)	.2594(2)	.0047(5)	.0012(2)	.0030(4)	.0000	.0000	.0000(1)
C	.2500	.2381(1)	.4149(1)	.0032(4)	.0014(2)	.0019(3)	.0000	.0000	.0000(1)
O1	.2500	.0781(1)	.4045(2)	.0094(5)	.0010(2)	.0056(4)	.0000	.0000	.0004(1)
O2	.4733(1)	.3193(1)	.4127(1)	.0032(5)	.0026(2)	.0054(3)	-.0012(1)	-.0004(1)	-.0003(1)

NEUTRON POWDER DIFFRACTION STUDY OF THE STRUCTURE OF Li_2ReO_3

R. J. Cava
(Bell Laboratories, Murray Hill, NJ)

and

A. Santoro

and

R. S. Roth
Ceramics, Glass, and Solid State Science Division

In a confirming study of ionic conductors containing Li^+ , the structure of Li_2ReO_3 has been studied with the neutron powder technique.

Neutron diffraction measurements were made at room temperature with the five-counter high resolution neutron diffractometer at the NBSR, using the experimental conditions given in table 1.

The structure was refined with the Rietveld method (1969) modified by Prince (1979) to process simultaneously the five sets of data obtained from the five channels of the multiple detector diffractometer. The initial model of the structure was refined in space group $\bar{R}3c$ with six molecular units Li_2ReO_3 per unit cell and with the Re atoms located in positions 6(b), the Li atoms in positions 12(c), and the O atoms in positions 18(e)*. In this refinement (as well as in those that follow), the structural parameters were refined together with the lattice and profile parameters, and with ten additional parameters, two for each channel, defining linear backgrounds. Isotropic temperature factors for each atoms were kept fixed in these calculations, but an overall temperature factor was allowed to vary. The R factors obtained in this refinement are given in table 2. The value of R_1 is unreasonably high (18.97%). This fact, together with a resulting overall temperature factor $Q = -1.17 \text{ \AA}^2$ may indicate that the symmetry assigned to the structure is not correct. A refinement in space group $R3c$ was therefore carried out with the Re, Li1, and Li2 atoms in positions 6(a) and the O atoms in positions 18(b). The R factors obtained from these calculations (also reported in table 2) indicate that the structure is probably acentric, but

* Hexagonal axes have been used throughout these refinements.

Table 1. Experimental conditions used to collect the powder intensity data for Li_2ReO_3 .

Monochromatic beam: reflection 220 of a Cu monochromator

Wavelength: $1.5416(3) \text{ \AA}$

Horizontal divergences: (a) in-pile collimator: $10'$ arc;
 (b) monochromatic beam collimator: $20'$ arc;
 (c) diffracted beam collimator: $10'$ arc

Monochromator mosaic spread: $\sim 15'$ arc

Sample container: vanadium can ~ 10 mm in diameter

Angular ranges scanned by each detector: 15-40, 35-60, 55-80,
 75-100, 95-120

Angular step: 0.05°

Number of independent Bragg reflections: 65

still the value of R_I is too high (16.7%) and the value of Q too low (-1.14 \AA^2). At this point a close examination of some single peaks in the powder pattern showed that the peak shape can be described better with a modified Lorentzian than with a Gaussian (see Santoro and Prince, this report). The refinement program was therefore modified so that the Pearson type VII distribution could be used and calculations were carried out with $m = 2$ (modified Lorentzian)*. No improvement, however, was obtained with this method. This is an indication that other factors, such as the presence of impurities in the sample, affect the observed intensities. A final refinement was then carried out by excluding from the calculations a number of regions of the powder pattern, especially in correspondence of the tails on both sides of each identifiable peak. The R factors obtained

* For a description of the Pearson distribution see Santoro and Prince, this report.

Table 2. R-factors obtained in the refinements of the structure of Li_2ReO_3

Space Group		R_I	R_P	R_W	R_E	X
$\overline{R}3c$	No regions excluded	18.97	10.61	13.53	7.71	1.75
R3c	No regions excluded	16.70	10.05	12.77	7.71	1.66
R3c	Pearson function with m=2	16.71	10.01	12.71	7.71	1.65
R3c	Regions excluded	15.06	9.52	11.93	7.55	1.58

$$R_I = 100 \times \frac{\sum |I(\text{obs}) - I(\text{cal})|}{\sum I(\text{obs})}$$

$$R_P = 100 \times \frac{\sum |Y(\text{obs}) - Y(\text{cal})|}{\sum Y(\text{obs})}$$

$$R_W = 100 \times \left\{ \frac{\sum [W(Y(\text{obs}) - Y(\text{cal}))^2]^{1/2}}{\sum WY^2(\text{obs})} \right\}$$

$$R_E = 100 \times \left\{ \frac{(N - P + C)}{\sum WY^2(\text{obs})} \right\}^{1/2}$$

N, P, and C are the number of observations, the number of refined parameters, and the number of constraints, respectively.

in this last refinement are better than these calculated previously (Table 2), but the values of R_I and Q (15.06% and -1.12, respectively) are still unreasonable. The structural parameters obtained in this calculation are given in table 3.

A preliminary analysis of the structure shows that all parameters, with the exception of the overall temperature factor, have no unusual or suspicious features. We must conclude, therefore, that the structure determined in this study is basically correct. It may well be, however, that the symmetry is even lower than R3c and that structural distortions and/or impurities in the sample affect significantly the experimental intensities. The non-Gaussian peak shape of the diffraction lines is certainly an indication that the physical conditions of the sample do require an

analysis more detailed than the one made up to this point. As a knowledge of the accurate structure of the compound is important in the understanding of its electric properties, work in this direction is still being done at the present time.

Table 3. Results of the profile refinement of the structure of Li_2ReO_3

Atom	Position in R3c	x	y	z	B	n
Re	6(a)	0	0	0.0127(9)	0.4	1/3
O	18(b)	0.3572(12)	0.0134(12)	0.2484(9)	0.6	1.0
Li1	6(a)	0	0	0.2009(18)	1.0	0.29(3)
Li2	6(a)	0	0	0.8485(24)	1.0	0.29(2)

Numbers in parentheses are standard deviations on the last decimal figures.

-
1. H. M. Rietveld, *J. Appl. Cryst.*, 2, 65-71 (1969).
 2. E. Prince, *NBS Technical Note 117*, 8-9 (1979).

POWDER NEUTRON DIFFRACTION STUDY
OF CHEMICALLY PREPARED β -PbO₂Peter D'Antonio
(Naval Research Laboratory, Washington, DC)

and

A. Santoro

β -PbO₂ is the major constituent of the lead-acid battery. A detailed knowledge of its structure is essential in correlating electrochemical activity with the atomic arrangement of the electrode constituents of the battery. Such knowledge is also important in understanding the nature of the chemical bonds in compounds with rutile-type structures (Baur, 1956; 1958; 1961; Baur and Khan, 1971). Structural studies of β -PbO₂ have been carried out by x-ray (Tolkachev, 1958) and neutron powder diffraction techniques (Leciejewicz and Padlo, 1962, indicated by LP in what follows). The oxygen positions in the structure could not be determined with any precision in the x-ray work. On the other hand, in the neutron diffraction experiment only data up to $\sin\theta/\lambda = 0.3$ were used, and the structure was only partially refined because no temperature factors were introduced in the calculations. More importantly, in this study the value of the positional parameter of the oxygen atoms was obtained with such a large standard deviation that it is impossible to establish if the PbO₆ octahedra are compressed or elongated along their axial direction (Baur and Kahn, 1971). As the distortions of octahedra in rutile-type AB₂ oxydes are of theoretical interest, we thought it worthwhile to refine the structure of β -PbO₂ with the Rietveld method (Rietveld, 1969).

The sample used to collect the neutron diffraction data was chemically prepared, Baker reagent grade, β -PbO₂, lot #4604. The measurements were made at room temperature with a five detector diffractometer at the National Bureau of Standards Reactor (Prince and Santoro, 1980), using the experimental conditions summarized in table 1.

The powder pattern of $\beta\text{-PbO}_2$ consists of isolated peaks as well as resolved and unresolved clusters. The distribution of the reflections is such that the angular interval scanned by each detector contains a sufficient number of points free from diffraction lines to permit a reliable evaluation of the background contribution to the observed intensities at all the 2θ diffraction angles. Some of the diffracted lines were slightly asymmetric near the gaussian tails. This may be caused by impurities in the sample or by crystallite size effects. In any event, the regions affected were excluded from all subsequent calculations.

The structure was refined with the Rietveld method (Rietveld, 1969) modified to simultaneously process the data from the five channels of the multiple detector diffractometer. The neutron scattering amplitudes were $b(\text{Pb}) = 0.94$ and $b(\text{O}) = 0.58 \times 10^{-12}$ cm. The initial values of the lattice parameters and of the positional parameter x of the oxygen atoms were those obtained by LP (1962) and the initial profile parameters U , V , and W were calculated theoretically (Caglioti, Paoletti, and Ricci, 1958). The anisotropic temperature factors of the Pb and O atoms were refined together with the other parameters. Their introduction in the calculations is justified because the data were measured to a sufficiently high $\sin\theta/\lambda$ and because the background intensity was reliably determined. The initial values of these parameters were set equal to those of comparable oxides (e.g. Baur and Khan, 1971). All parameters were allowed to vary simultaneously until the shifts were less than 0.3 times the standard deviation. The results of the refinement are given in table 2 and the observed and calculated profiles are shown in figure 1.

The lattice parameters obtained in the refinement agree closely with those measured by LP with a back reflection camera and with those determined by Naidu (as quoted by Baur and Khan, 1971). The small systematic deviations are probably due to the uncertainty with which the

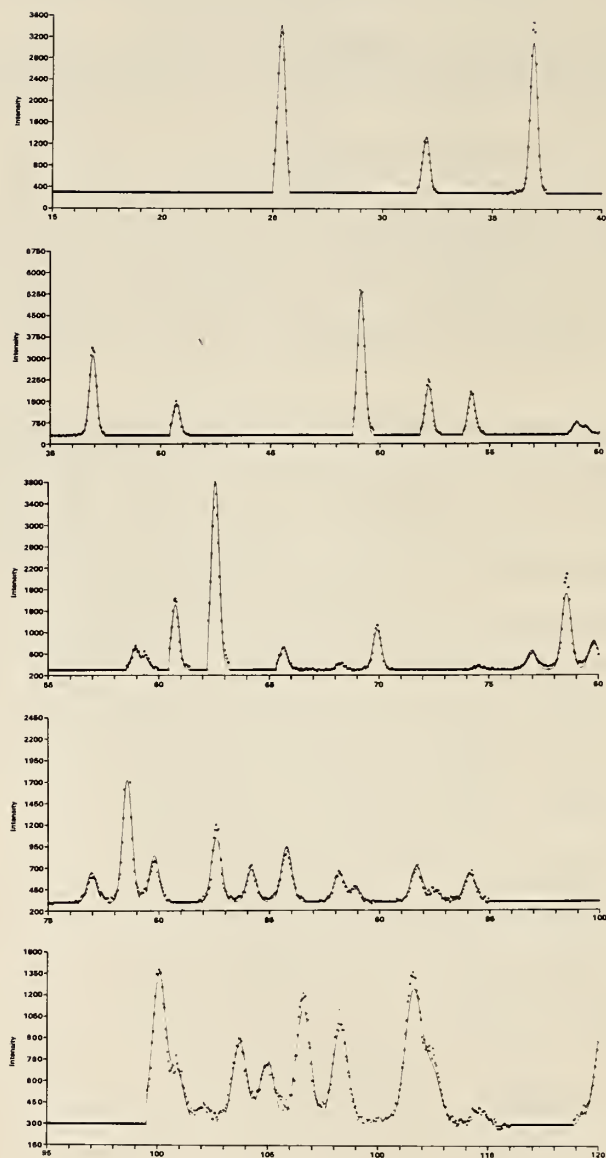


Figure 1. Observed (dots) and calculated (continuous line) profiles for β -PbO₂. Each section of the figure is recorded with a different detector of the five-detector diffractometer with an overlapping of the patterns of 5° in 2θ .

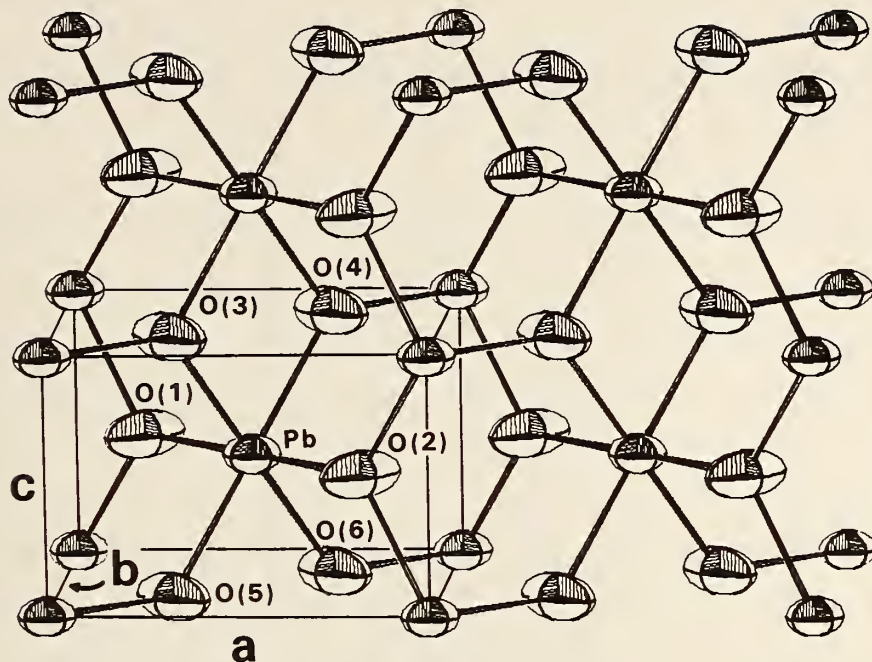


Figure 2. Three-dimensional view of the structure of $\beta\text{-PbO}_2$. The atoms are represented by their thermal ellipsoids. The labeling of the atoms is the same as that used in Table 3.

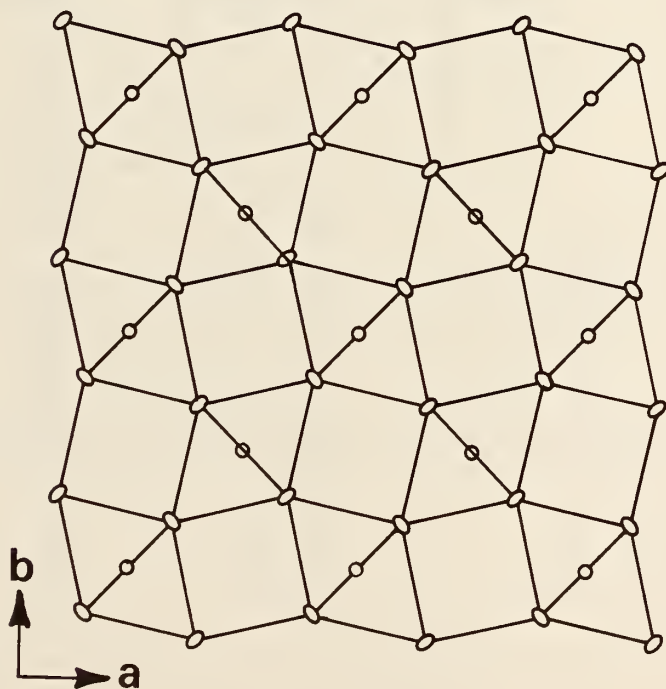


Figure 3. Projection of the structure of $\beta\text{-PbO}_2$ on the plane (001). Atoms are joined to show the packing of the PbO_6 octahedra.

Table 1. Experimental conditions used to measure the powder pattern of β - PbO_2 .

Monochromatic beam: reflection 220 of a Cu monochromator

Wavelength: $1.5416(3) \text{ \AA}$

Horizontal divergences:

(a) in pile collimator: $10'$ arc

(b) monochromatic beam collimator: $20'$ arc

(c) diffracted beam collimator: $10'$ arc

Monochromator mosaic spread: $\sim 15'$ arc

Sample container: vanadium can ~ 1 cm diameter

Angular ranges scanned by each detector: $15-40^\circ$, $35-60^\circ$, $55-80^\circ$, $75-100^\circ$, $95-120^\circ$

step: 0.05°

Number of independent Bragg reflections: 44

Table 2. Results of the refinement of the structure of β -PbO₂.

	a	c	c/a	x	x _m (***)
This work ⁽⁺⁺⁾	4.9578(2)	3.3878(2)	0.68333(5)	0.3067(2)	0.30835
Naidu ^(*)	4.9568(5)	3.3866(2)	0.68322(8)		
LP(1962)	4.955 (3)	3.383 (2)	0.6827 (7)	0.309 (4)	0.3083
Tolkacev (1958)	4.946	3.379	0.6832	0.308	0.3083

Atom	Position	$\beta_{11}=\beta_{22}$	β_{33}	β_{12}	$\beta_{13}=\beta_{23} \times 10^4$ ⁽⁺⁾
Pb	2a	55(4)	50(1)	3(6)	0
O	4f	97(5)	80(2)	-50(7)	0

Profile parameters: $U = 0.50(2)$, $V = -0.36(3)$, $W = 0.210(8)$ (deg^2)

$R = 4.71\%$, $R_p = 12.28\%$, $R_w = 14.44\%$, $R_{\text{expected}} = 6.05\%$, $\chi = 2.4$ ^(**)

(*) As quoted by Baur and Khan (1971)

(+) The thermal parameters are of the form

$$\exp[-(h^2\beta_{11} + k^2\beta_{22} + \ell^2\beta_{33} + 2hk\beta_{12} + 2h\ell\beta_{13} + 2k\ell\beta_{23})]$$

(**) The R-factors are defined in several publications (e.g., Rietveld, 1969).

(***) $x_m = \frac{c^2}{8a^2} + \frac{1}{4}$, with c and a measured by Naidu.

(++) The cell dimension errors obtained in the neutron refinement do not include the error in the neutron wavelength.

Table 3. Principal distances and angles in the octahedral coordination sphere of $\beta\text{-PbO}_2$.

	This work	LP (1962)
$\text{Pb-O}(3,4,5,6)^{(*)} \equiv (\text{Pb-O})_1$	$2.1689(7)^{(**)}$	$2.157(12) \text{ \AA}$
$\text{Pb-O}(1,2) \equiv (\text{Pb-O})_2$	$2.1500(11)$	$2.165(20)$
$\text{O}(3)\text{-O}(4)$	$2.7107(22)$	$2.677(40)$
$\text{O}(5)\text{-O}(6)$		
$\text{O}(1)\text{-O}(3,4,5,6)$	$3.0542(5)$	$3.056(8)$
$\text{O}(2)\text{-O}(3,4,5,6)$		
$\text{O}(3)\text{-O}(6)$	$3.38668(2)$	$3.383(2)$
$\text{O}(4)\text{-O}(5)$		
$\text{O}(3)\text{-Pb-O}(4)$	$77.35(5)^\circ$	$76.7(8)^\circ$
$\text{O}(5)\text{-Pb-O}(6)$		

(*) The labeling of the atoms is given in Figure 2.

(**) These distances were calculated by using $x=0.3067(2)$ and the lattice parameters measured by Naidu (Baur and Khan, 1971).
The distance $(\text{Pb-O})_m$ corresponding to x_m of Table II is 2.1615 \AA .

neutron wavelength is known (table 2) and therefore Naidu's parameters are used in all subsequent calculations. The values of the profile parameters U, V, and W are in agreement with those observed for other compounds analyzed with the same experimental conditions (e.g., Santoro, Roth, and Minor, 1979). The anisotropic thermal factors are of the same order of those reported for similar compounds (Baur and Khan, 1971). From figure 2 it can be seen that the major vibrational motion of the oxygen atoms is perpendicular to the planes $\{110\}$, in agreement with the results of Baur and Khan (1971) for rutile-type SiO_2 and for GeO_2 .

The structure of $\beta\text{-PbO}_2$ is shown in figure 2 with the atoms represented by their thermal ellipsoids. The six oxygen atoms surrounding the lead atoms form slightly distorted octahedra. In figure 3 the oxygen atoms are connected to show the packing sequence of the octahedra. The structure consists of vertical columns of edge sharing PbO_6 octahedra. These columns are oriented along the $[001]$ direction and form sequences of corner sharing octahedra along the $\langle 110 \rangle$ directions, with the octahedra alternately rotated by 90° about $[001]$.

The principal interatomic distances and angles in the PbO_6 octahedron are compared with the results of LP in table 3 (the values reported in column 3 of the table have been recalculated to facilitate comparison and to correct some errors in the results of LP). The four equatorial bonds $(\text{Pb}-\text{O})_1$ lie in the planes $\{110\}$ and the two axial bonds $(\text{Pb}-\text{O})_2$ are normal to these planes.

According to our results, and contrary to those of LP, $(\text{Pb}-\text{O})_1 > (\text{Pb}-\text{O})_2$, i.e., the octahedron of the oxygen atoms surrounding the lead atom is slightly compressed along the axial direction. This result, however, is significant only if the value of the standard deviation σ_x associated with the positional parameter x can be considered reliable. In a recent analysis of the profile fitting procedure, Sakata and Cooper (1978) have concluded that the Rietveld method weights the observations incorrectly and that the estimated standard deviations are smaller by a

factor of at least 2 than those given by a refinement based on integrated intensities. On the other hand, Prince (1980) has pointed out that the high precision of the Rietveld method is a consequence of the fact that each peak is assumed to be Gaussian, so that each data point within the peak becomes an independent measurement of the intensity. This results in a more precise estimate of the diffracted intensity. In agreement with Prince's conclusions, it has been shown in a number of cases (e.g. Andresen, Hewat, and Sabine, 1978; Cheetham and Taylor, 1977) that the Rietveld method gives quite realistic standard deviations associated with the atomic coordinates. The high precision of the Rietveld method translates into high accuracy only if the model is adequate, i.e., free of hidden factors such as unrecognized structural distortions, non-gaussian peak shape, etc. No problems of this kind are apparent in our experiment. All the parameters calculated in the refinement are quite reasonable, including the thermal and profile parameters which are very sensitive to errors in the adopted structural model and to the physical conditions of the sample used to collect the data. Finally, the correlation coefficients involving x and the other refined quantities are low, the largest of them being only 10%.

To remove any doubts, a second evaluation of the positional parameter was obtained by carrying out a refinement based on integrated intensities. These were obtained by fitting least-squares gaussians to 27 single or separable reflections. This refinement gave $x = 0.3066(6)$ with an R-factor, based on structure factors, of 2.0% (the R factor based on F^2 was 3.6%). As expected, the standard deviation σ_x is larger than that obtained with the Rietveld method (the same is true for the standard deviations associated with the thermal parameters). Even in this case, however, the difference between the value of x obtained in the refinement and that reported by LP can be considered significant. Thus, the point representing $\beta\text{-PbO}_2$ in the plot of x versus c/a shown in figure 2 of Baur and Khan's paper (1971) is located below the line

corresponding to the conditions for undistorted octahedra in the structure. It follows that $\beta\text{-PbO}_2$ is in the same category with the fluorides of Mg, Mn Fe, Co, and Zn and the oxides of Cr, Ru, and Os. A conclusion of this study is that $\beta\text{-PbO}_2$ is closer to the Born model, and its bonding has more ionic character, than previous structural investigations implied.

-
1. A. F. Andresen, A. W. Hewat, and T. M. Sabine, *Conference on Diffraction Profile Analysis*, Abstracts, Cracow, Poland (1978).
 2. W. H. Baur, *Acta Cryst.* 9, 515-520 (1956).
 3. W. H. Baur, *Acta Cryst.* 11, 488-490 (1958).
 4. W. H. Baur, *Acta Cryst.* 14, 209-213 (1961).
 5. W. H. Baur and A. A. Khan, *Acta Cryst.* B27, 2133-2139 (1971).
 6. W. R. Busing, K. O. Martin, and H. A. Levy, *ORFLS*, Report ORNL-TM-305, Oak Ridge National Laboratory, Oak Ridge, Tennessee (1963).
 7. G. Caglioti, A. Paoletti, and F. P. Ricci, *Nucl. Instrum.* 3, 223-228 (1958).
 8. A. K. Cheetham and J. C. Taylor, *J. Sol. State Chem.* 21, 253-275 (1977).
 9. J. Leciejewicz and I. Padlo, *Naturwissenschaften* 16, 373-374 (1962).
 10. E. Prince, *J. Appl. Cryst.*, submitted for publication (1980).
 11. E. Prince and A. Santoro, NBS Technical Note 1117, Editor F. J. Shorten, 11-12 (1980).
 12. H. M. Rietveld, *J. Appl. Cryst.* 2 65-71 (1969).
 13. M. Sakata and M. J. Cooper, Report HL78/2359 AERE Harwell, U.K. (1978).
 14. A. Santoro, R. S. Roth, and D. Minor *Acta Cryst.* B35, 1202-1205 (1979).
 15. J. C. Taylor and P. W. Wilson *Acta Cryst.* B30, 554-555 (1974).
 16. A. Tolkacev, *Vestnik Leningradskogo Univ.* No. 4, 152 (1958).

FURTHER WORK ON GEOMETRICAL AMBIGUITIES IN THE INDEXING OF POWDER PATTERNS

A. Santoro

and

A. D. Mighell

(Ceramics, Glass, and Solid State Science Division)

By definition, two or more different lattices give a "geometrical ambiguity" when they generate powder patterns having the identical number of distinct diffraction lines with identical values of $(\sin\theta)/\lambda$, but not necessarily with identical multiplicity. For example, it is easy to prove that a body centered cubic lattice of conventional unit cell vectors \vec{a}_i ($i = 1, 2, 3$) and the tetragonal P lattice obtained with the transformation

$$\vec{b}_i = \sum_j B_{ij} \vec{a}_j \quad (j = 1, 2, 3) \quad (1)$$

in which

$$B = \begin{pmatrix} 0 & -1/2 & 1/2 \\ 0 & -1/2 & -1/2 \\ 1/2 & 0 & 0 \end{pmatrix} \quad (2)$$

satisfy the above definition of geometrical ambiguity. It follows that the powder pattern consistent with one lattice can be indexed equally well in terms of the other (in this particular case, the lattices consistent with the same powder pattern are four, the other two being orthorhombic F and orthorhombic P).

Geometrical ambiguities have been studied by Mighell and Santoro (1975) with the following procedure.

Let us consider a reciprocal lattice Λ^* described by the translations \vec{a}_i^* . The reciprocal lattice vectors of Λ^* are given by

$$\vec{r}_h^* = \sum_i h_i \vec{a}_i^* \quad (3)$$

with

$$h_i = \dots -1, 0, 1, \dots \quad (4)$$

If we perform the transformation

$$\vec{b}_i^* = \sum_j B_{ij}^* \vec{a}_j^* \quad [B^* = (\hat{B})^{-1}] \quad (5)$$

we generate a new lattice Γ^* described by the translations (primitive) \vec{b}_i^* . The reciprocal lattice vectors of Γ^* are given by

$$\vec{r}_k^* = \sum_i k_i \vec{b}_i^* \quad (6)$$

with

$$k_i = \dots -1, 0, 1, \dots \quad (7)$$

The vectors \vec{r}_k^* can be expressed in terms of the base \vec{a}_i^* by making use of equation (5)

$$\vec{r}_k^* = \sum_j l_j \vec{a}_j^* \quad (8)$$

where

$$l_j = \sum_i k_i B_{ij}^* \quad (9)$$

The lattices Λ^* and Γ^* will give a geometrical ambiguity if, for each vector \vec{r}_h^* in Λ^* there is a vector \vec{r}_k^* in Γ^* such that

$$|\vec{r}_h^*| = |\vec{r}_k^*| \quad (10)$$

and vice-versa.

The method used by Mighell and Santoro (1975) to verify equation 10 consists in proving if two quadratic forms represent the same set of numbers. For the example represented by equations (1) and (2) we have

$$r_h^{*2} = (h_1^2 + h_2^2 + h_3^2) a^{*2} \quad (11)$$

where

$$h_1^2 + h_2^2 + h_3^2 = 2n \quad (\text{body centered lattice}), \text{ and}$$

$$r_k^{*2} = 2(2k_1^2 + k_2^2 + k_3^2) a^{*2} \quad (12)$$

It can be proven, with standard methods of number theory, that $h_1^2 + h_2^2 + h_3^2 = 2n$ and $2(2k_1^2 + k_2^2 + k_3^2)$ represent the same set of numbers when the triplets h_i and k_i are cycled over all the permissible integers. Therefore, the two lattices Λ^* and Γ^* do indeed give a geometrical ambiguity.

A significant disadvantage of this approach is that it cannot be generalized to the point where conditions for the occurrence of ambiguities can be established. In particular, the method does not allow one to understand in a direct way the critical role played by the symmetry in searching for such conditions, and consequently, it does not make it possible to devise a systematic procedure for finding all the geometrical ambiguities which may occur in frequently encountered lattices. Therefore, we have analyzed the problem with a new procedure, simpler and more general than the one used previously (Mighell and Santoro, 1975).

Let us consider the transformation

$$\vec{b}_i = \sum_j B_{ij} \vec{a}_j \quad (13)$$

and let χ and χ' be triplets of real numbers and h and h' triplets of integers. We have

$$\chi' = B h \quad (14)$$

and

$$\vec{a}_i^* = \sum_j B_{ji} \vec{b}_j^* \quad (15)$$

A reciprocal vector is expressed in Λ^* and Γ^* by the equations

$$\vec{r}^* = \sum_i h_i \vec{a}_i^* = \sum_i \sum_j h_j B_{ij} \vec{b}_i^* \quad (16)$$

Since the h_i are integers, \vec{r}^* is a reciprocal lattice vector in Λ^* . It will be a reciprocal lattice vector also in Γ^* if, and only if,

$$h'_i = \sum_j h_j B_{ij} \quad (17)$$

i.e., if the numbers $\sum_j h_j B_{ij}$ are also integers. If these numbers are not integers, then \vec{r}^* is a reciprocal lattice vector in Λ^* but not in Γ^* .

If we write the transformations

$$\text{and} \quad \left. \begin{aligned} \chi' &= B \chi \\ \chi &= B^{-1} \chi' \end{aligned} \right\} \quad (18)$$

we may say that a peak χ in the powder pattern of Λ will be coincident (i.e. having the identical value of $\sin\theta/\lambda$) with a peak in the powder pattern of Γ if the numbers χ' are integers. And, conversely, a peak χ' of Γ will be coincident with a peak of Λ if the numbers χ are integers.

This type of solutions will certainly exist if the elements B_{ij} of matrix B are rational numbers, i.e., if Λ and Γ are derivative lattices.¹ Three cases are possible: (1) some peaks of the pattern of lattice Λ are coincident with some peaks in the pattern of Γ and vice-versa; (2) all the peaks of Λ are coincident with peaks of Γ , but the converse is not true; (3) all the peaks of Λ are coincident with peaks of Γ and vice-versa. The necessary and sufficient conditions for

¹This is a sufficient, not a necessary condition. The necessary condition for the occurrence of coincidences is that at least a column of matrix $H B$ must be rational. Matrix H is unimodular with H_{ij} integers. Its use here is necessary to deal with cases such as $[(R + 2)(2) I/RR I/RR I]$ which can be readily transformed into $[R(2) I/RR I/RR I]$. In the above matrices R and I indicate a rational and an irrational number, respectively.

case (1) to occur have been found previously. Cases (2) and (3) can be understood by discussing a specific example. Consider the transformation matrix Λ to Γ

$$\mathfrak{P} = \begin{pmatrix} 1 & 0 & 0 \\ 0 & 1 & 0 \\ 0 & -1/3 & 1/3 \end{pmatrix} \quad (19)$$

Transformations (18) are:

$$\begin{aligned} x' &= h & x &= h' \\ y' &= k & y &= k' \\ z' &= (-k + \ell)/3 & z &= k' + 3\ell' \end{aligned} \quad (20)$$

The triplets \mathfrak{x} are always integers, that is, all the diffraction lines in the pattern of Γ are also present in the pattern of Λ . The converse, however, is not true. For example if $\mathfrak{h} = (101)$, then $\mathfrak{x}' = (10 \ 1/3)$. If, however, Λ is cubic primitive, each line of general indices in the pattern of Λ is the superposition of 48 reflections, the indices of each of them being obtained by permutation of place and sign of the three integers h , k , and ℓ . Under these conditions, it can be proven that, if a reflection \mathfrak{h} does not give integral solutions for \mathfrak{x}' , there is at least one reflection \mathfrak{h}_n , metrically equivalent to \mathfrak{h} , which does and, as a result, each line in the pattern of Λ will have a coinciding line in the pattern of Γ . Clearly, the multiplicity is different in the two cases. Returning to our example, the reflection $\mathfrak{h} = (101)$ does not give integral solutions for \mathfrak{x}' , but $\mathfrak{h}_n = (011)$, which is metrically equivalent to \mathfrak{h} in the cubic system, does, and therefore, the reflection 010 of Γ will occur exactly at the same $\sin\theta/\lambda$ of the reflections 101 and 011 of the cubic lattice Λ .

The case represented by matrix (19) was not recognized in the previous study of geometrical ambiguities (Mighell and Santoro, 1975). On the basis of this example we may state that:

"The necessary and sufficient condition that lattices Λ and Γ must satisfy to give a geometrical ambiguity is that every reciprocal lattice vector of one of the two lattices must be either a reciprocal lattice vector or be metrically equivalent to a reciprocal lattice vector of the other lattice."

What this means in practice is that the metric symmetry of the two lattices must be such that a group of equivalent reciprocal lattice vectors in a lattice has at least one representative which also belongs to the other lattice.

The previous discussion shows that symmetry plays a vital role in the occurrence of geometrical ambiguities. In fact, it can be shown that ambiguities exist only if one of the two lattices is cubic, hexagonal, rhombohedral, or tetragonal.²

A straightforward method to discover all the cases of geometrical ambiguities consists in generating all the unique β matrices with "simple" rational elements B_{ij} and in transforming with them the high symmetry lattices. Each transformation can then be analyzed very much in the same way used to analyze the example discussed previously. Programs for doing these calculations are now being developed, and the results will be given in the next report.

²This statement requires a clarification. Geometrical ambiguities also occur for lattices of low symmetry. This can be seen in Table 1 of the paper by Mighell and Santoro (1975) (for example, the orthorhombic lattices F and P of case (2)). In these instances, however, the ratios of the scalar products $\vec{a}_i \cdot \vec{a}_j$ (and those of $\vec{b}_i \cdot \vec{b}_j$) are rational numbers, i.e., these lattices have derivative lattices of higher symmetry. It can be proven that the treatment of cubic, hexagonal, rhombohedral, and tetragonal lattices also includes these cases.

1. A. D. Mighell and A. Santoro, *J. Appl. Cryst.* 8, 372-374 (1975).

SMALL-ANGLE NEUTRON SCATTERING STUDY OF A
TWO-PHASE TUNGSTEN ALLOY

H. J. Prask and C. S. Choi
(Energetic Materials Division, LCWSL, ARRADCOM, Dover, NJ)

and

(National Bureau of Standards, Washington, DC)

and

S. Singhal
(National Bureau of Standards, Washington, DC)

and

(State University of New York at Stony Brook, NY)

One of the principal types of anti-tank munitions employed by the Army incorporates a tungsten-alloy "kinetic-energy" penetrator. The penetrators which are prepared by means of isostatic pressing, sintering, heat treatment and cold working--are comprised of a "tungsten" phase and a "matrix" phase. Improvement in the performance of these munitions is sought by varying the composition, heat treatment, or degree of cold work. A previous neutron diffraction study showed the variations in texture of the matrix phase as a function of degree of cold work in .97W-.018Ni-.012Fe by weight alloy.¹ In this composition alloy, the matrix phase is virtually invisible to x-ray diffraction.

Another aspect of interest for these samples is the hardening which is observed when a second heat treatment is given the alloy after swaging. For a nominal .90W-.07Ni-.03Fe alloy ("tungsten" phase: ~ .998W-0.0005Ni-0.0015Fe; matrix phase: ~ .22W-.55Ni-.23Fe by weight) yield strength and hardness are each found to increase by approximately 20% after heat treatment. Preliminary SANS measurements have been made on three .90/.07/.03 samples. All three samples were sintered and heat treated (20 hrs. at 1000°C); two of the samples were swaged (24% R.A.) and one of these was further heat treated (5 hrs at 500°C).

In the SANS configuration employed the useable momentum-transfer range was $Q \geq 0.01 \text{ \AA}^{-1}$. For all three samples the data were found to

correspond very well to Porod distributions (i.e. $I(Q) = k/Q^4$). A Porod distribution is expected for scatterers with well-defined boundaries and radii of gyration fulfilling the condition $R_g Q > 1$. This indicates that $R_g > 110\text{\AA}$ for the scatterers in all three samples. In addition it was found that the scattered intensity, which is proportional to the product of (number of scatterers X surface area per scatterer) is in the ratio $1/1.79 \pm 0.02 / 1.95 \pm 0.02$ for the unswaged, swaged, and swaged with second heat treatment samples, respectively.

Further SANS and wide-angle neutron diffraction measurements are planned to better understand the differences observed in the results for the three samples. Specifically, quantitative results characterizing the nature of the scatterers (i.e. precipitate or void) and size and concentration are needed to understand the hardening process.

-
1. C. S. Choi and H. J. Prask, *NBS Tech. Note* 1117, 139-42 (1980).

SMALL-ANGLE NEUTRON SCATTERING STUDY OF THE MICROSTRUCTURAL
DEVELOPMENT DURING PRECIPITATION STRENGTHENING OF NI BASED SUPERALLOYS

S. P. Singhal
(State University of New York, Stony Brook, NY)

and

(National Bureau of Standards, Washington, DC)

and

H. A. Alperin
(Naval Surface Weapons Center, White Oak, MD)

and

(National Bureau of Standards, Washington, DC)

and

H. Herman
(State University of New York, Stony Brook, NY)

and

F. Biancanello

In present day aerospace technology, the Ni based superalloys form the basis of aircraft engine turbine blade materials, which are used under most aggressive conditions of the temperature, stress, and chemical environment. In order to achieve microstructures which can retain a respectable stability of properties, the superalloys not only contain several alloying additions, but also undergo a complex series of thermal treatments. A considerable degree of "commercial" success has been achieved in production and usage of these alloys; although the "precise" mechanism of formation, growth, and degradation of microstructural properties remains relatively understood.

At the NBS reactor we have begun a program to study the kinetics of precipitation strengthening and subsequent microstructural changes during the creep and high temperature fatigue deformation of these alloys.* In Ni based superalloys, the major strengthening constituent

*Some recent studies have indicated that creep deformation in these alloys is synchronous with the coarsening of γ' . Therefore, creep behavior of these alloys is highly dependent on the stability of γ' under ambient temperature and stress conditions.

is gamma prime (γ'). The "precise" composition of γ' varies during the different stages of heat treatment but in general it can be given as $\text{Ni}_{(4-x)} [\text{Al} + \text{M}]_x$ where M could be the elements like Ti, Ta, and Nb etc. A high volume fraction and fine dispersion of γ' are needed to enhance the properties for high temperature applications.

In the present study a binary alloy of Ni-14.7 at % Al was quenched from 1200°C from a single phase region. Quenched samples of the thickness ~ 0.1 cm were aged isothermally at the temperatures of 540 and 600°C. Figures 1(a) and 1(b) show the Small-Angle Neutron Scattering (SANS) curves for the alloy aged at 600°C. The measurements were performed using neutrons of wavelength $\sim 6\text{\AA}$ ($\text{FWHM} \pm 20\%$) to avoid the complicating effects of double Bragg scattering. The Q range ($= \frac{4\pi \sin\theta}{\lambda}$) of these experiments was between 0.009 and 0.09 \AA^{-1} . Depending upon the number density of the structural inhomogeneities, the structural features in the range of 600 to 60 \AA dimensions could be easily measured by the present choice of parameters.

The as-quenched samples showed a flat scattering profile (figure 1(a)) indicating that quenching was severe enough to suppress the formation of γ' . After one hour of aging at 600°C a well defined peak is developed in the small-angle scattering curve (figure 1(b)). With further aging, this peak moves towards the lower scattering vectors. Depending upon the type of model used to analyze the aging kinetics, such a peak shifting is interpreted as either coarsening of γ' particles formed during aging or coarsening of wavelength of modulated γ' structure formed by spinodal decomposition mechanism.

The mechanism of the formation of γ' in Ni-Al alloys has been a subject of some controversy in the recent past. Ardell and Nicholson¹ and Kirkwood^{2,3} have concluded on the basis of their electron-microscopic studies that γ' is formed by a nucleation and growth mechanism. However, Gentry and Fine⁴ carried out the measurement of saturation magnetization as a function of aging time and indicated that the decomposition takes place by a spinodal mechanism. It must be realized at this point that the aging temperatures used by various authors ranged from 400 to 800°C.

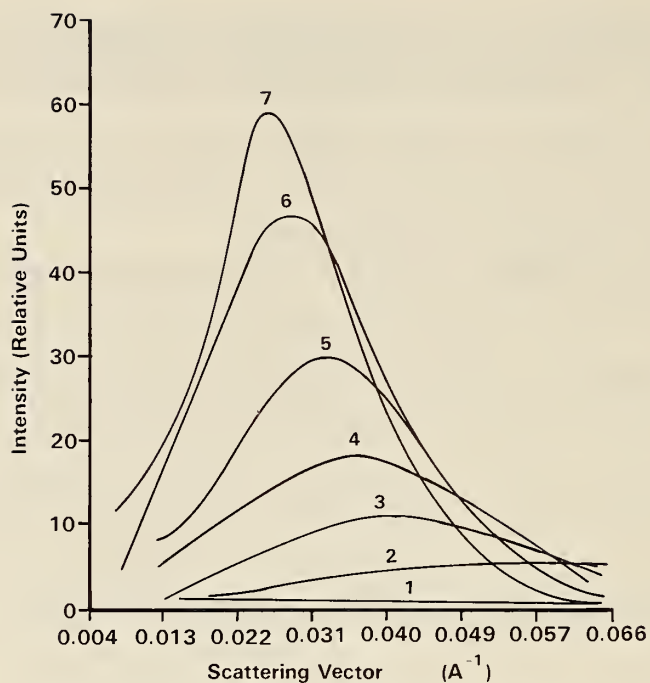


Figure 1(a). Intensity (I) vs. scattering vector (Q). Spectra for solid-quenched and aged Ni-14.7 atomic % Al alloy. [1-as-quenched, 2-1 hr., 3-3 hr., 4-5 hr., 5-10 hr., 6-15.5 hr., and 7-24 hr. at 600°C]

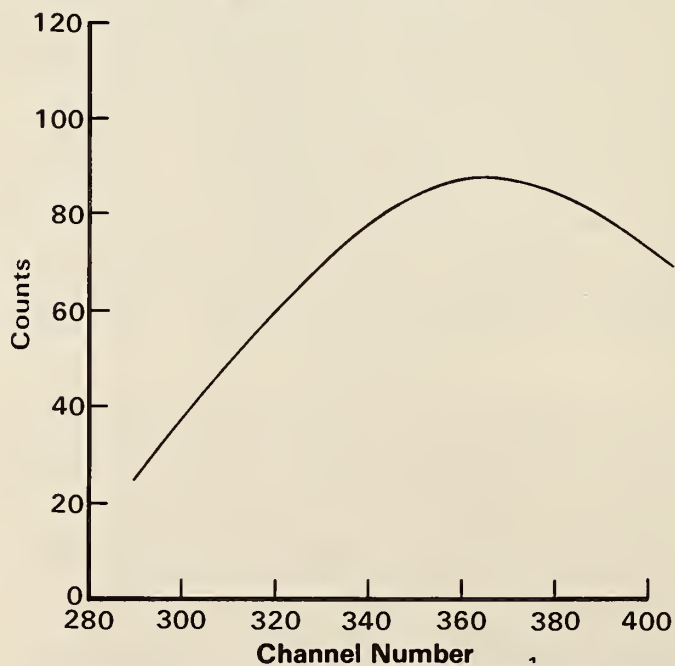


Figure 1(b). Intensity vs. scattering vector for Ni-14.7 atomic % alloy aged 1 hr. at 600°C.

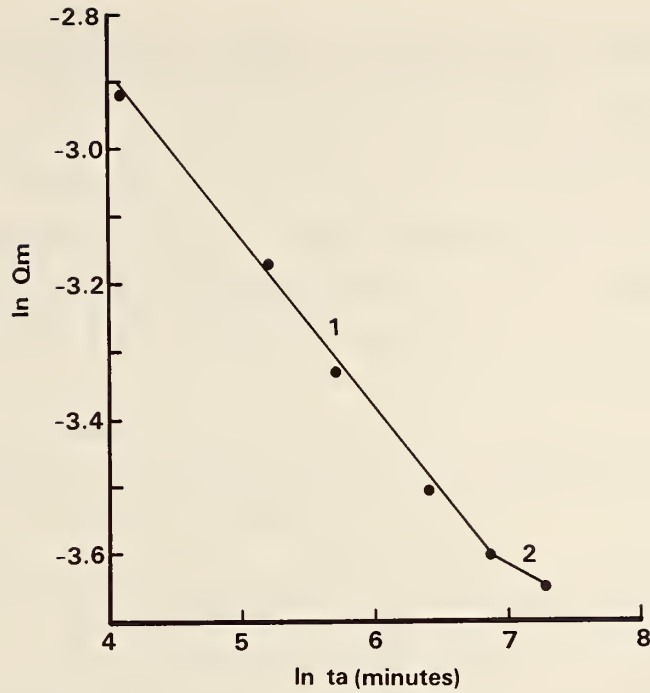


Figure 2. Variation of peak position (Q_m) as a function of aging time (t_a).

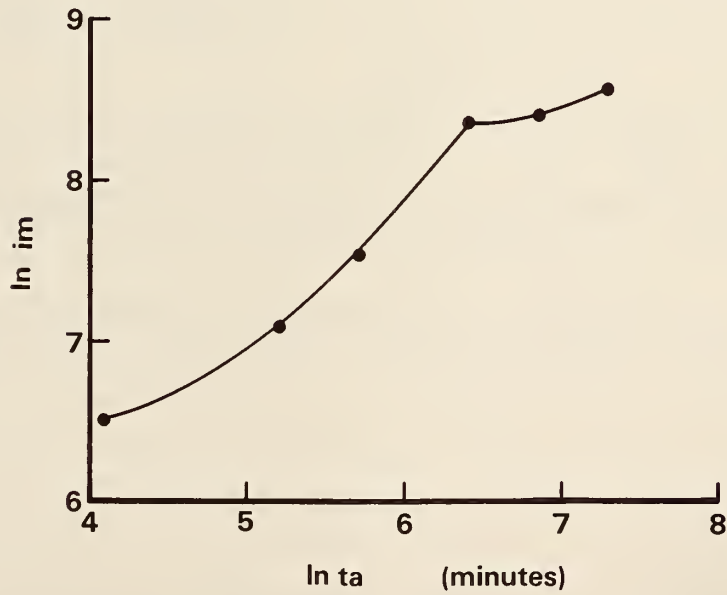


Figure 3. Variation of normalized peak intensity (I_m) as a function of aging time (t_a).

Ardell and Nicholson and Kirkwood performed their isothermal aging experiments at temperatures of 750°C and above. On the other hand, the aging temperatures used by Gentry and Fine were in the range of 425 to 450°C. It is, therefore, possible that Gentry and Fine's experiments were carried out in the spinodal region of the phase diagram. The aging temperatures used in our study are intermediate to these two studies.

Figure 2 shows a log-log plot of Q_m i.e. scattering vector at maximum intensities as a function of aging time. It would appear from this curve that two regimes of the decomposition process are clear. In regime I, the time dependence of Q_m is given by the equation

$$Q_m = 0.15 t_a^{-1/4}$$

where t_a is the aging time. This is suggestive of the fact that during stage I the system has not yet entered the conventional $t^{-1/3}$ coarsening regime (See reference 4). In regime II the rate of coarsening appears to have slowed down, although one needs to carry out the experiments for longer aging times to confirm this. Similar behavior was seen by Wilkes and Saundersen⁵ during the coarsening studies in a Cu-Ni-Cr alloy where they observed a transient arrest in coarsening kinetics before entering into $t^{-1/3}$ type of growth.

Figure 3 shows a log-log plot of normalized peak intensity (I_m) as a function of aging time. One of the striking features of this curve is an intermediate slowing down of the growth of peak intensities between aging times of 10 and 15.5 hours. According to recent theoretical analysis of Ditchcock and Schwartz⁶, in later stages of spinodal decomposition the peak intensity approaches a constant value having no time dependence (e.g. see figure 3 of reference 6). An alloy in this state is said to be in the "stationary state" of the spinodal process. From figure 3 it appears that after an aging time of 10 hours at 600°C the alloy has reached this stationary state. The main characteristic of the stationary state is that the amplitude of the compositional modulation wave approaches the value dictated by the phase boundaries of the metastable miscibility gap.

Similar behavior was seen by Singhal⁷ in the later stages of the spinodal decomposition in a Au-60 at % Pt alloy. The rise in peak intensities on further aging (after 15.5 hrs) can be attributed to Ostwald Ripening type of process⁸ where larger particles grow at the expense of smaller ones due to the higher surface to volume free energy ratio of the latter. Detailed analysis of these and other features of phase decomposition in Ni-Al alloys is in progress presently.

-
1. A. J. Ardell and R. B. Nicholson, "On the Modulated Structures of Ni-AR Alloys," *Acta. Met.* 14, 1295 (1966).
 2. D. H. Kirkwood, "Precipitate Number Density in a Ni-AR Alloy at Early Stages of Aging," *Acta. Met.* 18, 563 (1970).
 3. A. W. West and D. H. Kirkwood, "Nucleation and Precipitate Densities in a Nickel-Aluminum Alloy," *Scripta Met.* 10, 681 (1976).
 4. W. O. Gentry and M. E. Fine, "Precipitation in Ni-11.1 Atomic % Al Alloy and Ni-13.8 Atomic % Al Alloys," *Acta. Met.* 20, 181 (1972).
 5. P. Wilkes and R. I. Saunderson, "Coarsening in the Cu-Ni-Cr System," *Acta. Met.* 26, 1357 (1978).
 6. B. Ditchek and L. M. Schwartz, "Diffraction Study of Spinodal Decomposition in Cu-10 W% Ni-6 W% Sn," *Acta. Met.* 28, 807 (1980).
 7. S. P. Singhal, "Small-Angle Neutron Scattering and TEM Studies of the Phase Decomposition in the Au-Pt System," Ph.D. Thesis State University of New York at Stony Brook, (1980).
 8. J. M. Lifshitz and V. V. Slyozov, "The Kinetics of Precipitation from Supersaturated Solid-Solutions," *J. Phys. Chem. Solids* 19, 35 (1961).

THERMAL MOTIONS IN AMMONIUM PERCHLORATE

C. S. Choi and H. J. Prask

(Energetic Materials Division, LCWSL, ARRADCOM, Dover NJ)

and

(National Bureau of Standards, Washington, DC)

Huller has recently developed a theoretical model for rotational, quantum-mechanical tunneling of tetrahedral XH_4 groups in solids¹ and applied the model to the interpretation of neutron inelastic scattering measurements of tunneling states in NH_4ClO_4 . Relative librational force constants extracted from the analysis were found to be in excellent agreement with librational amplitudes determined from our low-temperature single-crystal neutron diffraction measurement.² However, a force-model calculation³ did not yield hydrogen equilibrium positions in agreement with the measured structure. In view of this, we have redetermined the crystal structure using ND_4ClO_4 , both single-crystal and powder, to confirm our previous results and to more completely characterize ammonium-ion dynamics in the 10 to 80K temperature range.

1. Single Crystal Study

Reflection data were collected at two different temperatures, 20K and 75K, within the scattering sphere up to 0.6 \AA^{-1} in $\sin\theta/\lambda$. In the crystal structure refinements (space group Pnma), the deuterium atoms of the ammonium group were constrained to rigid-body thermal motions. The refinement for the 20K structure converged rapidly to the final R indices $R = 0.038$ and $R_w = 0.037$. The refinement of the 75^oK structure was repeated with several different fixed values of secondary extinction coefficients, and final R value $R = 0.094$ and $R_w = 0.096$ were obtained. Shifts in atomic positions are compared with those of the hydrogenous compound at different temperatures in figure 1. The positional shifts (nonhydrogenous atoms) are more pronounced at temperatures below 78K, which may

be attributed to the sharp increases in the librational motion of ammonium group observed in that temperature region. The structure and thermal motions of the ND_4 groups are essentially the same as those of NH_4 except for small temperature-dependent positional shifts and changes in libration amplitudes.

2. Powder Diffraction Study

The librational amplitude of the ND_4 group at 30K, 45K, and 60K were studied by a neutron powder diffraction refinement with instrumental parameters: $\lambda = 1.542\text{\AA}$, $2\theta(\text{mono}) = 74.2^\circ$, $2\theta_{\text{max}} = 120^\circ$, $\Delta(2\theta) = 0.1^\circ$ and collimation of $20'-20'-10'$. Positional parameters of the perchlorate group were obtained from the single crystal structures of 20K and 75K by linear interpolation (proportional to temperature changes) and were excluded from the refinement. The ND_4 group was treated as rigid with translational and librational motion only. The R indices of the refinements were $R_1 = 5.6$ $R_p = 4.0$ $R_w = 5.2$ $R_e = 1.9$ for the 30K structure and 6.1, 3.8, 4.9 and 1.9 respectively for the 60K structure. The 45K structure study has not been completed.

3. Librational Motion of the Ammonium Group.

The root-mean-square amplitudes of librations for the ammonium group at different temperatures are summarized in Table 1. The deuterated and hydrogenous ammonium groups both undergo very large amplitude libration about an axis with essentially identical orientation in the observed temperature region, 10K to 78K. The temperature dependent rms amplitudes show a saturated value, approximately 30° , at temperatures 60K and above.

The amplitudes of librational motion obtained from the single-crystal data has been used to extract librational frequencies in a harmonic approximation (Table 1). It is interesting to note that at the lowest temperatures the isotope shift of the librational frequency corresponding

Table 1. Summary of rigid body libration amplitudes of ammonium group.

Temperature	Principal Axis	$\chi_{h W_L} (\text{Cm}^{-1})^*$	rms $L(^{\circ})$	l	m	n
10K	1	44	20.8	0.6845	0.	0.7290
	2	147	11.4	0.	1.	0.
	3	187	10.1	-0.7290	0.	0.6845
78K	1	52	29.6	0.6901	0.	0.7237
	2	98	16.4	0.	1.	0.
	3	110	15.0	-0.7237	0.	0.6901
b) <u>ND₄ ion</u>						
20K	1	41	16.1	0.6487	0.	0.7610
	2	101	9.7	0.	1.	0.
	3	145	8.1	-0.7610	0.	0.6487
(30K)**	1		22.0	0.6215	0.	0.7834
	2		10.4	0.	1.	0.
	3		4.9	-0.7834	0.	0.6215
(60K)**	1		29.7	0.6184	0.	0.7859
	2		10.9	0.	1.	0.
	3		5.4	-0.7859	0.	0.6184
75K	1	35.5	28.5	0.6608	0.	0.7505
	2	59	17.8	0.	1.	0.
	3	79	13.8	-0.7505	0.	0.6608

* librational frequencies from Cruickshank⁵.

** Neutron powder diffraction refinement.

to the largest amplitude libration is on the order of only 10% whereas the isotope-shifted frequencies of librations about the other two axes is close to the expected $\sqrt{2}$ shift (i.e. $\sqrt{I_H/I_D}$). This result is very important for the interpretation of Raman data in which a very temperature-dependent mode was observed in NH_4ClO_4 at 50cm^{-1} in the polarization in which the large amplitude libration should be observed.⁴ However, the isotope shift in ND_4ClO_4 was found to be only 0.89 suggesting that this was not the expected libration. The present diffraction result, on the other hand, indicates that this mode is very probably the expected libration.

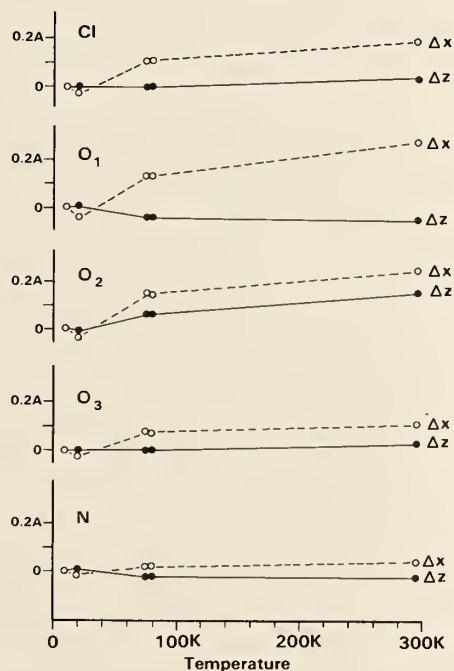


Figure 1. Comparison of atomic positions at various temperatures Δx and Δz , in Å unit, are the positional changes of each atom from its 10°K structure.

1. A. Hüller, *Phys. Rev. B*, 16, 1844, (1977).
2. C. S. Choi, H. J. Prask & E. Prince, *J. Chem. Phys.*, 61, 3523, (1974).
3. A. Hüller, Private communication, (1979).
4. G. J. Rosasco & H. J. Prask, *Solid State Commun.*, 16, 135, (1975).

5. D. W. J. Cruickshank, *Acta Cryst.*, 9, 1005 (1956).

THE DETECTION OF AN ORDER-DISORDER PHASE TRANSITION IN A MOLECULAR CRYSTAL BY COMPUTER MOLECULAR DYNAMICS

S. F. Trevino

(ARRADCOM, LCE, Dover, NJ)

and

(National Bureau of Standards, Washington, DC)

and

D. H. Trai

(Thermophysics Division)

We have recently begun a program designed for the investigation of the mechanisms by which energy released by a chemical reaction redistributes itself in condensed matter. The general outline of the work is as follows. We wish to model a diatomic molecule which is capable of dissociation into a state of lower energy (thus leading to a release of kinetic energy). This dissociation is effected through the interactions with neighboring molecules. In addition, we wish to allow recombination so as to better mimic nature. For this purpose, a pairwise potential is constructed of two parts, each a (6-12) type. The intermolecular potential whose minimum corresponds to the larger distance is chosen as the Lennard-Jones 12-6 potential. The intramolecular potential is scaled in a somewhat arbitrary fashion and is given by:

$$\Phi_{\text{itra}} = \left\{ \frac{4\epsilon}{n} \frac{\sigma}{nr}^{12} - \frac{\sigma}{nr}^6 \right\} + \frac{\epsilon}{2}$$

where ϵ and σ are the same parameters as in the Lennard-Jones potential, and n is a scale factor. We have used $n=3$ and $n=4$. Having thus defined the pairwise interaction of all the atoms, computer molecular dynamics is used to obtain the response of a collection of such particles to various stimuli. The initial step in our investigation is the construction of a perfect crystal modeled in the standard method by using periodic

boundary conditions of an array of diatomic molecules. The initial configuration consists in placing the center of mass of the molecule on an FCC lattice and allowing them to relax until a stable orientational configuration is obtained. This process led to a crystal structure very similar to that of N_2 in its lowest temperature phase with the single exception that the cell was slightly tetragonal ($c/a = 0.97$) rather than cubic. The crystal was heated while holding the volume constant and various properties were monitored. These included the total energy, the kinetic energy, the intramolecular distance, the single molecule angular correlation function ($G(\gamma) = \sum \delta(\gamma - \gamma_n) d\gamma$ where the sum is over the particles in the model and γ_n is the angle which the molecular axis makes with the z-axis, for example), etc. The initial intention of this experiment was to observe chemical decompositions. For this purpose, the intramolecular separation was carefully monitored. It was observed that, although the amplitude of the molecular stretch increased with temperature, the maximum separation of the two atoms of the molecule was never much larger than the distance to the minimum of the first potential. Our interpretation of this result is that in a perfect crystal lattice, decomposition is greatly hindered by the presence of neighboring molecules; and in addition, that increasing the pressure on the system also inhibits decomposition. It is clear to us from this that the role of defects (vacancies) is of crucial importance to the mechanisms of decomposition in the solid. It is our intent to study these details with our model. As the heating was continued, a lambda type order-disorder phase transition was detected. The transition is characterized by a pronounced continuous increase in internal energy as a function of temperature and in the width of $G(\gamma)$ as a function of γ until at just above the transition temperature $G(\gamma)$ is essentially a constant with γ .

C. NON-RRD PROGRAMS

ACTIVATION ANALYSIS: SUMMARY OF 1980 ACTIVITIES

Rolf Zeisler

The Activation Analysis Group has eight full-time and one part-time employees. Of these employees, seven are research scientists, one of whom is on detail for the Office of Measurements for Nuclear Technology and two are technical support personnel. The group hosts a guest worker from the Smithsonian Institution. The group is physically located in the reactor building where it utilizes office modules, measurement and counting laboratories (including one class 100 clean room), and radiochemistry laboratories.

The Activation Analysis Group, in support of the Inorganic Analytical Research Division, conducts research and analysis in four basic program areas:

1. Basic Research in Nuclear Analytical Chemistry

This activity is primarily aimed at improving the analytical measurement system using nuclear techniques. This includes analytical method development, improvement of instrumental and radiochemical analysis schemes, and all areas of analytical quantitation. Recent efforts are highlighted by high precision and high accuracy instrumental analysis of aluminum and the comparative determination of iodine in biological matrices after irradiation with thermal and fast neutrons and photons.

2. Analytical Research Applied to Specific Programs

This activity utilizes the group's analytical capability to provide reliable analytical data in the study of systems dependent on trace element composition. Specific efforts have been made in sampling and sample preparation methodology in order to provide meaningful analytical samples. The extended instrumental capabilities help the Activation Analysis Group to provide the vast number of analytical data, which combined with the results of other analytical techniques provide essential information on environmental and biological systems. The information is needed for example in the Chesapeake Bay Program and in the Pilot National Environmental Specimen Bank Program.

3. Analytical Support for the SRM Program

Analysis performed on new Standard Reference Materials (SRM's) are an extremely important area of the group's activity. Extreme emphasis is placed on the accuracy of analytical results. These efforts are backed by the essentially blank free activation analysis procedures and vast applications of instrumental analysis.

4. Service Analysis

Service Analyses are a small but important part of the group's analytical program, chiefly undertaken to expedite another NBS program or when the analytical capability cannot be obtained otherwise. There are many cases where a unique measurement is needed, thus triggering development of new nuclear analysis capabilities.

The summaries of the work completed this year in the four basic program areas are included below. More detailed descriptions of projects can be obtained from literature references or individual program reports.

1. Basic Research in Nuclear Analytical Chemistry

a. Pulse Pileup Correction Methods

R. M. Lindstrom

A significant source of error in activation analysis is the loss of counts at high counting rates due to pulse pileup. Wytttenbach¹ showed that a simple model based on the non-extending dead time formalism can correct for this loss with acceptable errors at dead time above 20%. His formulation, however, involved an unnecessary mathematical approximation; a better formula for the correction factor is

$$I(\text{true})/I(\text{observed}) = \exp (P \cdot DT/LT), \text{ where}$$

$$DT = CT - LT$$

CT = elapsed clock time

LT = elapsed live time

P = a constant, proportional to the amplifier time constant τ .

A FORTRAN program, PILSET, has been written to determine P and its statistical uncertainty from a set of observations of a reference source in the presence of variable amounts of interfering activity. The dependence of P on the amplifier time constant τ is shown in figure 1. The detector resolution is plotted on the same graph; a balance between good resolution and small pileup correction requires setting τ at 1-2 μ s for most work.

This model has been tested in an interlaboratory comparison of source strength measurements, organized by the International Atomic Energy Agency (IAEA). Two separate sets of measurements were reported, one with pileup corrections made as described above, and another using a commercial pileup rejector - livetime corrector. As can be seen by figure 2, both methods give acceptable agreement with the source strengths given by IAEA.

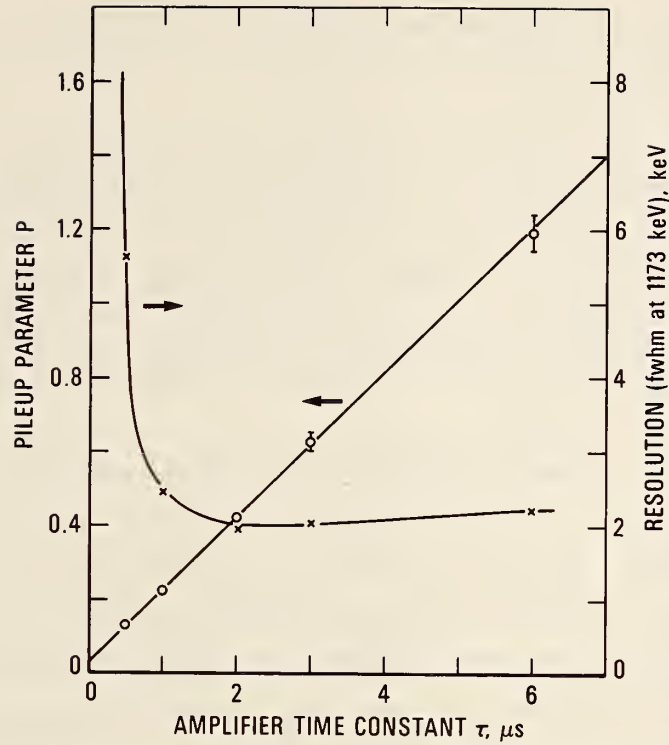


Figure 1. Pileup parameter P versus amplifier time constant τ .

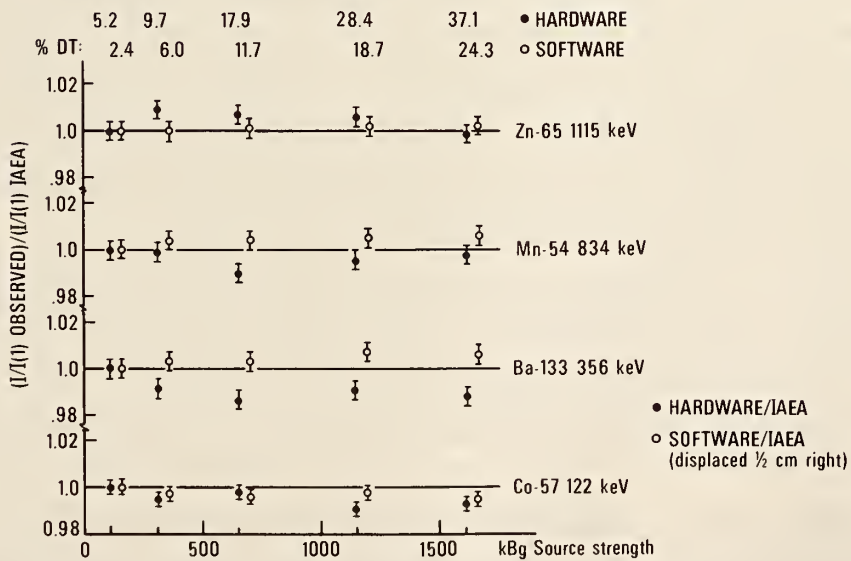


Figure 2. Hardware versus software pileup correction.

b. High-Accuracy Aluminum Determination by Neutron Activation

R. F. Fleming and R. M. Lindstrom

Aluminum, the second most abundant cation in the earth's crust, is certified in only two of the thirteen environmental and biological SRM's in the current catalog, largely because there are few reliable methods of measuring this element at NBS. Non-destructive neutron activation has progressed recently so that we understand and can eliminate all sources of systematic error. Precision is limited by counting statistics, but this may be very small.

The initial phases of this work have been successfully completed. The kinetic equations have been solved rigorously, with all parameters included: radioactive decay, dead time, and pulse pileup. The aluminum concentration of a material (single-crystal sapphire) of precisely known composition, with an accuracy limited only by counting statistics at the 0.5% level. All systematic biases have either been compensated for or the necessary corrections have been measured and verified. The measured aluminum concentration was found to be $52.78 \pm 0.30\%$, which can be compared to the true value of 52.952%. (The reduced χ^2 is 2.1.) The major corrections required to the data were for count rate dependent effects, as expected. In extreme cases these corrections were as great as 15%. The next phase of this work is to apply the capability established to the more complex matrices of the SRM bauxites. Soon after irradiation essentially all activity is Al-28. Therefore, during irradiation and counting are necessary for results as good as those for sapphire.

Results to data on the bauxites are extremely encouraging. Sources of bias, due to the coarseness of commercially available time bases and of irradiation and counting geometry, have been detected and eliminated with improved experimental design. The dominant remaining uncertainty in the best of our measurements may be neutron absorption by the hydrogen in the sample and its container. The magnitude of this effect is difficult to calculate; it could be a few tenths of a percent. Normalizing, the concentrations to SRM 676, our best results for the four bauxites is as follows:

NON-RRD PROGRAMS

SRM	69b	696	697	698
Aluminum certified (relative)	0.895 <u>±</u> 0.004	1.000 <u>±</u> 0.006	0.840 <u>±</u> 0.004	0.884 <u>±</u> 0.007
Aluminum measured (relative)	0.900 <u>±</u> 0.004 0.898 <u>±</u> 0.003	1.000 <u>±</u> 0.004 1.000 <u>±</u> 0.003	0.828 <u>±</u> 0.004 0.835 <u>±</u> 0.003	0.873 <u>±</u> 0.005 0.879 <u>±</u> 0.003

We are close to showing that activation analysis is a fully reliable method of aluminum measurement, able to stand alone for certification if carefully done. We expect to demonstrate even higher accuracy in the future for other elements.

c. Determination of Total Iodine in Biological Materials

G. J. Lutz

During a visit to the University of Michigan reactor several months ago, we conducted some irradiations inside a boron nitride cup and lid. This effectively screens out the thermal component of the neutron flux and relatively enhances capture reactions which have significant resonance in the epithermal region as well as fast neutron reactions.

Although iodine exhibits an excellent intrinsic sensitivity for determination by thermal neutron activation analysis, the limit of non-destructive determination in biological materials is 10-20 ppm. This is because the activation product I-128 has a short half-life and a not particularly favorable decay scheme. The photopeak associated with the decay of I-128 is obscured by Compton continua of higher energy photo-peaks of the activation products of various elements, including manganese, sodium, bromine, chlorine, and aluminum. When the irradiation is conducted with epithermal neutrons, the production of I-128 is reduced by about an order of magnitude, but the production of interfering nuclides is reduced by roughly two orders of magnitude. Lower levels of non-destructive determination of iodine are then of the order of tenths of parts per million.

It is expected that NBS will certify one or more of its biological SRMs for total iodine content. Currently at NBS, the two most reliable

methods for iodine seem to be the epithermal neutron activation analysis described above and instrumental photon activation analysis. A rather limited comparison of some samples by both methods has been accomplished and results from this exploratory work agree at levels of approximately 2 ppm of iodine to within 15-20%.

We have obtained some kelp tablets and have crushed (to powder), homogenized and dried a portion of them. Their iodine content is approximately 200 ppm. This level makes errors due to counting by either activation method highly unlikely. Whether we continue to get discrepancies of 15-20% or the two independent methods agree within random error at this level will provide clues as to the source of the problem.

d. Lithium and Lithium-6 Analysis with the Nuclear Track Technique
B. S. Carpenter (NBS) and L. J. Pilione (Pennsylvania State University)

Introduction

The concentration and distribution of lithium can be determined with the nuclear track technique if elements, such as boron, are not present in relatively large amounts.⁽¹⁾ The alpha particles produced by (n, α) reactions of different elements are for the most part indistinguishable with the nuclear track technique. In this investigation an absorbing material is placed between the sample and the detector such that the alpha particles are screened out while the tritons produced in the ${}^6\text{Li}(n, \alpha){}^3\text{H}$ reaction penetrate and produce etchable tracks.⁽²⁾ The triton track density produced in this fashion, is proportional to the lithium concentration and the lithium-6 isotopic abundance of the sample.

Methods and Analysis

To observe the effects of absorber thickness on the triton track density -- cellulose nitrate detectors (Kodak Pathe CA 80-15) were cut into strips ($\sim 0.5 \text{ cm}^2$) and heat sealed inside various thicknesses of linear polyethylene (12.5-55 μ meters). One-half dram vials ($\sim 1 \text{ ml}$ capacity) were filled with a standard lithium solution (1358 ppm Li, 7.45% ${}^6\text{Li}$) and the detector-absorber package positioned in the center of

the vial. The samples were exposed to thermal neutrons in the D₂O facility at the Breazeale Reactor, Pennsylvania State University. The detectors were retrieved and chemically etched in 2.5 N NaOH @ $50 \pm 0.5^\circ\text{C}$ for 25 minutes. Random fields of view were selected on both sides of the detector surface and the triton tracks counted with a Leitz optical microscope.

The data presented in table 1 indicates that the triton track density remains constant for absorber thicknesses between 12.5 and 25 μ -meters (the uncertainties represent one standard deviation = $1/(\text{total number of triton tracks})^{1/2}$).

As a check on the screening effect of the absorber (12.5-25 μ meters) against α -particles -- detector absorber packages were placed in vials containing boron solutions (1000 ppm). The samples were processed as before and no tracks above background were observed in the detector. The background tracks resulted from the reaction $^{14}\text{N}(n, p)^{14}\text{C}$ in the cellulose nitrate detector. The proton and triton tracks were found to be indistinguishable. In all cases blanks were exposed along with the samples and the proton track density subtracted out from the total to yield the net triton track density. This background set the lower limit of detection at 100 ppm Li, 7.4% Li-6.

Lithium solutions of known concentration and isotopic abundance were selected to verify the relationship between the triton track density and the lithium concentration and isotopic abundance. The known samples and blanks were processed as described previously (25 μ meter absorber). It can be seen from table 2 that a linear relationship exists between the triton track density and the lithium concentration. The effect of isotopic abundance was found by calculating the ratio of the triton track density to the lithium concentration for each sample. The results shown in table 3 indicate a linear relationship exists.

The isotopic abundance of the Atomic Absorption Standard was not specified by the manufacturer. Using the measured ratio and table 3, the isotopic abundance was found to be $7.48 \pm 0.44\%$.

Conclusion

It has been found that the concentration or isotopic abundance of lithium in solution can be determined using the nuclear track technique without interference problems from other elements present in the solution. The limit of detection is 100 ppm Li, 7.43% ^6Li with an accuracy of $\pm 6\%$. The process time/sample is ~ 15 minutes.

Table 1. Triton track density vs absorber thickness

Absorber Thickness (μ meter)	Triton Track Density ($\times 10^5 \text{ t/cm}^2$)
12.5	7.28 ± 0.29
15.5	7.21 ± 0.28
18.5	7.00 ± 0.28
21.5	7.00 ± 0.28
25.0	7.40 ± 0.30
28.0	7.00 ± 0.28
33.0	5.80 ± 0.23
35.0	5.14 ± 0.21
40.0	3.98 ± 0.16
45.0	3.01 ± 0.12
50.0	1.74 ± 0.07

Table 2. Triton track density vs lithium concentration

Sample	Lithium Concentration (ppm)	Triton Track Density (*10 ⁵ t/cm ²)
Atomic Absorption		
	500	9.25 ± 0.38
	333	6.43 ± 0.28
	250	4.98 ± 0.22
	167	3.55 ± 0.16
Standard Reference Material 924 (NBS, 4.60% ⁶ Li)		
	407	4.66 ± 0.17
	339	3.27 ± 0.12
	204	2.17 ± 0.08
	136	1.53 ± 0.06
Standard Reference Material #9 (NBS, 7.43% ⁶ Li)		
	378	7.12 ± 0.25
	315	5.76 ± 0.25
	189	3.84 ± 0.18
	126	2.71 ± 0.13
Oak Ridge National Lab (95.9% ⁶ Li)		
	38.4	8.47 ± 0.35
	32.0	6.49 ± 0.28
	26.0	5.41 ± 0.24
	12.8	2.97 ± 0.13
Oak Ridge National Lab and NBS SRM - #9 (20% ⁶ Li)		
	126	6.06 ± 0.26
	95	4.72 ± 0.21
	63	3.12 ± 0.15
	32	1.37 ± 0.07
Oak Ridge National Lab and NBS SRM - #9 (45% ⁶ Li)		
	126	13.4 ± 0.44
	95	9.37 ± 0.39
	63	6.08 ± 0.27

Table 3. Triton track density/lithium concentration vs lithium-6 isotopic abundance

Triton Track Density/Lithium Concentration ($\times 10^3 \frac{\text{t}}{\text{cm}^2}$) ppm	Lithium-6 Abundance (%)
1.08 \pm 0.08	4.60
1.97 \pm 0.11	7.43
4.75 \pm 0.32	20.0
10.1 \pm 0.56	45.0
2.16 \pm 1.31	95.9

-
1. R. L. Fleischer, P. B. Price, and R. M. Walker, *Nuclear Tracks in Solids: Principles and Applications*, University of California Press, Berkley (1975).
 2. B. S. Carpenter and L. J. Pilione, *NBS Technical Note 969*, 89-90, 1978.

2. Analytical Research Applied to Specific Programs

a. The National Environmental Specimen Bank (NESB)

S. H. Harrison and R. Zeisler

In the past year, the NESB program has progressed from the research and development phase into the first year of implementation of the pilot bank. This year was highlighted by the completion of the Specimen Bank laboratory and storage facility, implementation of the sample collection protocol, initiation of trace element analyses on banked samples, and further improvement and evaluation of the sample homogenization procedure.

The construction of the clean room facility was completed in November 1979. This facility, located in the NBS Reactor building, houses the specimen bank laboratory and storage rooms. Since construction was completed, it has been equipped with the items necessary for processing and storing samples. These items include upright compressor freezers operating at -80°C and -25°C , liquid nitrogen freezers holding samples in nitrogen vapor at temperatures less than -120°C , a dust-free cabinet for storing freeze-dried samples, a cabinet for storage of histological slides, oxygen monitor, biohazard hood, refrigerated shelf freeze dryer, and equipment for sample homogenization.

The collection of human liver specimens, the first sample type to be studied in the pilot bank of the NESB, was initiated this year through contracts with three medical schools. A very careful sample collection protocol¹ is being used by pathologists and their assistants. Liver specimens are shipped to NBS at cryogenic temperatures by an express air freight service. A total of 300 samples are targeted to be collected in the first year. About 10% of these will be processed for analysis by homogenization and subsampling into Teflon PFA jars.

The samples collected this year are analyzed for their trace element content only. The trace organic analysis is under methodology development this year and will be used for real sample analysis next year. Three inorganic analytical techniques will be used routinely for sample analysis. These are neutron activation analysis, voltammetry, and atomic absorption

Table 1. Instrumental neutron activation analysis of normal human liver.

Element	Concentration ($\mu\text{g/g}$ fresh wet)
Na	760
Mg	120
Al	0.74
Cl	360
K	2790
Cr	0.05
Mn	0.83
Fe	154
Co	0.039
Cu	7.1
Zn	63
Se	0.35
Rb	3.7
Mo	0.90
Ag	0.05
Cd	0.93
Sb	0.007

spectrophotometry. Instrumental neutron activation analysis of the human liver samples is used to provide data on Na, Mg, Al, Cl, K, Cr, Mn, Fe, Co, Cu, Zn, Se, Br, Rb, Mo, Ag, Cd, Sb, La, and Hg. Representative data is presented in table 1. Radiochemical activation analysis has been used to analyze the livers for Cu, Cd, As, Se, Sb, and Mo. For major element analysis, prompt gamma activation analysis looks to be a promising technique after preliminary investigation of a liver sample. In addition to activation analysis methods, voltammetry is used to analyze for Cu, Cd, Pb, Ni, and Zn, and atomic absorption spectrophotometry is used for Be, Al, Cr, Ni, Sr, Se, Ba, and Pb.

The brittle fracture technique for cryogenic homogenization of samples was pioneered by G. Iyengar.² We have modified his design, which was only capable of handling 5 to 10 g of sample per batch, so that 250 g of frozen liver can be homogenized at a time and the preliminary results indicate that 1 g subsample of the homogenate is a satisfactory representative of the whole.

-
1. "Sampling and Sample Handling Protocols for Human Livers," S. H. Harrison in Pilot Program for the National Environmental Specimen Bank-Phase I, Sally H. Harrison, Rolf Zeisler, and Stephen A. Wise, Editors, NBS Special Publication in preparation.
 2. Iyengar, G. and Kasperek, K., *J. Radioanalytical Chem.*, p. 301-315 (1977).

b. Analysis of Chesapeake Bay Water and Associated Suspended Solids
R. R. Greenberg, H. M. Kingston, and E. S. Beary

As part of a multidisiplinary and multiagency study of the Chesapeake Bay, 102 water samples and the filtered suspended solids from these samples are being analyzed by neutron activation analysis. The samples were collected 1 m below the surface, and 1 m above the bottom at 52 different locations throughout the bay. Approximately 30 full-process blanks were also collected and are being analyzed. Pre-irradiation, ion-exchange chromatography is used to concentrate the elements of interest from the water samples, and separate them from interfering matrix elements such as Na, Cl, and Br. After filtration, 100 mL of water is passed through pre-cleaned chelex 100 chelating resin in a class 100 clean room. The resin is washed with 1.0 M ammonium acetate, washed with ultrapure water, dried, and irradiated for four hours in RT-3. Samples of SRM 1643a (trace elements in water) are being processed and analyzed with the bay water samples to check the accuracy of the procedure used.

The results of the analyses completed indicate great variation among samples, as illustrated in table 1. The concentration of many elements in the filtered particulate fractions vary over two orders of magnitude. To a large extent, this is due to differences in total mass loadings on the filters. Various factors can influence the amount of particulate material suspended in the bay water such as: current; tide; temperature; wind conditions; etc., making interpretation of the data difficult. One approach which appears to be useful in this study is to compare the elemental ratios among the different sample locations instead of the absolute concentrations. By normalizing to a crustal element, such as Sc, the problems caused by differing mass loadings are essentially eliminated. The particulate Fe concentration, for example, in sample 11005 (table 1) is 150 times greater than in sample 11032, however, their Fe/Sc ratios are essentially the same (3200 compared to 3700).

When completed, this study may prove useful in identifying anthropogenic and/or natural sources to the Chesapeake Bay. In addition, since these

Table 1. Concentration ng/mL*

Element	Filtered Particles			Dissolved		
	Blank-13	Sample-11032**	Sample-11005**	Blank-3B-R1	Sample-11032**	Sample-11005**
Cd	< 0.02	< 0.3	< 0.5	< 0.06	< 0.09	< 0.3
Co	< 0.006	0.028+0.003	1.02+0.05	0.0110+0.006	0.067+0.003	0.049+0.003
Cr	2.3+0.1	2.3+0.1	7.4+0.4	1.55+0.08	1.66+0.08	2.4+0.1
Fe	1.1+0.2	19+1	2840+140	1.00+0.05	2.1+0.2	3.8+0.2
Mo	< 0.009	< 0.05	0.2+0.2	0.03	3.1+0.2	3.8+0.2
Sc	0.00013+0.00002	0.0049+0.0002	0.90+0.05	0.00014+0.00001	0.00046+0.00002	0.00072+0.00004
Sn	< 0.2	< 0.4	< 6	< 0.2	< 0.5	< 0.6
Th	< 0.0006	0.0043+0.0005	0.66+0.03	0.00042+0.00008	0.0021+0.0003	< 0.0009
U	< 0.00007	0.008+0.001	0.16+0.01	0.0013+0.0005	0.93+0.05	1.05+0.05
Zn	0.50+0.03	0.83+0.08	15.3+0.8	0.59+0.03	8.7+0.5	1.84+0.05

*Uncertainties are the estimated overall analytical uncertainties at the 1 S level.

**Blank values have not been subtracted from the samples.

NON-RRD PROGRAMS

samples were collected concurrently with sediment, pore water, and benthic studies, both the water to sediment equilibrium and the aquatic population will be correlated.

c. I-129 Analysis

G. J. Lutz

A project has recently been initiated to set up the equipment for I-129 analysis with a view of certifying a botanical Standard Reference Material for its I-129 content.

The analysis consists of a pre-irradiation separation, an irradiation in the reactor, and a post-irradiation separation. The pre-irradiation separation involves spiking the sample with I-125 traces for subsequent yield determination and combustion of the sample in a stream of oxygen. The off gases are filtered through glass wool to trap out any particulate material and the iodine is trapped on activated charcoal. The pre-irradiation filtering is necessary to remove cesium, and tellurium which could interfere via the reactions respectively $^{133}\text{Cs}(n,\alpha)^{130}\text{I}$, $^{235}\text{U}(n,f)^{129}\text{I}(n,\gamma)^{130}\text{I}$, and $^{128}\text{Te}(n,\gamma)^{129}\text{Te} - ^{129}\text{I}(n,\gamma)^{130}\text{I}$.

The charcoal trap containing the iodine is then sealed in quartz and irradiated in the reactor for a suitable length of time. After a short cooling period, a few milligrams of inactive iodine carrier is added. The major activities are those due to chlorine, bromine, and impurities in the activated charcoal. The charcoal and carrier are burned in a stream of oxygen. The off gases are again passed through a plug of glass wool to filter out particulate material. The collecting trap consists of a bed of hydrated manganese dioxide (HMD) followed by a charcoal trap for collecting the iodine. HMD is one of a series of selective ion retention media developed during the past several years. It is usually used for separations from aqueous solutions, but has been applied to gas phase separation.

Over a fairly wide temperature range, a bed of HMD will remove

NON-RRD PROGRAMS

99.9%+ of chlorine and bromine from a gas stream while passing > 95% of the iodine.

Tracer studies have been completed on the pre- and post-irradiation separations and the final apparatus to be used is being constructed.

d. Consistency Study of Re-Refined Lubricating Oils

R. F. Fleming

The Bureau was mandated in the Energy Policy and Conservation Act of 1976 to develop and evaluate a set of test procedures necessary to establish the "substantial equivalency" of a re-refined lubricating oil when compared to virgin oils. As part of this effort, the Recycled Oil Program (Office of Recycled Materials) has set up a study of approximately 40 tests to be performed on eleven lubricating oils (six re-refined, four virgin, and a check sample) each month for a year. As part of these tests, the concentration of chlorine and of bromine are being determined by neutron activation analysis. It is the consistency of these measurements over the twelve month period which is of particular interest, although absolute concentrations may also be found important.

Since neutron activation analysis of the oils is capable of a sensitivity of 30 ppb for both elements, it is the only analytical method which can provide the required precision and accuracy for this study. Preliminary results indicate that the measurements easily distinguish between virgin and re-refined oils, and are able to monitor significant changes in halide concentrations with time.

NON-RRD PROGRAMS

3. Certification Analysis of SRM's.

a. New Biological SRM's: Bovine Liver and Citrus Leaves

R. R. Greenberg, R. Zeisler, R. M. Lindstrom, G. J. Lutz,
S. Harrison, and J. V. Bailey

Two new bovine liver Standard Reference Materials (1577A and 1577B), and a new citrus leaves SRM (1572) have recently been prepared and are currently being analyzed. Both instrumental neutron activation analysis (INAA) and radiochemical neutron activation analysis techniques have been used. The elemental concentration determined so far are listed in table 1.

NON-RRD PROGRAMS

Table 1. Elemental Concentrations in New Biological SRMs Concentration - $\mu\text{g/g}$ unless % indicated.

Element	Method	Bovine Liver SRM-1577A	Bovine Liver SRM-1577B	Citrus Leaves SRM-1572
Ag	INAA	0.050 \pm 0.011	0.040 \pm 0.010	
Ag	RNAA	0.045 \pm 0.001		
Al	INAA	3.1 \pm 0.8	2.9 \pm 1.0	93 \pm 5
As	INAA			3.12 \pm 0.14
As	RNAA	0.046 \pm 0.004		
Ba	INAA			21.4 \pm 0.6
Br	INAA	9.0 \pm 0.1	9.7 \pm 0.1	
Ca (%)	INAA			3.18 \pm 0.09
Cd	RNAA	0.430 \pm 0.004		
Cl	INAA	2760 \pm 120	2700 \pm 160	
Co	INAA	0.242 \pm 0.005	0.255 \pm 0.006	
Cr	INAA	0.43 \pm 0.28	0.31 \pm 0.21	0.74 \pm 0.09
Cr	RNAA	0.29 \pm 0.13		
Cs	INAA			0.098 \pm 0.005
Cu	INAA	153 \pm 8	163 \pm 10	
Cu	RNAA	158 \pm 1		
Fe	INAA	194 \pm 4	195 \pm 4	92 \pm 7
K (%)	INAA	0.96 \pm 0.05	0.97 \pm 0.09	1.90 \pm 0.07
Mg	INAA	520 \pm 180	520 \pm 120	6100 \pm 200
Mn	INAA	9.6 \pm 0.8	9.3 \pm 0.3	22.6 \pm 0.9
Mo	RNAA	3.2 \pm 0.1		
Na	INAA	2200 \pm 30	2190 \pm 30	160 \pm 13
Rb	INAA	12.7 \pm 0.3	12.9 \pm 0.3	5.0 \pm 0.2
Sb	RNAA	0.0029 \pm 0.0003		
Sc	INAA			0.0109 \pm 0.0007
Se	INAA	0.73 \pm 0.02	0.73 \pm 0.04	
Se	RNAA	0.72 \pm 0.04		
Zn	INAA	124 \pm 1	125 \pm 2	30.5 \pm 0.9

NON-RRD PROGRAMS

b. Analysis of Obsidian SRM 278 and Basalt SRM

M. J. Blackman

Two new silicious rock standard reference materials: obsidian, a natural glass with the approximate composition of granite; and basalt, a basic igneous rock were analyzed by instrumental neutron activation. Sodium, manganese, potassium, and dysprosium were sought. Table 1 presents the results of this analysis.

Table 1. Na, Mn, and Dy in Obsidian SRM and Basalt SRM.

	Obsidian	Basalt
Na %	$3.62 \pm 0.06^*$	$1.61 \pm 0.02^*$
Mn $\mu\text{g/g}$	395 ± 14	1285 ± 13
Dy $\mu\text{g/g}$	5.73 ± 0.59	---

* indicate 2 standard deviations

4. Service Analysis

a. Measurement of the Co-60 to Co-59 Ratio in Microparticles

R. F. Fleming and R. M. Lindstrom

If a cobalt-bearing steel is subjected to neutron irradiation and at a subsequent time the ratio of cobalt-60 to cobalt-59 atoms and the ratio of iron-55 to iron-54 atoms are measured, it is possible to determine both the decay time since the end of irradiation and the neutron fluence to which the particle was exposed. For this purpose, we developed two methods for the determination of the cobalt ratio and applied them to particles ranging in mass from 80 ng to 300 μg . The measurements were carried out at the ORR reactor in Oak Ridge during the period of the NBSR shutdown.

The first method is the approach of conventional neutron activation analysis. The sample was irradiated along with a known mass of elemental cobalt as a standard. The 58.6 keV gamma emitted by the 10.47 minute $^{60\text{m}}\text{Co}$ activity produced was counted using a thin Ge photon detector. This gave the Co-59 mass. The number of Co-60 atoms was determined by counting the particle against a Co-60 standard source (SRM-4210). This gave the specific activity of the particle as Ci of $^{60}\text{Co}/\text{gram } ^{59}\text{Co}$.

The direct measurement of the $^{60}\text{Co}/^{59}\text{Co}$ ratio was also done by NAA. For this, a known mass of cobalt was irradiated along with a Co-60 source of known activity. In addition to the $^{59}\text{Co}(n,\gamma)^{60\text{m}}\text{Co}$ gamma, we also measured the activity of the 67.4 eV gamma from the 99 minute Co-61 produced by $^{60}\text{Co}(n,\gamma)^{61}\text{Co}$. This provided a calibration of the irradiation/counting system since

$$\frac{N_{60}}{N_{59}} = \frac{A_o^{61}}{A_o^{60\text{m}}} \left[\frac{\sigma_{59} \Gamma_{60\text{m}} \epsilon_{60\text{m}}}{\sigma_{60} \Gamma_{61} \epsilon_{61}} \right]$$

where $A_o \equiv \frac{\lambda C e^{\lambda t_i}}{(1-e^{-\lambda \tau})(1-e^{-\lambda \Delta})} \frac{e^{\lambda \delta} - 1}{\lambda \delta}$

with λ = decay constant

C = net counts in

τ = irradiation time

Δ = live time of count

δ = dead time of count

t_i = time from irradiation end/to start of count

σ = activation cross section

Γ = gammas per decay

ϵ = detector efficiency

The measurement gave the calibration factor (in square brackets) as 0.229 ($\pm 10\%$) so that the specific activity is given as

$$\text{Ci } ^{60}\text{Co} / \text{g } ^{59}\text{Co} = 264 \frac{A_o^{61}}{A_o^{60m}}$$

This second method has the important advantage that all geometry effects during irradiation and counting are eliminated. This proved to be crucial in the case of particle D10A which was not visible and hence difficult to position precisely. The results are given below by both methods showing excellent agreement, except for D10A for which the direct method gives the more reliable result.

Particle	Weight (μg)	^{60}Co Activity (μCi)	$\text{Ci } ^{60}\text{Co} / \text{gm } ^{59}\text{Co}$	
			Direct	Conventional
G2	300.3	12.8	-	0.91
D1	66.2	9.30	1.36	1.34
RF	28.0	8.97	10.4	10.2
G1	15.7	5.58	11.6	11.6
HEX 7-1	134.3*	257	-	19.6
D10A	0.083	2.59	335	282

*Estimated from dimensions.

b. Study of the Selenium Dependancy of Cardiac Mitochondrial
Glutathione Peroxidase

R. Zeisler

Introduction:

Cardiac mitochondria generate significant quantities of hydrogen peroxide as a byproduct of normal metabolism. This toxic product must, of course, be disposed of before it causes severe damage to mitochondria and surrounding organelles. For this reason, the existing defenses of mitochondria to hydrogen peroxide attack are naturally of interest. There are two major enzyme classes able to destroy hydrogen peroxide. Catalase is one of these. This enzyme catalyzes the conversion of two moles of hydrogen peroxide to one mole each of oxygen and water. The second class is the glutathione dependant peroxidases. These enzymes use glutathione to reduce hydrogen peroxide to water. The known glutathione peroxidases are all soluble enzymes which contain selenium in their active site. Indeed, tissue activity of this enzyme appears to be strictly dependant on dietary selenium. This enzyme and its selenium dependancy is of considerable economic importance as well. Selenium deficiency leads to diseases of economic importance in pigs, lamb, and chicken. In most of these cases, the diseases have been associated with a resultant lack of glutathione peroxidase activity. This enzyme may also be involved in protection against chemical carcinogens and radiation damage. In spite of all of this, it is obvious that there are considerable species variation in sensitivity to selenium deficiency and this has suggested that other mechanisms of peroxide removal must exist and that in certain species these mechanisms supplant the selenium dependant glutathione peroxidase. For this reason, we have reexamined the whole problem.

Results:

We have isolated mouse cardiac mitochondria and found them to be a rich source of glutathione peroxidase. Furthermore, this mitochondrial activity was unaffected by prolonged selenium deficiency sufficient to

eliminate the previously described selenium dependant enzyme in the cytosol. Next we studied distribution within the mitochondria and found it to sediment with the mitochondrial membrane, not with the mitochondrial matrix. All of this information suggested that we were dealing with a new enzyme which was membrane bound and not dependent on dietary selenium.

We next took, whole mitochondria, mitochondrial membrane, and mitochondrial matrix from normal and selenium deficient animals and measured glutathione peroxidase activity and selenium content via neutron activation analysis. The results showed that the deficient animals had half the selenium concentration of the control animals in each fraction examined. These results serve to further demonstrate the difference between this newly described enzyme and the well known selenium dependent glutathione dependant glutathione peroxidase.

Future Plan:

To finally prove the selenium independance of this enzyme we need to purify it to homogeneity and show absence of selenium in that preparation.

c. High Resolution Depth Profiling Using Thermal Neutron Beams

R. F. Fleming and I. G. Schroder (Nuclear Radiation Division)

The joint effort with Sandia Laboratories Albuquerque, NM (Dr. J. M. Harris) to investigate the use of thermal neutron beams to determine the amount and depth profile of isotopes such as He-3, Li-6, and B-10 in metal and semiconductor substrates, has continued.

The depth profiling technique using thermal neutron beams involves illuminating a target with a beam of thermal neutrons and measuring, with an energy-dispersive detector (silicon surface barrier), the energy distribution of the charged particles produced. Since the incident neutron energy is completely negligible compared to the reaction Q-value (E_0) the charged particles produced are both monoenergetic and isotropic. Those particles which escape from the sample lose energy along their exit path at a known rate dE/dx . The energy distribution of these particles at a fixed escape geometry is measured by a silicon surface

barrier detector. When subtracted from the initial energy (E_0), the energy loss distribution is obtained, which can be directly related to the depth distribution of the parent isotope via the known stopping power. Though the sensitivity, resolution, and maximum depth analysis vary greatly among isotopes, being dependent upon the reaction cross section and the Q-value, the neutron technique has significant advantages over conventional charged particle profiling methods such as Rutherford backscattering, proton-induced x-ray (PIXE), sputter-auger or ion beam analysis, especially for low-Z targets. These advantages include: the non-destructive nature of the neutron beam probe; the spatially uniform probe efficiency in samples which do not strongly attenuate the neutron beam; the lack of kinematic broadening so that the target depth distribution is monotonically related to the exiting particle energy via the particle's stopping power; and finally, the relative ease and speed of the measurements as the energy spectrum from an energy-dispersive detector gives a measure of the entire depth distribution in a single run.

The work to date has involved implants of He-3, Li-6, and B-10 as well as actual tritide targets of both ScT_2 and ErT_2 . Figure 1 shows an energy spectrum with a "surface" layer of He-3 on a Sc substrate. Figure 2 shows the broad proton distribution from the He-3 accumulated in a 1.5 μm thick ErT_2 target. These metal tritides (MT_2) are stoichiometrically loaded with tritium which, as it undergoes its natural 12-year beta decay, produces the helium-3. These tritides are fabricated as targets for high yield 14-MeV neutron generators which are used for defense, medical therapy, and analytical purposes. The buildup of the helium-3 and its migration in the tritide may have a significant effect on the long term integrity of the neutron targets.

The measurements performed with implantation loaded He-3 targets have shown that sensitivities of less than 10^{15} He-3 atoms/ cm^3 are possible and that by unfolding the observed proton spectrum and using the appropriate stopping power, depth resolution of less than 100 \AA can be obtained.

Table 1. Candidate for thermal neutron depth profiling

Elem.	Reaction	Target Half-life	atoms/mci or (% abund.)	Energy of Emitted Particles (keV)	Cross Section (barns)	Sensitivity (atoms/cm ²)
He	³ He(n,p) T	Stable	(.00014)	573	5327	2 x 10 ¹³
Li	⁶ Li(n,α) T	"	(7.5)	2056	940	1 x 10 ¹⁴
B	¹⁰ B(n,α) ⁷ Li	"	(20)	1473	3836	3 x 10 ¹³
Be	⁷ Be(n,p) ⁷ Li	53 day	2.5 x 10 ¹⁴	1439	48000	2 x 10 ¹²
Na	²² Na(n,p) ²² Ne	2.6 year	4.4 x 10 ¹⁵	2248	36000	3 x 10 ¹²
Ni	⁵⁹ Ni(n,α) ⁵⁶ Fe	8 x 10 ⁴ yr	1.3 x 10 ²⁰	4753	12	8 x 10 ¹⁵
N	¹⁴ N(n,p) ¹⁴ C	stable	(99.63)	584	1.8	6 x 10 ¹⁶
O	¹⁷ O(n,α) ¹⁴ C	"	(0.038)	1415	0.235	4 x 10 ¹⁷
S	³³ S(n,α) ³⁰ Si	"	(0.75)	3081	0.14	7 x 10 ¹⁷
Cl	³⁵ Cl(n,p) ³⁵ S	"	(75.77)	598	0.49	2 x 10 ¹⁷
K	⁴⁰ K(n,p) ⁴⁰ Ar	"	(0.012)	2231	4.4	2 x 10 ¹⁶

NON-RRD PROGRAMS

Sensitivity based on: 0.1 cps, 1% solid angle, 10⁸ n/cm²/sec flux

In the accompanying table are listed the feasible thermal neutron induced charged reactions which represent strong candidates for thermal neutron depth profiling. Along with each reaction and their relevant characteristics are listed the calculated sensitivity of each based on a count rate of 0.1 cps, a detector solid angle of 1%, and a neutron flux of 10^8 . By far the most attractive candidates are He-3, Li-6, and B-10 since they are stable and have large cross sections. We have obtained results for all three reactions. Besides the importance of He-3 in metal tritides, both He-3 and Li-6 depth distributions are of great interest to the thermonuclear fusion community for first-wall reactor design and for diffusion into metals. The distribution of lithium and especially boron in semiconductors is of course of great concern to the electronics community. In fact the recent explosive growth of ion beam depth profiling has been driven primarily by this need. Both Be-7 and Na-22 are of interest because of their huge cross sections even though the targets would be radioactive. (The radioactivity has the advantage, however, of allowing absolute measurement of the number of target atoms by gamma counting.) The study of sodium diffusion into metals and glasses is a long standing problem. The Ni-59 reaction would allow study of nickel diffusion into host metals--the physics of this reaction has already been thoroughly investigated at the NBSR.

At present, construction of a high purity 10^8 n/cm²/sec thermal neutron beam dedicated to depth profiling at the BT-3 port of the NBSR has begun. With this beam, the previous work will be continued and many of the problems associated with table I will be investigated. The feasibility of the present technique must be demonstrated for radioactive samples (Be, Na, K) and for those isotopes with low reaction cross sections (N, O, S, Cl) which would be suitable for depth profiling only for matrices in which they form a major constituent.

5. Facilities

a. Facilities for Activation Analysis: Counting and Computation

R. M. Lindstrom

A number of gamma- and x-ray detectors are in use for assaying radioactive samples. These include four first-line detectors (two large Ge(Li) and two Gamma-X), five Ge(Li) detectors in the range of 12 ± 2 percent relative efficiency, two special-purpose detectors (Ge(Li) well and low-energy photon spectrometer), and two older, smaller Ge(Li) detectors in reserve. Three detectors have automatic sample changers for unattended counting of series of samples. Data are acquired through six analog-digital converters (ADCs) on an ND6620 computer-based data acquisition system and through three ND100 and one TN1710 hardwired multichannel analyzers (MCAs). Two of the MCAs can be controlled by and transfer data to and from the ND6620; all have magnetic tape and printer output.

Most data processing is done with the ND6620 system. In addition to the ADCs the system consists of two display and acquisition (DAS) terminals, a central processor, 224 kbytes of memory, 10 Mbytes of disk, 7-track and 9-track magnetic tape, two additional terminals, and a fast printer. The software purchased with the system is used for most work, and additional programs have been written for ADC assignment, pileup calibration, linear regression, and weighted mean calculations.

b. Activation Analysis Studies of Archaeological Artifacts

M. J. Blackman

The analysis of archaeological artifacts by instrumental neutron activation has continued. The goal of these investigations has been to use trace and minor element profiling in provenience studies and to examine the production and distribution of the various objects. The materials so far analyzed include ceramics from the southeast and southwest U. S. and from Western Asia; clay samples from the U. S. and Western Asia; and chert and nephrite from Labrador, Canada.

PRECISION GAMMA-RAY AND X-RAY WAVELENGTHS

E. G. Kessler, Jr., W. C. Sauder, and R. D. Deslattes
(Center for Absolute Physical Quantities)

Gamma- and x-ray wavelengths are measured using two crystal transmission spectrometers. These spectrometers are unique in the world because (1) crystals whose lattice spacing has been measured by x-ray/optical interferometry are used, and (2) angle measuring interferometry of high accuracy ($\sim 0.5 \times 10^{-3}$ sec) and absolute calibration is used. More experimental details are available in references 1, 2, and 3.

Over the past two and one-half years a significant number of wavelengths^{3,4} from Au-198, Ir-192, Yb-169, and Tm-170 have been published along with the W $K\alpha_1$ x ray.⁵

A measurement of the wavelength of the electron-positron annihilation radiation (511 keV) has been attempted but failed because of source irradiation and manipulation problems. The positrons which are produced in the radioactive decay of a Cu-64 source form positronium whose short lived singlet state leads to a three photon decay. The narrowing of the annihilation line is accomplished by mixing the singlet and triplet states in a magnetic field and by thermalizing the positronium in a cryogenic He gas.⁶

Significant changes in the Cu-64 source design and manipulation are being made to insure a successful measurement of this line. Thin sheets of Cu foil plated with Au appear to be inert in the irradiation thimble water and should prevent Cu contamination of the thimble water as was previously experienced. A simplified source-manipulator connection should permit easy insertion of the radioactive source into the He dewar. A measurement should occur in early 1981.

Some high Z K x rays produced at the 4 MeV electron Van de Graaff have been measured during the past year. Measurements over a wide Z-range permit tests of self-consistent field calculations.^{7,8} Because of the low efficiency of the two crystal spectrometers, only $K\alpha_1$, $K\alpha_2$, $K\beta_1$, and $K\beta_3$ transitions can be accurately (< 10 ppm) measured in a reasonable

time. Measurements of Ag ($Z = 47$), Er ($Z = 68$), Au ($Z = 79$), Pb ($Z = 82$), and U ($Z = 92$) have been made and measurements of additional elements such as Xe ($Z = 54$), Ba ($Z = 56$), Sm ($Z = 62$), and W ($Z = 74$) are anticipated.

Also during the past year, final analyses of the shape and energy of the erbium K absorption edge has been completed. This measurement was made to provide an energy calibration for kaonic potassium x rays which were studied by Lum and Wiegand⁹ of Lawrence Berkeley Laboratory. Because the 6-5 transition in kaonic potassium is coincident with the erbium K edge, a measurement of the absorption of the kaonic x rays by calibrated foils permits the assignment of energies to the kaonic x rays. The mass of the kaon can be deduced by comparing measured and theoretical values for the kaonic transition. A kaon mass value accurate to ± 110 ppm has been determined. A joint publication including the kaonic x-ray measurements and the foil calibration is in preparation.

Accurate higher energy (> 1 MeV) gamma-ray standards are needed for detector calibration, as standards for relative measurements, and as a possible input to the fundamental constants. The highest energy that we have directly measured is 675 keV although an energy of 1.1 MeV has been obtained by summation. Over the next year we plan to extend our measurements above 1 MeV in order to ensure that accurate high energy measurements are possible using the present crystals and angle measuring techniques.

-
1. R. D. Deslattes, Proc. Int. School of Physics 'Enrico Fermi', Course 68 (1978).
 2. R. D. Deslattes, E. G. Kessler, Jr., W. C. Sauder, and A. Henins, *Annals of Physics* (to be published).
 3. E. G. Kessler, Jr., R. D. Deslattes, A. Henins, and W. C. Sauder, *Phys. Rev. Lett.* 40, 171 (1978).
 4. E. G. Kessler, Jr., L. Jacobs, W. Schwitz, and R. D. Deslattes, *Nucl. Instr. and Meth.* 160, 435 (1979).
 5. E. G. Kessler, Jr., R. D. Deslattes, and A. Henins, *Phys. Rev. A* 19, 215 (1979).

6. W. C. Sauder and R. D. Deslattes, *Jour. Res. NBS* 71A, 347 (1967).
7. R. D. Deslattes, E. G. Kessler, Jr., L. Jacobs, and W. Schwitz, *Phys. Lett.* 71A, 411 (1979).
8. K-N. Huang, M. Aoyagi, M. H. Chen, B. Crasemann, and H. Mark, *At. Data Nucl. Data Tables* 18, 243 (1976).
9. G. K. Lum and C. E. Wiegand, *Bull. Am. Phys. Soc.* 23, 64 (1978).

MASS ASSAY OF STANDARD DEPOSITS

D. M. Gilliam and W. E. Slater
(Nuclear Radiation Division)

The NBS collection of fissionable deposits includes four fissile isotopes: U-235, Pu-239, U-233, and Pu-241. An archive deposit with mass in the 10- to 300- microgram range is maintained for each isotope. For both U-235 and Pu-239, the standard deposit mass has been determined to an accuracy of $\pm 0.5\%$, or better, by two independent techniques: isotope dilution mass spectrometry (IDMS) and absolute alpha counting. However, for the Pu-241 and U-233 deposits, no IDMS analysis is yet available to confirm the alpha assay. A second assay path for Pu-241 and U-233 was needed, and the path of comparison to the more accurately known U-235 and Pu-239 deposits in a monoenergetic thermal neutron beam was selected.

A 35-meV beam from a crystal spectrometer--filtered by oriented graphite to exclude the $\lambda/2$ impurity--was chosen for the comparison. ENDF/B-V cross sections were used for conversion of fission rate ratios to mass ratios. The results are tabulated in the table.

Principal isotope and deposit label	Mass by alpha assay (micrograms of principal isotope)	Mass by fission ratio at 35 meV to ^{235}U standard (micrograms of principal isotope)	Mass by fission ratio at 35 meV to ^{239}Pu standard (micrograms of principal isotope)
^{233}U 23-1-1	119.5 \pm 1.0%	119.9	118.8
^{241}Pu 41K-03-1(L)	8.96 \pm 3.0%	8.84	8.76

REACTOR FILTERED BEAMS

Robert B. Schwartz

(Nuclear Radiation Division)

Neutron response as a function of energy was determined for the neutron personnel dosimeters used at the Battelle Pacific Northwest Laboratory and at Argonne National Laboratory. The measurements were made using the thermal, 2 keV, 24 keV, and 144 keV beams at the NBS reactor, and with the Cf-252 spontaneous fission source. These measurements will allow the dosimeter readings to be interpreted properly once the neutron spectrum in the working environment is known.

USE OF THE THERMAL COLUMN AT THE NBS REACTOR TO DETERMINE THE EFFECTIVE MASS OF U-235 IN A MINIATURE FISSION CHAMBER

E. D. Mc Garry

(Nuclear Radiation Division)

In support of the Light Water Reactor (LWR) Pressure Vessel Surveillance Dosimetry Improvement Program,* absolute core-power measurements were made in a research reactor** at the Oak Ridge National Laboratory (ORNL). The reactor power was deduced from extensive measurements of the fission rate of U-235 in a miniature fission chamber that was inserted down between the fuel plates in the core. The reactor power measurements were a cooperative effort of ORNL, NBS and the CEN/SCK Laboratory in Mol, Belgium. The NBS function was to provide a measurement of the amount of U-235 in the fission chamber.

(*) The U.S. Nuclear Regulatory Commission's LWR-PV Surveillance Dosimetry Improvement Program administered for the NRC Metallurgy and Materials Research Branch by the Westinghouse-Hanford Engineering Development Laboratory, Richland, Washington.

(**) The subject reactor is the Pool Critical Assembly (PCA) located in the canal of the Bulk Shielding Reactor (BSR) at ORNL.

NON-RRD PROGRAMS

The method used to deduce the mass of U-235 in the miniature chamber was to compare its fission rate in a neutron field with that of another chamber containing a known mass of U-235. The neutron field chosen for this investigation was that in a 30-cm cavity within the graphite thermal column of the NBS reactor. (See figure 1.) The following paragraphs discuss why the mass sought is an effective mass rather than the true absolute mass of U-235 in the miniature chamber.

First, the two chambers have different geometries. The miniature chamber, used for the power measurements, is a high-pressure, ionization chamber containing a few micrograms of U-235 in a cylindrical geometry 1.5 mm in diameter, 10 mm in sensitive length and 1.2 m in overall length. The NBS chamber is a dual, parallel-plate type ionization chamber which can accomodate two light, 1.25 cm-diameter deposits of fissionable material on thin (5-mil thick), back-to-back discs of platinum or other suitable materials. The NBS chamber is shown in figure 2 and described in detail in reference 1. Because of the big difference in size, the possible perturbation of the flux by the NBS chamber was examined in detail. The effect of field gradients on repositioning, or the relative positions, of the chambers was also examined.

The effects of relative spatial locations, as well as chamber perturbations, were investigated with a mockup of the NBS chamber through and around which the miniature CEN/SCK could be positioned. Table 2 shows where measurements were taken and figure 4 shows the results. The perturbation at the CEN/SCK chamber, because of the presence of the NBS chamber, is approximately 2% and of the same magnitude whether the smaller chamber is inside of or along side of the NBS chamber. Therefore, a measurement configuration was then chosen with the CEN/SCK chamber beside the NBS chamber so that the perturbation at the smaller chamber was the same as at the center of the mockup. This means the perturbation is the same as that at the NBS deposits in the real chamber. The chamber perturbation therefore cancels from the fissionrate ratio measurements to within $\pm 0.3\%$ uncertainty.

However, the flux perturbation issue is more complex because there is also a flux perturbation by the 5-mil platinum backing on each deposit, none of which were included in the mockup chamber. Only one deposit on platinum was used for the fission-rate comparison measurements. The perturbation because of this backing was estimated analytically to be $2.5 \pm 1.5\%$ and the ratios must be adjusted for this perturbation.

Also, there is an unmeasurable perturbation by the nominal 10-mil steel walls of the CEN/SCK chamber. However, this perturbation is common to both the measurements in the NBS thermal column and to the reactor power measurements at ORNL, at least insofar as the neutron spectra are similar. Because the perturbation is small, on the order of $\pm 2\%$, it has been assumed that to $\pm 0.5\%$ it cancels from both NBS and ORNL measurements. This perturbation is, therefore, implicitly included in the effective mass of U-235 in the miniature chamber.

The last reason for measuring an effective mass is related to the shape of the voltage pulse-height distribution from the fission chamber. Figure 3 shows this distribution in the NBS chamber for two different deposit thicknesses. When the "valley" between the noise and the bulk of the distribution is well defined, and the peak-to-valley ratio is large, essentially all fission events can be counted because their pulse heights exceed a discriminator set anywhere in the valley. When the valley is not well defined, the fraction of true fissions counted is a function of the discriminator setting. This is the situation with the miniature chamber so its relative effective mass is a function of the discriminator setting. (See figure 5.) This effect produces less than $\pm 0.2\%$ uncertainty in the effective mass determination.

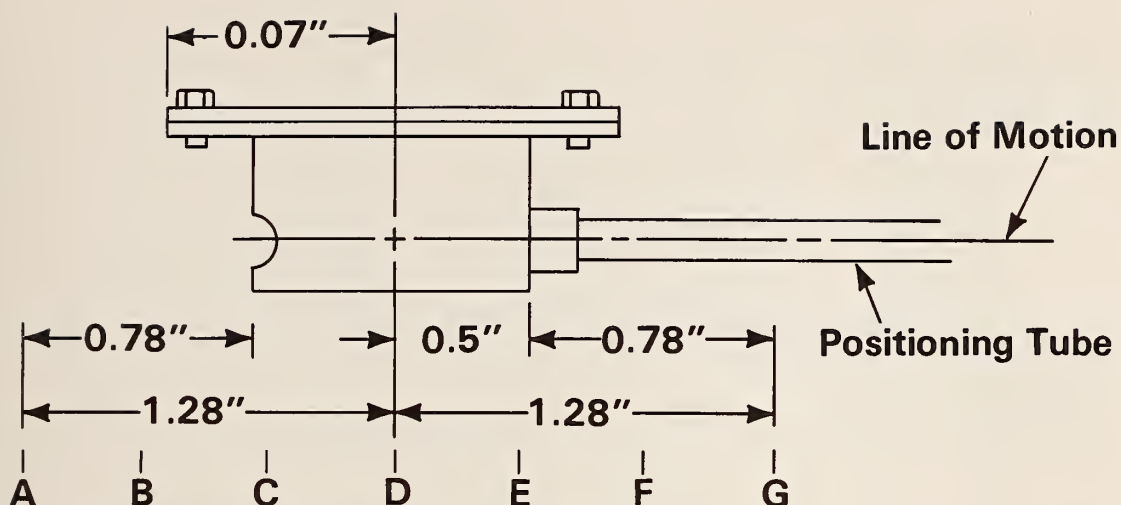
Final results of the measurements are summarized in table I and the paragraph following the table.

Table 1. Fission rate ratio between a 31.2 microgram NBS U-235 deposit and CEN/SCK fission chamber No. 1879

Number of Measurements	Observed & Dead-Time Corrected Fission Rate Ratio Above the Preferred Discriminator Setting ¹	Extrapolation-to-Zero Correction ² for the NBS Fission Chamber	NON-RRD PROGRAMS	
			Ratio: NBS Observed Fission Rate Divided by CEN/SCK Relative Fission Rate	
10	6.441 ± 0.0095	1.0038 ± 0.0002	6.465 ± 0.05%	
10	6.403 ± 0.0073	1.0038 ± 0.0002	6.427 ± 0.11%	
6	6.415 ± 0.0092	1.0038 ± 0.0003	6.439 ± 0.14%	
			Average:	6.444 ± 0.17%

¹Discriminators for both the NBS and CEN/SCK fission chambers are set at a fraction 0.54 of the peak of the pulse-height distribution.

²This correction adjusts the observed fission rate of the NBS fission chamber for that fraction of the fission-product pulse-height distribution which falls below the discriminator level.



**Positions at which CEN/SCK
Chamber measurements were made.**

Table 2. Mockup of the NBS fission chamber with a through hole for the CEN/SCK miniature cylindrical fission chamber.

Positions at which CEN/SCK chamber measurements were made

- A. Full in Position . . . The tip of the CEN/SCK chamber at this point is $1 \frac{1}{4}$ " beyond the front edge of the NBS dummy chamber.
- B. 1st Half Way Point . . . Tip is $\frac{1}{2}$ way between A & C.
- C. Front Edge . . . Tip is flush with front edge of NBS dummy chamber.
- D. Middle . . . Tip is really $\frac{1}{2}$ way between the front- and back-edge positions, which should mean tip is in middle of chamber.
- E. Back Edge . . . Tip of CEN/SCK chamber is flush with end of positioning tube.
- F. 2nd Half Way Point . . . Tip is $\frac{1}{2}$ way between positions E & G.
- G. Full Out Position . . . Tip is inside positioning tube $1 \frac{1}{4}$ " behind back edge of dummy chamber.

*Note: It is estimated from handling experience that CEN/SCK chamber can be repositioned at a point in the cavity to ± 2.5 mm.

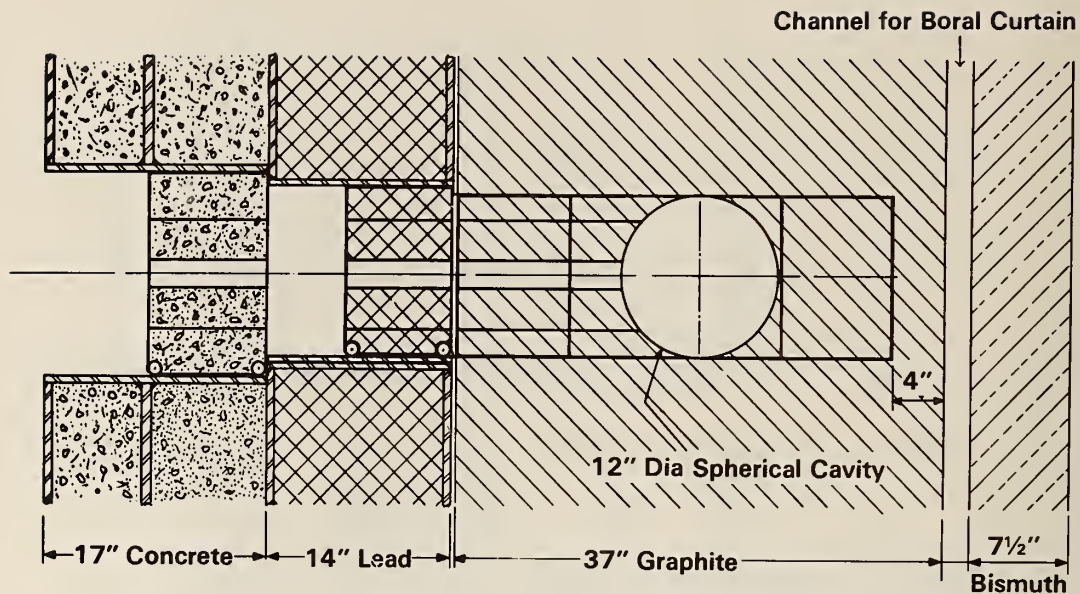


Figure 1. Plan view of a 30-cm cavity in the graphite of the thermal column of the NBS reactor. The cavity, when empty as shown, provides a region of isotropic thermal flux for miscellaneous irradiations and flux to drive two U-235 fission sources, positioned at the opposite ends of a cadmium pill box, for irradiations in a U-235 fission spectrum. The cavity may also be loaded with a B-10 shell inside of which exists the Intermediate-energy Standard Neutron Field (ISNF), a standard fast reactor type of spectrum.



Figure 2. NBS fission chamber which normally contains two back-to-back fissionable deposits on 5-mil thick steel backings. For the subject measurements only one deposit was in the chamber. This reduced the amount of thermal flux depression in the vicinity of the deposit.

NON-RRD PROGRAMS

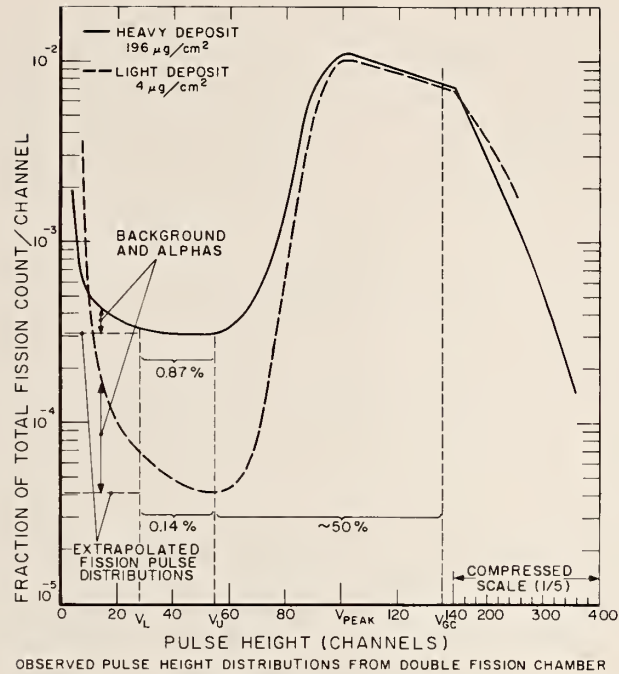


Figure 3. Observed pulse height distributions from double fission chamber.

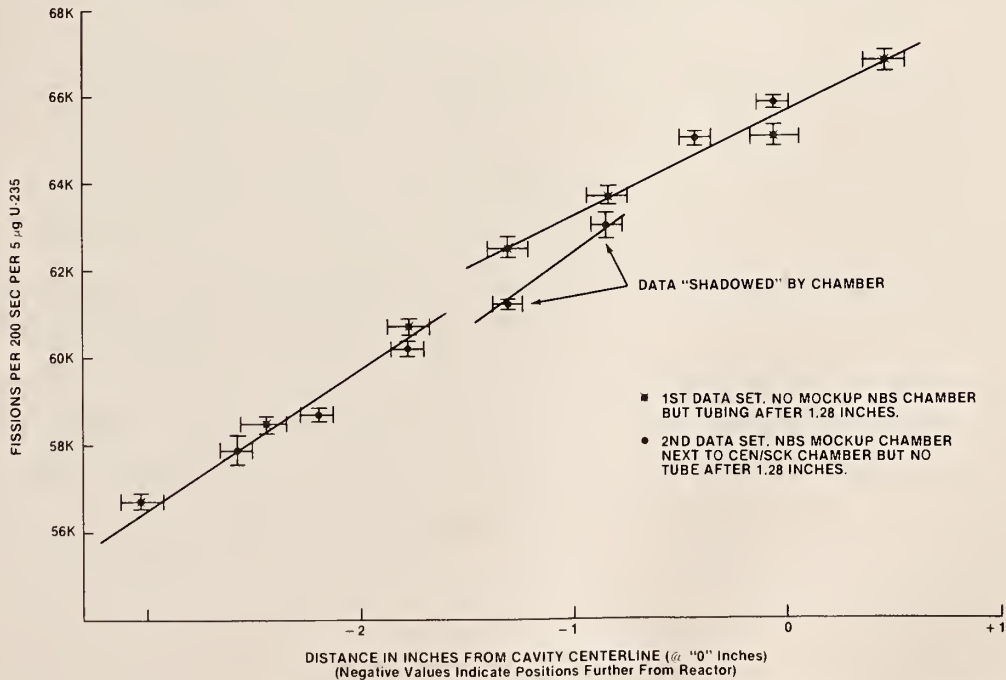


Figure 4. U-235 fissions in NBS 30-cm spherical, thermal column cavity with curtain down.

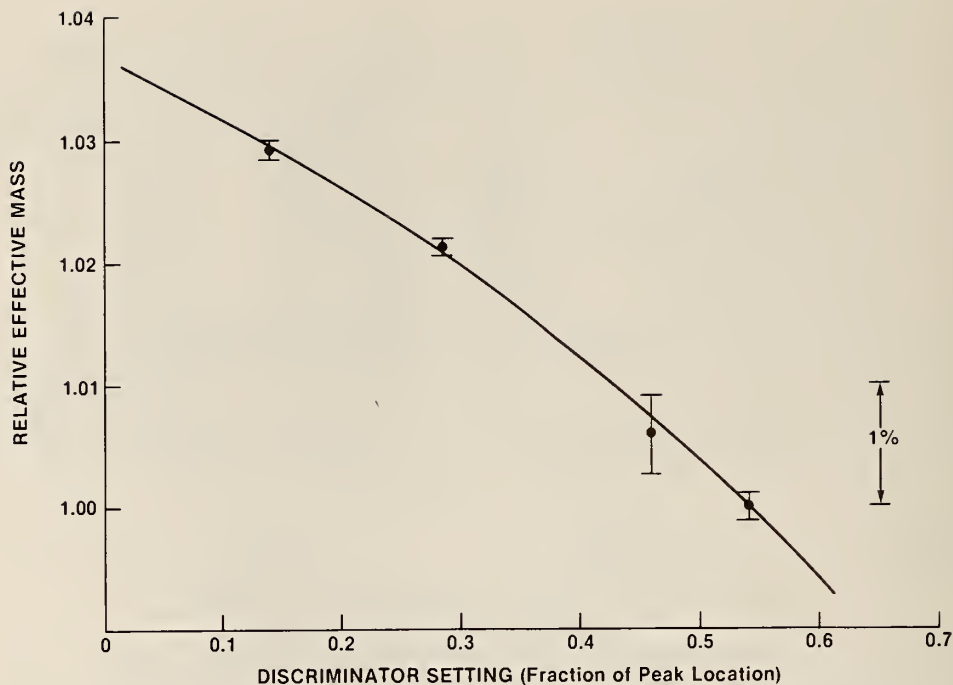


Figure 5. Effective U-235 mass versus discriminator setting for CEN/SCK fission chamber #1879.

The average value in table I, $6.444 \pm 0.17\%$, must be corrected for fission fragment absorption in the $31.2 \mu\text{g}$ NBS deposit and in the nominal $4.7 \mu\text{g}$ CEN/SCK deposit. The correction factor is $1.001172/1.00043 = 1.00129 \pm 0.00032$. As mentioned, the ratio also has to increase by $2.5\% \pm 1.5\%$ because of perturbation in platinum in the NBS chamber. The resulting ratio is 6.614. To the statistical uncertainties of 0.17%, and 1.5% systematic uncertainties $\pm 0.5\%$ must be added to account for possible non-cancellation of the previously described perturbation effects. There is also the additional 0.2% uncertainty associated with the discriminator settings. Because of the nature of these various uncertainties, they tend to add in quadrature and the final ratio is $6.614 \pm 1.6\%$.

NON-RRD PROGRAMS

Based upon a measured consensus mass of the NBS fission deposit (No. 25A-03-1) of 31.22 micrograms \pm 1.4%, the effective mass of the CEN/SCK miniature fission chamber used for absolute PCA core-powder measurements is:

$$\frac{31.22 \pm 1.4\%}{6.614 \pm 1.6\%} = 4.72 \pm 2.1\% \text{ micrograms U-235}$$

The associated discriminator setting for this result is 0.54 of the maximum of the pulse height distribution.

-
1. J. A. Grundl and D. M. Gilliam (NBS), N. D. Dudey and R. J. Popek (ANL) "Measurement of Absolute Fission Rates", *Nuclear Technology* 25, 237 (February 1975).

DYNAMIC SCATTERING FROM POLYMER SOLUTIONS

A. Z. Akcasu and M. Bermounz
(University of Michigan, Ann Arbor, MI)

and

C. C. Han
Polymer Science and Standards Division

Quasi-elastic neutron and light scattering experiments on polymer solutions have been used increasingly in recent years to study polymer solution dynamics¹. In these experiments one measures the intermediate scattering function $S(q, t)$ as a function of time t for different values of the momentum transfer, q . The measurement of $S(q, t)$ directly by neutron scattering has been possible only very recently with the application of the spin-echo technique².

Interpretation of such scattering experiments requires, ideally, a theory that can predict $S(q, t)$ as a function of t and q under actual experimental conditions, which are characterized by the temperature and

concentration of the solution, and by a chain model consistent with the chemical structure of the polymer. Unfortunately, exact expression of $S(q,t)$ is available, at present, only for a single unperturbed (0-condition) Gaussian chain without hydrodynamic interaction (Rouse model), and in the infinite chain limit, with hydrodynamic interaction and pre-averaged Oseen tensor (Rouse Zimm model). In this sense, a complete interpretation of dynamic scattering experiments on polymer solutions is an unsolved problem.

Some progress has been possible via knowledge of the asymptotic behaviour of $S(q,t)$ for large and small times, and in certain ranges of q -values. It is known that $S(q,t)$ decays exponentially after large times with a decay constant, Dq^2 where D is the diffusion coefficient of the polymer as a whole. Hence, D is determined readily by fitting an exponential function to $S(q,t)$ -data for sufficiently large t . This procedure is workable only when $qR_g \ll 1$, where R_g is the radius of gyration of the polymer. When this condition is not satisfied $S(q,t)$ decays below the noise level before the asymptotic exponential behaviour is reached. This is due to the contribution of the internal modes to the relaxation of $S(q,t)$ during the experiment. One may extend the q -range of the above procedure to larger q -values by representing $S(q,t)$ as superposition of two exponentials to take into account the effect of the most slowly decaying internal mode, as suggested by Pecora^{3,4}. However, one finds that the range of q -values and the time interval in which only the first internal mode is important are very narrow, as we have demonstrated. The effect of the internal modes during the experiment becomes important all at once when $R_{q=2-3}$ and thus makes the measurement of the decay constant of the first internal mode very inaccurate, if not impossible.

In the intermediate q -region defined by $qR_a \gg 1$ and $qa \ll 1$, where a is the statistical segment length, the relaxation of $S(q,t)$ is determined by all the internal modes collectively. Using an unperturbed single

gaussian chain model, de Gennes⁵, and Dubois-Voilette and de Gennes⁶ showed that $S(q, t)$ can be expressed as a function of a single variable $t = \Omega(q)t$ in the double limit of $qa \rightarrow 0$ and $qR_g \rightarrow \infty$. They referred to the scaling factor, $\Omega(q)$, as "characteristic frequency", and found that $\Omega(q) \sim q^3$ in the Zimm limit. This property of $S(q, t)$ has been used to interpret scattering experiments^{2,7} in the intermediate q -region by fitting the shape function, calculated for the unperturbed Gaussian chain, to $S(q, t)$ -data, obtaining $\Omega(q)$ as function of q , and representing $\Omega(q)$ by a power law q^a to see whether the exponent a deviates from the theoretical value 3. One difficulty with this procedure is that the conditions $qa \ll 1$ and $qR_g \gg 1$ are usually not strictly satisfied in an experiment. In the small- and large- q ends of this interval, the molecular and segmental diffusion effects, respectively, become increasingly important. In addition, $S(q, t)$ displays, as a function of time, a cross over from Rouse-like behaviour to Zimm-like behavior at a finite time. This cross over time is inversely proportional to $[(\xi_0/\eta_0 a)/qa]^4$ where $(\xi_0/\eta_0 a)$ is the draining parameter, ξ_0 is the friction coefficient per monomer, and η_0 is the viscosity of the solvent. Although the Zimm behavior is always reached asymptotically after sufficiently long times, it may not always be attained before $S(q, t)$ decays below the noise level during an experiment. One final difficulty with the above approach is that the characteristic frequency, obtained in an experiment in which the conditions $qa \ll 1$ and $qR_g \gg 1$ are not quite satisfied, does not have to obey strictly a simple q^3 -power law as predicted by the asymptotic theory.

In this paper we propose an alternative method for the interpretation of scattering experiments in terms of the initial slope $\Omega(q)$ of the normalized intermediate scattering function $\mathcal{S}(q, t) \equiv S(q, t)/S(q, 0)$, and a q -dependent shape function $f(t, q)$. The initial slope is defined by:

$$\Omega(q) \equiv -\lim_{t \rightarrow 0} d\mathcal{S}(q, t)/dt \quad (1)$$

The short times involved in this definition are larger than the memory times of the solvent. We anticipate that the dynamics of the chain will be governed by a diffusion equation in which the solvent effects are averaged out.

The shape function is introduced through:

$$\phi(q, t) \equiv \exp[f(\Omega t, q)]$$

Clearly, $f(0, q) = 0$ and

$$\left. \frac{df(t, q)}{dt} \right|_{t=0} = -1.$$

In the small- and large- q limits, $f(t, q)$ behaves as $f(t, q) \sim t$, since $\phi(q, t)$ decays exponentially in these q -ranges. In the mathematical limit of $q \rightarrow 0$ and $qR_g \rightarrow \infty$, it becomes a function of t only, and Ω coincides with the characteristic frequency introduced by Dubois-Violette and de Gennes.

One of the merits of the present approach is that the initial slope $\Omega(q)$ is calculable for all values of q as a function of temperature and concentration, in terms of the "blob" model of chain statistics^{8,9}. Thus, in an experiment, one is no longer restricted only to narrow asymptotic q -regions and dilute solutions at θ -condition. The main difficulty with this method, however, is that the initial slope is hard to measure in the intermediate q -range. We avoid this difficulty by providing the shape function $f(t, q)$ as a function of t for several values of q in this as well as other q -regions, and for a few values of the draining parameter $(\xi_0/\eta_0\alpha)$. By comparing these theoretical shape functions with the experimental $\ln \phi(q, t)$ one can determine simultaneously both the initial slope $\Omega(q)$ and the statistical segment length α , or the radius of gyration, R_g , depending on the range of q -values involved. The experimental $\Omega(q)$ can thus be compared with its theoretical expression that includes concentration and temperature effects. The tacit assumption in this procedure, as well as those used earlier, is that the shape function is less sensitive to temperature and concentration effects

than the initial slope, so that it can be approximated by its expression for a single Gaussian chain in O -condition.

In Reference 10, we have obtained theoretically various formulations of the scattering function $S(q, t)$. We have calculated the exact expressions of $S(q, t)$ for simple chain models. We also calculated directly the initial slope $\Omega(q)$ for various chain models and experimental conditions. Finally we explained a procedure the the interpretation of both neutron and light scattering experiments using the above mentioned results, with application to real light scattering data on polystyrene in toluene.

-
1. For example: (a) Chu, B. "Laser Scattering", *Academic Press*, (1974); (b) "Photon Correlation and Light Beating Spectroscopy", (Ed. H. Z. Cummins and E. R. Pike), *Plenum Press*, (1974; (c) Berne, B. J. and Pecora, R. "Dynamic Light Scattering", Wiley, (1976).
 2. Richter, D. *et al*, *Phys. Rev. Lett.* 1978, 41, 1484.
 3. Pecora, R. J. *Chem. Phys.* 1965, 43, 1562.
 4. Pecora, R. J. *Chem. Phys.* 1968, 49, 1032.
 5. de Gennes, P. G. *Physics*, 1967, 3, 37.
 6. Dubois-Voilette, F and de Gennes, P. G. *Physics*, 1967, 3, 181.
 7. Adam, M. and Delsamo, M. *Macromolecules*, 1977, 10, 1229.
 8. Daoud, M. *Thesis*, Universite de Paris 1977.
 9. Larnous, B. *et al*, *Physics*, 1978, 39, 77
 10. Akcasu, A. Z., Benmouna, M. and Han, C. C., *Polymer* (in press).

SMALL-ANGLE NEUTRON SCATTERING ON ATACTIC POLYSTYRENE WITH HIGH LABELED CHAIN CONCENTRATION

S. J. Bai

(Reactor Radiation Division/University of Michigan)

and

Charles C. Han and David J. Lohse

(Polymer Science and Standards Division)

The application of small-angle neutron scattering (SANS) to polymer systems has been following the approach of light and x-ray scattering. In the determination of single molecular chain behavior, low labeling chain concentration is usually required to minimize the contribution due to multi-chain interference. Recently, it has been pointed out^{1,2} that because of the uniqueness of isotope labeling technique multi-chain interference can be accounted for and subtracted from the neutron measurement. Thus, high concentration of labeled chain can be used for SANS investigation provided the labeled chain and the un-labeled chain can be treated as identical except their scattering lengths.

For bulk atactic polystyrene (PS), the coherent elastic differential cross section reduces to³

$$S(Q) = C(1-C)(b_H - b_D)^2 S_s(Q) + [Cb_D + (1-C)b_H]^2 S_T(Q) \quad (1)$$

where C is the labeled chain concentration, b_H and b_D are the scattering lengths of hydrogenated PS (PSH) and deuterated PS (PSD) monomers, respectively. $S_s(Q)$ is the single chain form factor.

$$S_s(Q) \equiv \left(\sum_{\substack{j,j' \\ k,k'}} \delta_{j,k} e^{iQ \cdot (\underline{R}_j + \underline{\Gamma}_{j'} - \underline{R}_k - \underline{\Gamma}_{k'})} \right) \quad (2)$$

$S_T(Q)$ is the total form factor of the whole system.

$$S_T(Q) \equiv \left(\sum_{\substack{j,j' \\ k,k'}} e^{iQ \cdot (\underline{R}_j + \underline{\Gamma}_{j'} - \underline{R}_k - \underline{\Gamma}_{k'})} \right) \quad (3)$$

where \underline{R}_i is the C.M. position of the i -th chain, and $\underline{\Gamma}_i$ is the position of the i' -th monomer of the i -th chain relative to \underline{R}_i . The bracket

denotes an ensemble average over all accessible states of the system. It is shown in Eq. (1) that two bulk PS samples with different labeled chain concentration would generally be sufficient to obtain $S_s(Q)$ from their coherent scattering intensities.

For all molecular chain configurations, $S_s(Q)$ can be approximated in the low-Q region by

$$S_s(Q)^{-1} \sim \left(1 + \frac{Q^2 R_g^2}{3}\right) \quad (4)$$

where R_g is the radius of gyration of the molecular chain. The slope of $S_s(Q)^{-1}$ versus Q^2 reveals R_g which used to understand the distribution of the chain configuration. For polymer chains in a θ -solution, the molecular chains assume a random distribution with a simple relation between the molecular shape and the molecular weight. This relation is

$$R_g \sim Mw^{0.5} \quad (5)$$

where Mw is the molecular weight of the polymer.

In our experiment, PSH and PSD of approximately matched molecular weights of 9500 and 32,000 were used. The PS species were co-dissolved in p-xylene with PSD/PS ratio from zero to 0.30. The solvent was removed by freeze-drying. PS mixtures were then molded to become bulk samples close to 0.065 cm thick. Neutron measurements were performed on BT5(NBS) SANS spectrometer. The Q-region was extended from about 0.012\AA^{-1} to 0.097\AA^{-1} .

Figure 1 is an example of measured single chain form factor $S_s(Q)$ presented as $S_s^{-1}(Q)$ versus Q^2 . In this case, PSD/PS concentration C is 20 percent, and PS molecular weight Mw is 32,000. From the slope-intercept treatment of the low-Q region of figure 1 we obtain an R_g of 48\AA .

Our values of R_g are shown as open triangle (Δ) in figure 2, which is a collection of SANS on PS results. Symbols correspond to θ -solution of PSD in cyclohexane at 36°C (+)⁶, bulk PS with low C (o)⁶, and bulk PS with high C (o)⁷.

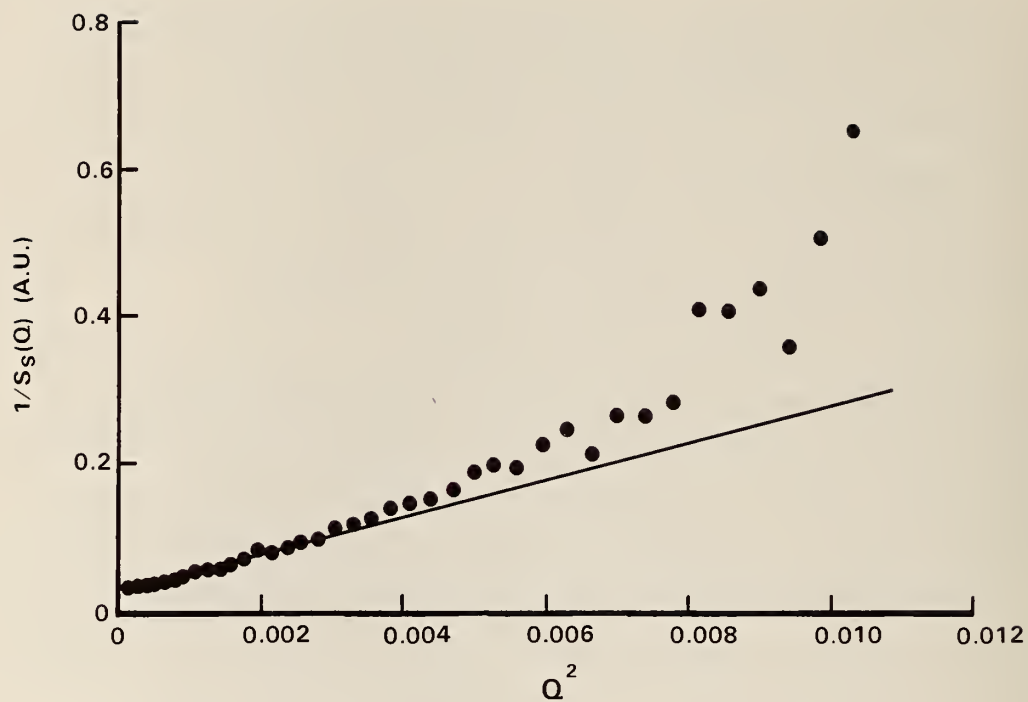


Figure 1.

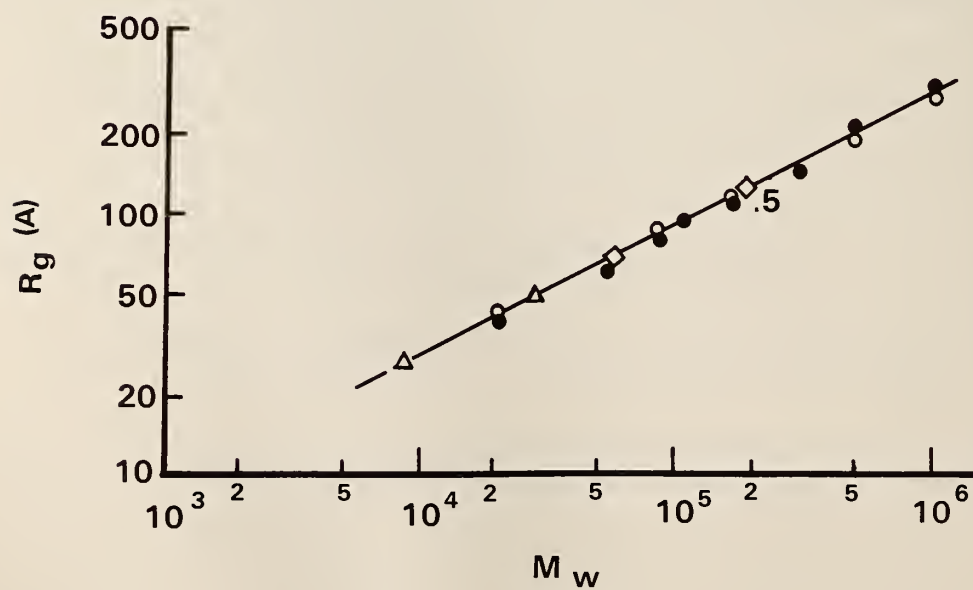


Figure 2.

It is evident from our results that small molecules, with contour length as small as 250\AA , of bulk PS still preserve a configuration with random distribution. Also the validity of the high labeled chain concentration approach is demonstrated when the labeled chain and the unlabeled chain can be identically treated and have similar molecular weight. This greatly facilitates SANS experiment which has been limited by the comparably small flux from all available neutron sources.

We are presently extending this study to PS-cyclohexane solutions in both dilute and semidilute regions. Our emphasis is centered on the question of chain expansion with finite concentration of " θ -temperature".

-
1. C. Williams et al., *J. Polym. Sci.: Polym. Lett. Ed.*, 17, 379 (1979).
 2. A. Akcasu et al., *J. Polym. Sci.: Polym. Phys. Ed.*, 18 (1980).
 3. G. C. Summerfield, J. S. King, and R. Ullman, *J. Appl. Cryst.*, 11, 548, (1978).
 4. P. Debye, *J. Phys. Chem.*, 51, 18 (1947).
 5. P. Flory and J. Rehner, *J. Chem. Phys.*, 11, 512 (1943).
 6. J. P. Cotton et al., *Macromolecules*, 7, 863 (1974).
 7. J. S. King et al., (to be published).

EVALUATION OF NEUTRON SPECTRUM IN THE INTERMEDIATE-ENERGY
STANDARD NEUTRON FIELDJ. Grundl and C. Eisenhauer
(Nuclear Radiation Division)

Specification of the neutron spectrum for the Intermediate-Energy Standard Neutron Field (ISNF) was completed this year. Included are error bounds for the spectrum over its full energy range and also propagated uncertainties for most of the neutron reaction rates which have been or will be measured in the system. The spectrum evaluation was based on an exhaustive study of the spectrum sensitivity to physical and nuclear parameters of the system and was backed up by density and chemical impurity determinations and neutron beam transmission measurements. Table 1 shows the effect on the ISNF spectrum of variations in the important physical parameters of the system. Ratios of the perturbed spectrum to the standard ISNF spectrum are given in 14 energy groups for the indicated variation in each parameter. Correlations of the spectrum changes associated with the parameter uncertainties showed an unexpected pattern of errors for the neutron reaction rates. Table 2 shows the effect of variations in the physical parameters on the calculated reaction rates in ISNF. Variations in the scattering properties of carbon, which would be expected to have effects at low energies, produce significant variations in threshold reaction rates such as U-238 (n,f). Typical reaction rate errors attributable to ISNF spectrum uncertainties are in the range $\pm 0.5\%$ to $\pm 1.4\%$ exclusive of fission spectrum uncertainties; with fission spectrum uncertainties included the errors are $\pm 0.6\%$ to $\pm 2.5\%$.

Table 1. Spectrum variation for ISNF parameter uncertainties

Lower Energy Boundary	Group Flux	¹⁰ B Absorption $\delta(\rho\sigma)_0 = +2\%$	Graphite Mean- Free-Path $\delta(1/\rho\sigma)_0 = -2\%$	Aluminum Scatter $\delta(\rho\sigma)_0 = +10\%$	Source Radius $\Delta r = -1\text{mm}$	Carbon Scatter P_2/P_3
0.414 eV		0.943	1.009	0.998	0.996	0.985
0.454 keV		0.967	1.009	0.999	0.996	0.987
1.234		0.980	1.008	1.000	0.996	0.991
3.355		0.988	1.008	1.000	0.996	0.994
9.12		0.993	1.007	1.001	0.996	0.996
24.8		0.997	1.005	0.996	0.996	0.998
67.4		0.999	1.003	0.999	0.996	0.999
111		1.001	1.003	1.000	0.997	1.000
183		1.0015	1.001	1.001	9.998	1.003
498		1.0025	0.999	1.001	1.000	1.005
1.353 MeV		1.0025	0.997	1.000	1.003	1.002
2.231		1.0025	0.995	0.999	1.006	0.989
3.679		1.0025	0.994	0.998	1.008	0.993
6.065-17		1.003	0.993	0.998	1.010	0.997

Factor listed is ratio of group flux for ISNF calculation with parameter changed as indicated to group flux without parameter change.

Table 2. (a) Cross section changes associated with individual ISNF parameter uncertainties

NON-RRD PROGRAMS									
Reaction	E ₉₅	E ₅₀	Boron-10 Absorption	Graphite Mean-Free- Path	Carbon Scatter	Aluminum Scatter	Source Radius	Total Error (rms sum)	
<u>Fission</u>									
²³⁵ U(n, f)	0.8 keV	0.24	- 0.5%	+ 0.2%	- 0.2%	< 0.1%	- 0.1%	± 0.6%	
Np(n, f)	0.5 MeV	1.5	+ 0.2%	- 0.3%	0.0%	< 0.1%	+ 0.3%	± 0.5%	
²³⁸ U(n, f)	1.4 MeV	2.3	+ 0.2%	- 0.6%	- 0.5%	+ 0.1%	+ 0.5%	± 1.0%	
<u>Capture</u>									
²³⁸ U(n, γ)	0.3	21	- 1.2%	+ 0.4%	- 0.4%	+ 0.1%	- 0.25%	± 1.4%	
Na(n, γ)	1.7	2.9	- 1.4%	+ 0.6%	- 0.6%	+ 0.25%	- 0.4%	± 1.7%	
Au(n, γ)	0.33	5	- 1.6%	+ 0.6%	- 0.6%	+ 0.15%	- 0.3%	± 1.8%	
<u>Threshold</u>									
In(n, n')	1.0	2.3	+ 0.2%	- 0.4%	- 0.4%	+ 0.2%	+ 0.5%	± 0.8%	
⁵⁸ Ni(n, p)	1.8	3.7	+ 0.2%	- 0.6%	- 0.8%	+ 0.4%	+ 0.7%	± 1.3%	
⁴⁸ Ti(n, p)	5.7	8	+ 0.2%	- 0.6%	- 0.3%	+ 0.6%	+ 1.0%	± 1.4%	

(a) Parameter uncertainties are listed in Table 1.

D. REACTOR OPERATIONS AND SERVICES

Shortly after the beginning of this reporting year, a mechanical problem which developed with one of the shim arms forced an extended reactor shutdown of nearly seven months. The problem was finally traced to a swelling of the cadmium blade which necessitated replacement of all four blades. The replacement process, which had never been done before, proved to be both difficult and complex because everything had to be done remotely due to the highly radioactive components and environment involved. In addition, a great deal of preparation had to be made including preparation of methods and procedures, design and construction of heavy shield cask, design and fabrication of tools and equipment, and fabrication of critical replacement parts.

The old shim arms were the original installed in the reactor during construction more than 12 years before. They had already lasted significantly longer than expected due to a very effective fuel management program. The blades had approximately two more years lifetime and were scheduled for replacement in 1981 during the conversion to 20 MW. The shim arm replacement operations were performed entirely in-house. They were carried out smoothly and efficiently and with absolute safety. There was little or no exposure to personnel.

During this period several other major tasks were undertaken. They included inspection of the reactor internal piping and overhaul of the fuel transfer system. A new fuel element design was installed in the reactor that will provide even greater fuel utilization efficiency, already one of the best in the country. Significant progress was made towards reactor modernization including procurement of a new cooling tower and design of all new or modified systems.

1. Reactor Operations

Reactor operating schedule was curtailed last year due to the replacement of the shim arms. Most of the effort of operations and

REACTOR OPERATIONS AND SERVICES

engineering personnel was directed towards returning the reactor to normal as quickly as possible. A summary of overall statistics is presented in the following table for the period July 1, 1979 - June 30, 1980.

NBSR OPERATING SUMMARY FY 80

No. of days at 10 MW	122
On-line time at 10 MW	33%
Average U-235 burnup	50%
No. of Irradiations	1160
Hours of Irradiations	1600
Hours per Irradiation	1.4

2. Irradiation Services

During the short period the reactor operated last year there was perhaps the heaviest use of irradiation facilities in the history of the reactor. Activation Analysis continued on a large scale. Among these are analyses of foods, drugs, environmental samples, forensic investigation, development of energy resources and raw materials, and the production of important standard reference materials.

Among new programs that have been initiated are the establishment of a National Environmental Sample Bank and ultraprecise analysis of atmospheric samples from all over the world. Discussions are also underway with NIH, the National Naval Medical Center, and Johns Hopkins for the production of fluorine-18 in a pioneering program for direct study of functions of vital organs and human cells.

3. Engineering Services

Aside from the engineering support provided to reactor operations and experimenters, engineering services was heavily involved in three major areas. These are the successful resolution of the shim arm problem and subsequent replacement, reactor modernization, and procurement and inspection of new fuel elements for future reactor use.

The shim arm problem was probably one of the most demanding ever encountered in the operating history of the NBSR. Extensive engineering,

design, fabrication, machining, and procurement were required. Engineering services personnel were also involved in several aspects of the actual replacement and installation of components, all performed remotely under-water. The careful planning and conduct of all operations resulted in the smooth and efficient reassembly and reinsertion of the new assemblies into the reactor. These were perhaps the most crucial and potentially damaging operations of the entire project.

Production of the new fuel element design was started this year and the first batch of elements were inspected, accepted, and delivered in time for use in the reactor.

Significant progress was made towards the reactor modernization. The new cooling tower design was completed and a contract was awarded for construction in the summer of 1980. Similarly the cooling tower basin design was finalized and construction has already started. Design of the extensive secondary piping, relocation of pumps, and a new chemical treatment center was also completed. A portion of the new secondary system is already in place with the balance to be completed once the new cooling tower is installed. All electrical connections design and specifications were also finalized. A comprehensive design plan of new nuclear, process, and monitoring instrumentation has been prepared. Most of the components and equipment have been specified and obtained. These will be assembled, tested, and installed periodically whenever reactor shutdown permits.

E. SERVICE PROGRAMS

ACTIVATION ANALYSIS PROGRAM OF THE FOOD AND DRUG ADMINISTRATION AT THE NBSR

W. B. Stroube, Jr., W. C. Cunningham, and M. Allegrini^{*}
(Food and Drug Administration, Washington, DC)

Neutron Activation Analysis (NAA) work performed by the Food and Drug Administration (FDA) is conducted in the reactor building located at the NBS. NAA has been used by the FDA for trace metal analyses of materials such as foods, drugs, and plant and animal tissues. The NAA group conducts research projects, provides services (such as analyses of special samples, when required information cannot be obtained from FDA field labs) and participates in interlaboratory studies. Since data obtained by NAA is complementary to other analytical techniques, sustained interactions with other FDA groups occur. Examples of two projects performed within the past year by the NAA group are discussed below.

1. Analysis of Sewage Sludge

Municipal sewage sludges have increasingly been used as crop fertilizers. Since sewage sludge contains high levels of many elements which have either toxicological or nutritional significance, questions have been raised concerning the practice of allowing food animals to graze on cropland to which sewage sludge had previously been applied.

The Department of Animal Sciences at Colorado State University conducted a study on cattle which were fed a diet containing a substantial amount of sewage sludge. The purpose of this study was to determine whether the addition of the sludge to the diet caused the levels of certain metals to be altered in various tissues. The data obtained indicated that the levels of some elements were elevated in some tissues from cattle which had been fed the sludge.

Recently, the FDA Metals Group has combined the efforts of Inductively Coupled Plasma (ICP) and NAA to obtain information for many

^{*}FDA visiting scientist from Institute of Food Science, University of Pavia, via Taramellis-Pavia, Italy.

SERVICE PROGRAMS

additional elements in the cattle tissues. Liver, kidney, spleen, brain and muscle tissue samples (from both control and experimental cattle) were analyzed, as well as the control and amended diets, feces from the control and experimental cattle, and the undiluted sewage sludge.

Agreements between ICP and NAA data were very good. The data indicated that the levels of Pb and Cd in kidney and of Pb, Cd, and Cu in liver in the human consumption of these tissues to be of concern on a regular basis. Most elements, however, were not raised to high enough levels to cause alarm.¹

2. Determination of Iodine

The deficiency of dietary iodine has been shown to cause goiter. In recent years, however, there has been some indication that excessive iodine intake can contribute to thyroid disorders in susceptible individuals. While excessive iodine intake does not appear to be a problem elsewhere, recent reports show an increasing iodine consumption by the people of North America. Therefore, it is important to be able to monitor iodine levels with good accuracy and precision.

Radiochemical NAA is currently being used to determine the average daily iodine intake of Americans. This is being accomplished by analyzing food samples collected at many locations throughout the United States. Provisions are made for three age groups - infant (6 mo.), toddler (18 mo.) and adult. The iodine intake is being determined for each age group.

The analysis technique being used is a modification of the combustion and gas phase separation procedure reported by Rook.² Parameters in this procedure were modified to improve iodine recoveries and analytical precision from the sample matrices of this study. Parameters which were modified include the size of the hydrated manganese dioxide (HMD) trap, the quantity of iodine carrier, the oxygen flow and the heating temperature of the HMD trap.

The modified method was tested with ten different food composites in order to evaluate the matrix influence. Recoveries were found to be 95% with a 3% coefficient of variation, indicating that the separation

does not depend on the food matrix. The performance of the method has been tested using NBS standard reference materials without certified iodine values. The average concentrations and standard deviations (dry weight) found with five determinations each were: Spinach (SMR 1570) 1.325 ± 0.055 ug/g; Oysters (SMR 1566) 3.209 ± 0.134 ; Bovine Liver (SMR 1577) 0.249 ± 0.012 ug/g. All NBS reference materials were dried in an oven at 100°C 24 hr prior to analysis.

To date, approximately 200 composite food samples have been assayed. Since additional samples are being analyzed and the data obtained to date have not been fully studied, results are preliminary. The daily adult intake, based on the levels found in the composites and assuming a 3900 Kcal caloric intake, ranges between 268 and 1212 ug/day.

-
1. Kenneth W. Boyer, John W. Jones, Douglas Linscott, Steven K. Wright, William Stroube, and William Cunningham, manuscript submitted to *Journal of Toxicology and Environmental Health*, July 1980.
 2. H. L. Rook, *J. Radioanal. Chem.* 39, 351 (1977).

U.S.G.S. ACTIVATION ANALYSIS PROGRAM

P. A. Baedeker and J. W. Morgan
(U.S. Geological Survey, Reston, VA)

1. Instrumental Neutron Activation Analysis

a. The Geological Survey has an ongoing program of Automated INAA which provides data for 24 to 30 elements in 3000 to 4000 rock mineral and coal samples per year. The technique is applied to studies related to: 1) the characterization of tectonic setting; 2) magma chamber eruptive sequences; 3) trace element partitioning to study petrologic history; 4) mechanisms of ore deposition; 5) alteration studies; 6) the formation of Mn nodules and metal rich sediments; 7) the origin of coals and peats; 8) compilation of a baseline of coal compositions; and 9) trace element studies to assist other geologic and geochemical investigations. During the past year the Georgia Tech Research Reactor was used during the six month period that the NBS reactor was shut down. Epi-thermal irradiation using the JEEP-II reactor in Kjeller, Norway are used for the analysis of rocks with high Uranium and/or Phosphorous contents.

b. The INAA procedure is being applied to the analysis of microscopic metal grain from chondrite meteorites¹, and to characterize iron meteorites collected in Antarctica in association with the Smithsonian Museum of Natural History.

c. A review of computer methodology in the analysis of gamma-ray spectra² has recently been completed.

2. Radiochemical Neutron Activation

a. Group separations of rare earth elements (REE) U.S.G.S. standard rocks. The group separation method is being applied to U.S.G.S. standard rock in which REE abundances are near or below the limits of detection of our INAA procedure.

b. Mafic and ultramafic rocks and separated minerals.

We continue to supplement our INAA determinations by group separations in those materials where REE abundances are very low.

- c. Ultra trace determinations of siderophile and volatile elements in meteorites, and in lunar and terrestrial rocks

Separations. Our current suite of siderophile elements (Au, Ge, Ir, Ni, Os, Pd, Re) is being extended by including separation steps for Ru (distillation) and Pt (anion exchange).

Lunar green glasses. Mafic and ultramafic glass spheres found on the Moon tend to have surface-correlated enrichments of volatile and siderophile elements. Last year, we showed that the siderophile element pattern in Apollo 17 black and orange glasses resembled that of a II B iron meteorite.³ Currently we are studying the bulk content of these elements in surface etched Apollo 15 green glasses (in conjunction with Roman Schmitt of Oregon State University) and also plan to extend the study to unetched specimens.

Lunar and terrestrial ultramafic rocks. Our study of a suite of terrestrial ultramafic rocks is now complete^{4, 5} and we intend to accumulate a similar data set for the few lunar ultramafic rocks available.

Strangways Crater, Australia. A suite of samples of impact melts and country rocks from the Strangways crater have been analyzed for siderophile and some volatile elements. The significant enrichments of Ni in impact melts are accompanied by only small enhancements of Ir and Os, suggesting that the impacting object was not chondritic in composition. As shown for the Lonar crater⁶, there is evidence of loss of Re and Se by volatilization during the impact process. In order to establish precise compositional mixing models to relate melt rocks with parental country rocks, this suite of samples is also being studied by INAA.

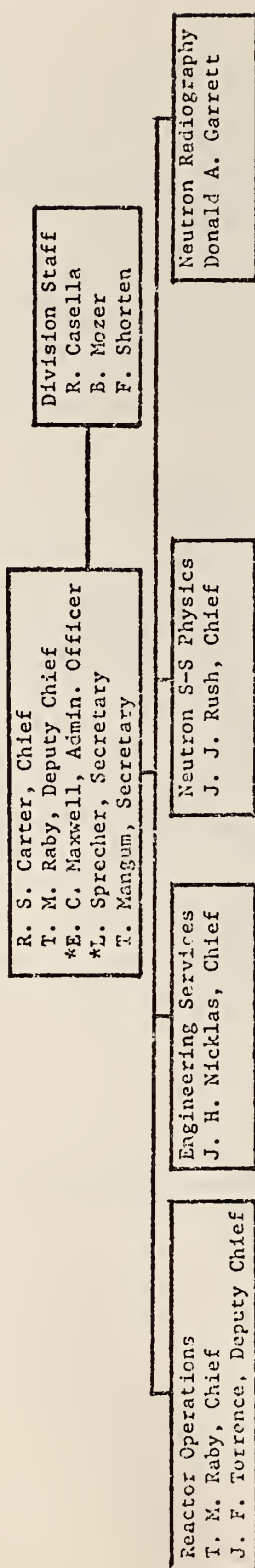
Antarctic iron meteorites. After INAA, the suite of 10 Antarctic irons will be analyzed for Pt metals, Au, Re, Ge, for further chemical characterization.

1. P. A. Baedeker, "Siderophile Element Fractionation in the Metal Phase of the Bruderheim Chondrite," *Lunar and Planetary Science XI, Part I*, 49-51 (1980).
2. P. A. Baedeker, "Comparisons of Peak-Search and Photopeak-Integration Methods in the Computer Analysis of Gamma-Ray Spectra," *Proceedings of the Fourth International Conference on Nuclear Methods in Environmental and Energy Research* (Univ. of Missouri, April 14-17, 1980) (in press).
3. J. W. Morgan and G. A. Wandless, (1979) "74001 Drive Tube: Siderophile Elements Match IIB Iron Meteorite Pattern," *Proc. Lunar Planet. Sci. Conf.* 10th p. 327-340.
4. J. W. Morgan, G. A. Wandless, R. K. Petrie, and A. J. Irving, (1980) "Composition of the Earth's Upper Mantle - I. Siderophile Trace Elements in Ultramafic Nodules." *Proc. Lunar Planet. Sci. Conf.* 11th, in press.
5. J. W. Morgan, G. A. Wandless, R. K. Petrie, and A. J. Irving, (1980) "Composition of the Earth's Upper Mantle - II. Volatile Trace Elements in Ultramafic Xenoliths." *Proc. Lunar Planet. Sci. Conf.* 11th, in press.
6. J. W. Morgan, (1978) "Lunar Crater Glasses and High-Magnesium Australites: Trace Element Volatilization and Meteoritic Contamination." *Proc. Lunar Planet. Sci. Conf.* 9th p. 2713-2730.
4. J. W. Morgan, G. A. Wandless, R. K. Petrie, and A. J. Irving, (1980) "Composition of the Earth's Upper Mantle - I. Siderophile Trace Elements in Ultramafic Nodules." *Tectonophysics*, in press.

F. PERSONNEL ROSTER

REACTOR RADIATION DIVISION

566



C. Freedman, Secretary

S. Long, Secretary

Reactor Operators

R. Beasley
M. Bell
N. Bickford
H. Brake
J. Browning
D. Cea
A. Chapman
H. Dilks
W. Mueller
J. Ring
R. Stiber
D. Wilkison
B. Young

*Part-time
+Intermittent
#Guest Worker

Mechanical Design

E. Guglielmo
J. Sturrock
Electronics
R. Conway
R. Hayes
L. Shuman

Crystallography

#C. Choi
D. Fravel (1/2)
E. Prince
W. Rymes (1/2)
A. Santoro
A. Tudgay (1/2)

Metal Hydrides and Molecular Materials

D. Fravel (1/2)
#A. Magerl
#H. Prask
J. Rowe (1/2)
W. Rymes (1/2)
#S. Trevino

Magnetic and Amorphous Materials

#H. Alperin
K. Hardman (Post Doc.)
#N. Koon
+J. Lynn
J. Rhyné
A. Tudgay (1/2)
#R. Williams

Advanced Neutron Methods

N. Berk
S. Bai, IPA
C. Glinka
J. Rowe (1/2)
S. Singhal, IPA

Reactor Operators

R. Beasley
M. Bell
N. Bickford
H. Brake
J. Browning
D. Cea
A. Chapman
H. Dilks
W. Mueller
J. Ring
R. Stiber
D. Wilkison
B. Young

*Part-time
+Intermittent
#Guest Worker

STAFF ROSTER

NON-RRD NBS STAFF LOCATED AT REACTOR

Division 354

P. Cassidy
K. Eggert
D. Hoaney
T. Hobbs
F. Moore
J. Shubiak

Division 532

M. Baier
R. A. Dallatore
C. Eisenhower
D. Gilliam
J. A. Grundl
E. McGarry
I. G. Schroder
R. Schwartz
W. Slater
V. Spiegel

Division 501

H. Berger

Division 506

D. Becker

Division 551

J. Bailey
M. J. Blackman
B. Carpenter
R. Fleming
T. Gills
S. Harrison
J. Koskoris
R. Lindstrom
G. Lutz
J. Mitchell
T. Mitlehner
L. Pilione
M. Vinocur
R. Zeisler

GUEST WORKERS AND COLLABORATORS

Division 520

A. Henins
L. Jacobs
E. Kessler
W. Sauder
W. Schwitz

Division 522

R. Dove
H. Marshak

Division 532

R. Caswell
A. Wasson

Division 533

R. Plaeious

Division 541

R. Kavanagh
J. Kelly
T. Madey

Division 544

S. Greer
D. Tsai

Division 553

H. Rook

STAFF ROSTER

Division 562

F. Biancanello
J. Early

Division 563

R. Bowen
C. Han

Division 564

R. Reno
R. Shull

Division 741

P. Brown

Argonne National Laboratory

R. Armani
T. Brun
R. Dunlap
H. Flotow
O. Hinks
S. Susman
J. Viccaro

Battelle, N. W.

W. Nicholson

Brookhaven National Laboratory

P. Levy
D. Richter

Federal Bureau of Investigation

R. Asbery
D. B. Davies
J. Haverkost
J. W. Kilty
E. Mitchell
C. Peters
J. P. Riley

Food and Drug Administration

M. Allegrini
W. Cunningham
D. Daly
W. Stroube, Jr.
J. Tanner

Harry Diamond Laboratory

C. Heimbach

National Gallery of Art

B. Miller
J. Olin
C. Parkhurst
K. Siverfelt

National Institutes of Health

D. Davies
R. Frank
J. Weinstein

Naval Air Defense Command

W. Williams

Naval Research Laboratory

C. Bond
P. D'Antonio
A. Ehrlich
M. Fatemi
J. Karle
N. Koon
F. Kuchas
K. Murray
V. Rath
L. Pecoia

Picatinny Arsenal

C. S. Choi
H. J. Prask
S. Trevino

STAFF ROSTER

Carnegie Institute of Washington

B. K. Kothari

Smithsonian Institution

M. Blackman

T. Chase

J. Mishara

S. O'Dell

L. Zacherman

U. S. Geological Survey

P. Baedeker

J. Morgan

American University

J. Ferrick

R. A. Segnan

Colorado State University

C. E. Patton

Howard University

G. A. Ferguson

Iowa State University

R. Shelton

Israel Institute of Technology

Y. Segal

Massachusetts Institute of Technology

B. Averbach

Reed College

W. Parker

Technical University of Munich

H. Metzger

H. Wipf

University of Antwerp

K. Michel

University of Arizona

R. Salemm

P. Weber

University of Alabama

J. Segrest

University of California

(Lawrence Livermore Laboratories)

J. Browne

D. Hankins

University of Chicago

E. Anders

R. Wolf

University of Houston

S. Moss

University of Illinois

H. Zabel

University of Maine

H. Patterson

University of Maryland

D. Anderson

N. ARas

D. Ballantine

G. Barley

D. Finnegan

STAFF ROSTER

I. Gokman
G. Gordon
W. Johnson
J. Lynn
J. Parrington
J. Phelan
S. Reingrover
W. Sonnefeld
M. Thompson
W. Walters
J. Weber
J. Winer
M. Yiu
W. Zoller

University of Missouri (Rolla)

W. James

State University of New York

H. Herman

University of Paris

B. Le Neindre

University of Pittsburgh

R. Buttera
S. Sankar
W. Wallace

University of Rhode Island

S. Pickart

Virginia Poly Technic Institute

R. Peterson
G. Gibbs

University of Wisconsin

J. Hinkley
J. Perepesco
H. Yu

Allied Chemical Corporation

G. Leibowitz
A. Maeland

B-K Dynamics

N. Chesser

Fedders Air Conditioning Company

W. Simpkins

General Electric Company

F. Luborsky
J. Walter

Lockheed Missile & Space, Inc.

D. Webster

Metronic, Inc.

P. Skarstad

Monsanto Research Corporation

W. Brotherton

Man Tech Corporation

D. Bracher

Sandia Corporation

J. Harris

Wilson Greatbach, Ltd.

R. Steinbring

Nuclear Energy Center, Mol, Belgium

A. Fabry

G. PUBLICATIONS

COLLABORATIVE PROGRAMS

- BARKIGIA, K. M., RAJKOVIC -BLAZER, L. M., POPE, M. T., PRINCE, E., and QUICKSALL, C. O., "Molybdoarsinate Heteropoly Complexes. The Structure of the Hydrogentetramolybdodimethylarsinate (2-) Anion by X-ray and Neutron Diffraction," *Inorganic Chemistry*, (in press).
- BRACHER, D. A., GARRETT, D. A., and HELLER, C., "Theory and Design of Instrumentation for Bridge Investigations," *Proceedings of the Mechanical Failures Prevention Group* (1980).
- CASELLA, R. C., "Neutron Scattering from Coherent Admixtures of Phonons with Libronic Excitations of Diatomic Impurities," *Phys. Rev.* B20, 5318 (1979).
- CHOI, C. S., PRASK, H. J., and TREVINO, S. F., "Non-destructive Investigation of Texture by Neutron Diffraction," *J. Appl. Cryst.* 12, 327-331 (1979).
- CHOI, C. S., PRASK, H. J., and PRINCE, E., "Phase Transitions in Ammonium Nitrate," *J. Appl. Cryst.* (in press).
- CHOI, C. S., and MARINKAS, P. L., "Refinement of Dipara-anthracene," *Acta. Cryst.* (in press).
- CULLEN, J. ALPERIN, H., MELAMUD, M. HATHAWAY, K., and RHYNE, J. J., "Magnetoelasticity and Moment Rotation in Amorphous Rare Earth-Iron Alloys," *Int'l J. of Magnetism and Magnetic Materials* 15, 593 (1980).
- D'ANTONIO, P. and SANTORO, A., "Powder Neutron Diffraction Study of Chemically Prepared β -PbO₂," *Acta. Cryst.* (in press).
- DOMBECK, T. W., LYNN, J. W., WERNER, S. A., BURN, T., CARPENTER, J., KROHN, V. and RINGO, R., "Production of Ultra-Cold Neutrons Using Doppler-Shifted Bragg Scattering and Intense Pulsed Neutron Spallation Source," *Nuc. Instr. and Meth.* 165, 139 (1979).

- FISH, G. E., RHYNE, J. J., BURN, T., VICARRO, P. J., NIARCHOS, D., DUNLAP, B. D., SHENOY, G. K., SANKAR, S. G., and WALLACE, W. E., "Neutron Scattering Studies of Hydrides of the Laves-Phase Rare Earth Compounds RFe_2 ," *Rare Earths in Modern Science and Technology II*, Plenum Publishers, p. 569 (1980).
- FORESTER, D. W., KOON, N. C., SCHELLENG, J. H., RHYNE, J. J., "Amorphous YFe_2 - A Concentrated Spin Glass," *J. Appl. Phys.* (to be published).
- FORESTER, D. W., KOON, N. C., SCHELLENG, J. H., and RHYNE, J. J., "Spin Glass and Magnetic Blocking Transitions in Amorphous YFe_2 - A Concentrated Spin Glass," *J. Appl. Phys.* 50, 7336-41 (1979).
- GLINKA, C. J., ROWE, J. M., LIBOWITZ, G. G., and MAELAND, A., "Neutron Crystal-Field Spectroscopy of $CeD_{2.12}$," *Journal of Physics: C* 12, 4229 (1970).
- GLINKA, C. J., PRASK, H. J., and CHOI, C. S., "Neutron Diffraction and Small-Angle Scattering as Nondestructive Probes of the Micro-structure of Materials," *Proceedings of the Conference on Mechanics of Nondestructive Testing*, (ed. by W. W. Stinchcomb, Plenum Press pp. 143-164 (1980).
- HARDMAN, K., JAMES, W. J., and YELON, W. B., "Preferential Ordering of Mn and Fe Atoms in $Y_6(Fe_{1-x}Mn_x)_{23}$," *Journal of Physics and Chemical Solids* (in press).
- HARDMAN, K., RHYNE, J. J., SMITH, K., and WALLACE, W. E., "Structural Investigation of $Th_6Mn_{23}D_{16}$ by Neutron Diffraction," *Journal of the Less Common Metals* (in press).
- KELLEY, R. D., CAVANAGH, R. R., RUSH, J. J., and MADEY, T. E., "Neutron Inelastic Scattering Study of C_2H_4 Adsorbed on Raney Nickel," *Surface Science* (in press).
- KELLEY, R. D., RUSH, J. J., and MADEY, T. E., "Vibrational Spectroscopy of Adsorbed Species on Nickel by Neutron Inelastic Scattering," *Chemical Physics Letters* 66, 159-164 (1979).
- KOON, N. C., and RHYNE, J. J., "Exchange and Crystal Field Excitations in Rare Earth Iron and Rare Earth Cobalt Laves-Phase Compounds," *Crystalline Electric Fields and Structural Effects in f-Electron Systems*, edited by J. E. Crow, R. P. Guertin, and T. W. Mihalisin, Plenum Publishing, p. 125 (1980).
- LYNN, J. W., "Crystal Field Effects in Magnetic Superconductors," *Crystalline Electric Fields and Structural Effects in f-Electron Systems*, edited by J. E. Crow, R. P. Guertin, and T. W. Mihalisin, Plenum Publishing, p. 547 (1980).

PUBLICATIONS

- LYNN, J. W., MONCTON, D. E., PASSELL, L. and THOMLINSON, W., "Magnetic Correlations and Crystal Field Levels in the Superconductor $(\text{Ce}_{.73}\text{Ho}_{.27})\text{Ru}_2$," *Phys. Rev.* B21, 70 (1980).
- LYNN, J. W. and GLINKA, C. J., "Magnetic Properties of the Superconducting Alloy System $(\text{Ce}_{1-c}\text{Ho}_c)\text{Ru}_2$ - A Neutron Scattering Study," *J. Magnetism and Magnetic Materials* 14, 179 (1979).
- LYNN, J. W. and SHELTON, R. N., "Neutron Scattering Studies of Magnetic Superconductors," *J. Magnetism and Magnetic Materials* 18, 1577 (1980).
- MAGERL, A., ROWE, J. M. and RICHTER, D., "On the Observation of Low Energy Excitations in NbD - A Simple Lattice Dynamical Model," *Phys. Rev. B* 22, 1417 (1980).
- MICHEL, K. H., and ROWE, J. M., "On the Existence of an Orientational Glass State in $(\text{KCN})_x(\text{KBr})_{1-x}$ Mixed Crystals," *Phys. Rev. B* (in press).
- NICHOLSON, W. W., and PRINCE, E., "Arobust/Resistant Technique for Crystal Structure Refinement," *Acta Cryst. A* (submitted).
- PRASK, H. J. CHOI, C. S., and TREVINO, S. F., "Nondestructive Testing of Armament-System Components by Means of Neutron Diffraction," *Proc. of the Army Science Conference* (in press).
- PRASK, H. J., and CHOI, C. S., "Texture, Nondestructive Characterization," *Ency. Matls. Sci. and Eng.* (submitted).
- PRINCE, E., "Comparison of Profile and Integrated Intensity Methods in Powder Refinement," *J. Appl. Cryst.* (submitted).
- RHYNE, J. J. "Amorphous Magnetic Materials - Chapter 16," *Handbook on the Physics and Chemistry of Rare Earths*, ed. by K. A. Gschneider and L. Eyring, North Holland Publishing, (1979).
- RHYNE, J. J. and KOON N. C., "RPA Theory of Magnetic Excitations in Rare Earth-Transition Metal Compounds: Application of ErCo_2 and ErFe_2 ," *Int's. J. of Magnetism and Magnetic Materials* 15, 349 (1980).
- RHYNE, J. J., KOON, N. C., and DAS, B. N., "Ground State Excitations in HoCo_2 ," *Intl. J. of Magnetism and Magnetic Materials* 14, 273 (1979).
- RHYNE, J. J., KOON, N. C. and ALPERIN, H. A., "Magnetic Excitations in TbFe_2 ," *Rare Earths in Modern Science and Technology II*, Plenum Publishers, p. 313 (1980).

PUBLICATIONS

- RHYNE, J. J., "Magnetic Inelastic Neutron Scattering Studies of Rare Earth Metals and Laves-Phase Compounds," *Proc. of the Science and Technology of Rare Earth Materials* (in press).
- RHYNE, J. J., "Magnetic Materials," *Article for the Encyclopedia of Physics*, ed. by R. G. Lerner and G. L. Trigg, Addison-Wesley Publishing, (in press).
- ROWE, J. M. and MAGERL, A., "Neutron Diffuse Scattering Intensities in Niobium," *Phys. Rev. B* 21, 1706-7 (1980).
- ROWE, J. M., RUSH, J. J., SHAPIRO, S. M. HINKS, D. G., and SUSMAN, S., "Neutron Scattering Studies of (CN)⁻ Defects in KBr," *Phys. Rev. B* 21, 4863-4868 (1980).
- ROWE, J. M., RUSH, J. J., HINKS, D. G. and SUSMAN, S., "Neutron Scattering Study of the Dynamics of KCN_{0.5}KBr_{0.5}," *Phys. Rev. Lett.* 43, 1158-61 (1979).
- RUSH, J. J., ROWE, J. M., GLINKA, C. J., VAGELATOS, N., and FLOTOW, H. E., "Coherent Neutron Scattering Study of the Vibrations of Interstitial Deuterium in α -VD_{0.7}," *Phys. Rev. B* 21, 5613-5616 (1980).
- RUSH, J. J., ROWE, J. M., and MAELAND, A. J., "Neutron Scattering Study of Hydrogen Vibrations in Polycrystal and Glassy TiCuH," *Journal of Physics F* (in press).
- SANTORO, A. and WLODAWER, A., "Absorption Correction for Weissenberg Diffractometers," *Acta Cryst.* A36, 442-450 (1980).
- SANTORO, A., MIGHELL, A. D., and RODGERS, J. R., "Determination of the Relationship Between Derivative Lattices," *Acta Cryst.* (in press).
- SANTORO, A., MIGHELL, A., and RODGERS, J., "Lattice Relationships: The Determination of Matrices that Will Relate Any Given Pair of Lattices," *Acta Cryst.* (in press).
- SANTORO, A., ROTH, R. S., and MINOR, D., "Neutron Powder Diffraction Study of the Structure of CeTaO₄, CeNbO₄, and NdTaO₄," *Journal of Solid State Chemistry* (in press).
- SANTORO, A., MAREGIE, M., ROTH, R. S., and MINOR, D., "Neutron Powder Diffraction Study of the Structure of CeTaO₄, CeNbO₄, and NdTaO₄," *Journal of Solid State Chemistry* (in press).
- SANTORO, A., "Use of Derivative Lattices in the Indexing of Powder Patterns," *Acta Cryst.* (submitted).

PUBLICATIONS

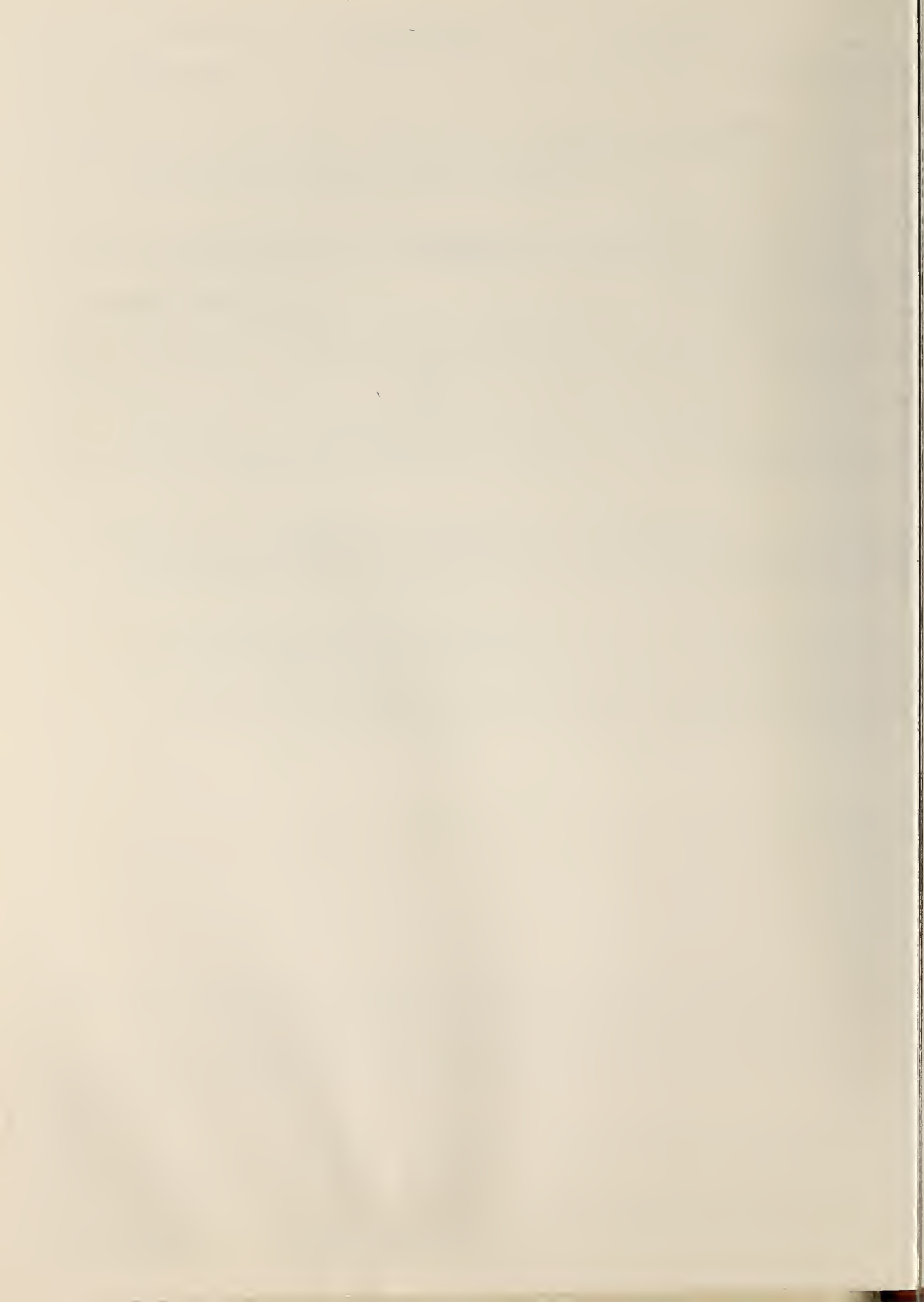
INDEPENDENT PROGRAMS

- CARPENTER, B. S., and PILIONE, L. J., "Lithium and Lithium-6 Analysis in Solutions by the Nuclear Track Technique," *Anal. Chem.*, (in press).
- CARPENTER, B. S., and JONES, F. E., eds., "Measurements and Standards for Nuclear Materials Safeguards," NBSIR 80-2033, May 1980.
- CANADA, T. R., and CARPENTER, B. S., eds., "Measurement Technology for Safeguards and Materials Control," *NBS Spec. Publ.* 582 (1980).
- CARPENTER, B. S., PILIONE, L. J., SCHRODER, I. G., ROE, J. W., and SANATINI, S., "Evaluation of Reactor Track-Etch Power Monitor," *ANS Transactions*, Vol. 33, 21 (1979).
- GREENBERG, R. R., "Simultaneous Determination of Mercury and Cadmium in Biological Materials by Radiochemical Neutron Activation Analysis," *Anal. Chem.*, 52, 676 (1980).
- HARRISON, S. H., MAIENTHAL, E. J., GILLS, T. E., and ZEISLER, R., "Protocol for the Collection, Storage, and Analysis of Human Organs the Pilot Bank Project of the National Environmental Specimen Bank," in *Trace Substances in Environmental Health*, XIII, D. P. Hemphill, ed., U. of Missouri, Columbia, June 1980 (in press).
- LINDSTROM, R. M., and FLEMING, R. F., "Accuracy in Activation Analysis: Count Rate Effects," to be published in Proc. of 4th International Conference on Nuclear Methods in Environmental and Energy Research (Univ. of Missouri, Columbia) 1980.
- LINDSTROM, R. M., "Measuring Trace Elements in Semiconductors: Methods and Pitfalls," *Solar Cells*, 1 (2), 117 (1980).
- LUX, F., ZEISLER, R., and REHER, J., "Aktivierungsanalytische Untersuchungen über die Probenmengenabhängigkeit der Streuung der Spurenelementgehaltswerte von Bleiweiss sowie über den cisalpinen Typ von Bleiweiss aus einem Rugens-Gemälde," *Radiochem. Radioanal. Letters*, 42, 341 (1980).
- MITCHELL, J. W., RILEY, JR., J. E., and CARPENTER, B. S., "Major Elemental Boron Determination by the Nuclear Track Technique," *ANS Transactions*, Vol. 34, 143 (1980).
- SCHWARTZ, R. B., EISENHauer, C. M., GILLIAM, D. M., SPIEGEL, V. and WASSON, O. A., *Trans. Am. Nuc. Soc.* 34, p. 621 (1980).

PUBLICATIONS

- TREVINO, S. F., "An Observation of One-Dimensional Reorientation and Tunnel Splitting of the Ground and First Excited State in a Low Barrier System: Solid Nitromethane," *J. Chem. Phys.* (Letter to the Editor) 71, 1973-4 (1979).
- TREVINO, S. F., PRINCE, E., and HUBBARD, C. R., "Refinement of the Structure of Solid Nitromethane," *J. Chem. Phys.* (in press).
- TREVINO, S. F. and RYMES, W. H., "A Study of Methyl Reorientation in Solid Nitromethane by Neutron Scattering," *J. Chem. Phys.* (in press).
- WLODAWER, A., SEGREST, J. P., CHANG, B. H., CHIOUETTE, R., and WEINSTEIN, J. N., "High Denisty Lipoprotein Recombinants: Evidence for a Bicycle Tire Micelle Structure Obtained by Neutron Scattering and Electron Microscopy," *FEBS LETTERS* 104, 231-235 (1979).
- ABRAHAMSSON, S., LINDQVIST, O., SJÖLIN, L., and WLODAWER, A., "Preliminary Investigation of a New X-ray Film," *J. Appl. Cryst.* (submitted).
- WLODAWER, A., "Studies of Ribonuclease-A by X-ray and Neutron Diffraction," *Acta Cryst. B* (in press).

U.S. DEPT. OF COMM. BIBLIOGRAPHIC DATA SHEET (See instructions)		1. PUBLICATION OR REPORT NO. NBS TN 1142	2. Performing Organ. Report No.	3. Publication Date May 1981
4. TITLE AND SUBTITLE NBS Reactor: Summary of Activities July 1979 to June 1980				
5. AUTHOR(S) Frederick J. Shorten, Editor				
6. PERFORMING ORGANIZATION (If joint or other than NBS, see instructions) NATIONAL BUREAU OF STANDARDS DEPARTMENT OF COMMERCE WASHINGTON, D.C. 20234			7. Contract/Grant No.	
			8. Type of Report & Period Covered July 1979 to June 1980	
9. SPONSORING ORGANIZATION NAME AND COMPLETE ADDRESS (Street, City, State, ZIP) Same as item 6.				
10. SUPPLEMENTARY NOTES <input type="checkbox"/> Document describes a computer program; SF-185, FIPS Software Summary, is attached.				
11. ABSTRACT (A 200-word or less factual summary of most significant information. If document includes a significant bibliography or literature survey, mention it here) This report summarizes all those programs which depend on the NBS reactor. It covers the period from July 1979 through June 1980. The programs range from the use of neutron beams to study the structure and dynamics of materials through nuclear physics and neutron standards to sample irradiations for activation analysis, isotope production, radiation effects studies, neutron radiography, and nondestructive evaluation.				
12. KEY WORDS (Six to twelve entries; alphabetical order; capitalize only proper names; and separate key words by semicolons) Activation analysis; crystal structure; diffraction; isotopes; molecular dynamics; neutron; neutron radiography; nondestructive evaluation; nuclear reactor; radiation.				
13. AVAILABILITY <input checked="" type="checkbox"/> Unlimited <input type="checkbox"/> For Official Distribution. Do Not Release to NTIS <input checked="" type="checkbox"/> Order From Superintendent of Documents, U.S. Government Printing Office, Washington, D.C. 20402. <input type="checkbox"/> Order From National Technical Information Service (NTIS), Springfield, VA. 22161			14. NO. OF PRINTED PAGES 211	
			15. Price	



NBS TECHNICAL PUBLICATIONS

PERIODICALS

JOURNAL OF RESEARCH—The Journal of Research of the National Bureau of Standards reports NBS research and development in those disciplines of the physical and engineering sciences in which the Bureau is active. These include physics, chemistry, engineering, mathematics, and computer sciences. Papers cover a broad range of subjects, with major emphasis on measurement methodology and the basic technology underlying standardization. Also included from time to time are survey articles on topics closely related to the Bureau's technical and scientific programs. As a special service to subscribers each issue contains complete citations to all recent Bureau publications in both NBS and non-NBS media. Issued six times a year. Annual subscription: domestic \$13; foreign \$16.25. Single copy, \$3 domestic; \$3.75 foreign.

NOTE: The Journal was formerly published in two sections: Section A "Physics and Chemistry" and Section B "Mathematical Sciences."

DIMENSIONS/NBS—This monthly magazine is published to inform scientists, engineers, business and industry leaders, teachers, students, and consumers of the latest advances in science and technology, with primary emphasis on work at NBS. The magazine highlights and reviews such issues as energy research, fire protection, building technology, metric conversion, pollution abatement, health and safety, and consumer product performance. In addition, it reports the results of Bureau programs in measurement standards and techniques, properties of matter and materials, engineering standards and services, instrumentation, and automatic data processing. Annual subscription: domestic \$11; foreign \$13.75.

NONPERIODICALS

Monographs—Major contributions to the technical literature on various subjects related to the Bureau's scientific and technical activities.

Handbooks—Recommended codes of engineering and industrial practice (including safety codes) developed in cooperation with interested industries, professional organizations, and regulatory bodies.

Special Publications—Include proceedings of conferences sponsored by NBS, NBS annual reports, and other special publications appropriate to this grouping such as wall charts, pocket cards, and bibliographies.

Applied Mathematics Series—Mathematical tables, manuals, and studies of special interest to physicists, engineers, chemists, biologists, mathematicians, computer programmers, and others engaged in scientific and technical work.

National Standard Reference Data Series—Provides quantitative data on the physical and chemical properties of materials, compiled from the world's literature and critically evaluated. Developed under a worldwide program coordinated by NBS under the authority of the National Standard Data Act (Public Law 90-396).

NOTE: The principal publication outlet for the foregoing data is the Journal of Physical and Chemical Reference Data (JPCRD) published quarterly for NBS by the American Chemical Society (ACS) and the American Institute of Physics (AIP). Subscriptions, reprints, and supplements available from ACS, 1155 Sixteenth St., NW, Washington, DC 20056.

Building Science Series—Disseminates technical information developed at the Bureau on building materials, components, systems, and whole structures. The series presents research results, test methods, and performance criteria related to the structural and environmental functions and the durability and safety characteristics of building elements and systems.

Technical Notes—Studies or reports which are complete in themselves but restrictive in their treatment of a subject. Analogous to monographs but not so comprehensive in scope or definitive in treatment of the subject area. Often serve as a vehicle for final reports of work performed at NBS under the sponsorship of other government agencies.

Voluntary Product Standards—Developed under procedures published by the Department of Commerce in Part 10, Title 15, of the Code of Federal Regulations. The standards establish nationally recognized requirements for products, and provide all concerned interests with a basis for common understanding of the characteristics of the products. NBS administers this program as a supplement to the activities of the private sector standardizing organizations.

Consumer Information Series—Practical information, based on NBS research and experience, covering areas of interest to the consumer. Easily understandable language and illustrations provide useful background knowledge for shopping in today's technological marketplace.

Order the above NBS publications from: Superintendent of Documents, Government Printing Office, Washington, DC 20402.

Order the following NBS publications—FIPS and NBSIR's—from the National Technical Information Services, Springfield, VA 22161.

Federal Information Processing Standards Publications (FIPS PUB)—Publications in this series collectively constitute the Federal Information Processing Standards Register. The Register serves as the official source of information in the Federal Government regarding standards issued by NBS pursuant to the Federal Property and Administrative Services Act of 1949 as amended, Public Law 89-306 (79 Stat. 1127), and as implemented by Executive Order 11717 (38 FR 12315, dated May 11, 1973) and Part 6 of Title 15 CFR (Code of Federal Regulations).

NBS Interagency Reports (NBSIR)—A special series of interim or final reports on work performed by NBS for outside sponsors (both government and non-government). In general, initial distribution is handled by the sponsor; public distribution is by the National Technical Information Services, Springfield, VA 22161, in paper copy or microfiche form.

U.S. DEPARTMENT OF COMMERCE
National Bureau of Standards
Washington, D.C. 20234

OFFICIAL BUSINESS

Penalty for Private Use, \$300

POSTAGE AND FEES PAID
U.S. DEPARTMENT OF COMMERCE
COM-215



SPECIAL FOURTH-CLASS RATE
BOOK